

VU Research Portal

The Pion Charge Form Factor via Pion Electroproduction on the Proton

Volmer, J.

2000

document version

Publisher's PDF, also known as Version of record

[Link to publication in VU Research Portal](#)

citation for published version (APA)

Volmer, J. (2000). *The Pion Charge Form Factor via Pion Electroproduction on the Proton*. [PhD-Thesis - Research and graduation internal, Vrije Universiteit Amsterdam]. Vrije Universiteit.

General rights

Copyright and moral rights for the publications made accessible in the public portal are retained by the authors and/or other copyright owners and it is a condition of accessing publications that users recognise and abide by the legal requirements associated with these rights.

- Users may download and print one copy of any publication from the public portal for the purpose of private study or research.
- You may not further distribute the material or use it for any profit-making activity or commercial gain
- You may freely distribute the URL identifying the publication in the public portal ?

Take down policy

If you believe that this document breaches copyright please contact us providing details, and we will remove access to the work immediately and investigate your claim.

E-mail address:

vuresearchportal.ub@vu.nl

**The Pion Charge Form Factor
via Pion Electroproduction
on the Proton**

Jochen Volmer

The work described in this thesis is part of the research programme of the “Stichting voor Fundamenteel Onderzoek der Materie (FOM)”, which is financially supported by the “Nederlandse Organisatie voor Wetenschappelijk Onderzoek (NWO)”

VRIJE UNIVERSITEIT

**The Pion Charge Form Factor
via Pion Electroproduction
on the Proton**

ACADEMISCH PROEFSCHRIFT

ter verkrijging van de graad van doctor aan
de Vrije Universiteit te Amsterdam,
op gezag van de rector magnificus
prof.dr. T. Sminia,
in het openbaar te verdedigen
ten overstaan van de promotiecommissie
van de faculteit der Exacte Wetenschappen/
Natuurkunde en Sterrenkunde
op dinsdag 3 oktober om 13.45 uur
in het hoofdgebouw van de universiteit,
De Boelelaan 1105

door

Jochen Volmer

geboren te Coesfeld, Duitsland

Promotor: prof.dr. G. van Middelkoop

Copromotoren: dr. H.P. Blok
dr. D.J. Mack

Contents

1	Introduction	1
2	Theoretical background and existing data	7
2.1	Introduction	7
2.2	Pion electroproduction	8
2.2.1	Kinematics	8
2.2.2	Cross sections	10
2.2.3	Models for pion electroproduction	11
2.2.4	Isoscalar contributions	14
2.2.5	Extraction of F_π	14
2.3	Existing data	15
2.4	Calculations for F_π	18
2.4.1	Asymptotic behaviour of F_π	19
2.4.2	F_π at low Q^2 in perturbative QCD	21
2.4.3	Models for soft contributions	25
2.4.4	Concluding remarks	27
3	Experimental apparatus	29
3.1	Accelerator	29
3.2	Target and scattering chamber	33
3.2.1	Cryogenic target	33
3.2.2	Optics target	34
3.3	Spectrometers	36
3.3.1	High Momentum Spectrometer	36
3.3.2	Short Orbit Spectrometer	38
3.4	Detector packages	39
3.4.1	Drift chambers	40
3.4.2	Hodoscopes	41

3.4.3	Gas Čerenkov counter	41
3.4.4	Lead-glass calorimeter	41
3.5	Trigger system and data acquisition	42
4	Spectrometer calibrations	45
4.1	Introduction to spectrometer optics	45
4.1.1	Definitions	45
4.1.2	Reconstruction of target quantities	48
4.2	The HMS-100 tune	49
4.3	Magnet setting and cycling	50
4.3.1	HMS quadrupole magnet setting procedure	50
4.3.2	HMS dipole magnet setting procedure	51
4.3.3	SOS magnet setting procedure	52
4.4	Results from matrix element fitting	52
4.4.1	Results for the HMS	52
4.4.2	Results for the SOS	55
4.5	Determination of experimental offsets	58
4.6	Saturation effects in the SOS	61
5	Data analysis	63
5.1	Choice of kinematics	63
5.2	Upgrades to the replay engine	65
5.3	Identification of good events	66
5.3.1	Particle identification	66
5.3.2	Subtraction of backgrounds	68
5.4	Efficiencies, dead times and other correction factors	69
5.4.1	Tracking efficiencies	69
5.4.2	Computer and electronics dead times	71
5.4.3	Coincidence blocking and retiming correction	72
5.4.4	Pion absorption	73
5.4.5	Target density correction	74
5.4.6	Charge measurement	74
5.5	SIMC	75
5.5.1	Overview of SIMC	75
5.5.2	$^1\text{H}(e, e'p)$ in SIMC	78
5.5.3	Detector acceptances in SIMC	79
5.5.4	The model cross section for pion electroproduction	80
5.6	L/T separation	83

5.7	Estimate of uncertainties	84
5.8	Analysis cuts	86
6	Results and discussion	89
6.1	Experimental cross sections	89
6.1.1	Discussion of the cross sections	89
6.1.2	Comparison with the VGL model	91
6.2	Extraction of the pion form factor	94
6.2.1	Pure VGL model	94
6.2.2	VGL model with constant background term	95
6.2.3	t -dependent F_π	96
6.2.4	$g_{\pi NN}$ -like t -dependence	96
6.3	Best values for F_π	97
6.4	Reanalysis of existing data	99
6.4.1	DESY data	99
6.4.2	CEA/Cornell data	100
6.5	Discussion	102
7	Summary	107
A	Tables of cross sections	111
B	Tables for F_π data	115
	References	119
	Samenvatting	125
	Zusammenfassung	129
	Nawoord	133

Chapter 1

Introduction

The fundamental nature of matter in terms of elementary particles and their interactions is the central topic in subatomic physics. From the nuclear physics perspective, the atom consists of a cloud of electrons surrounding a positively charged nucleus, which contains protons and neutrons. The protons and neutrons, collectively called nucleons, are held together by the strong nuclear force via the exchange of, *e.g.*, pions. Hadrons, *i.e.*, strongly interacting particles like nucleons or pions, are not elementary particles themselves but instead exhibit a substructure based on more fundamental particles, the so-called partons. The electrons, on the other hand, are believed to be fundamental in nature.

The most successful model currently available for the fundamental building blocks of matter is the so-called Standard Model. According to the Standard Model, there are three families of elementary particles, namely quarks, leptons and gauge bosons. Examples of leptons are electrons and neutrinos. The quarks are identified with the partons that are bound together into hadrons. The forces between them are mediated via the exchange of gauge bosons, such as photons for the electromagnetic interaction, and gluons for the strong interaction.

The field theory for electromagnetic interactions is Quantum Electrodynamics (QED). This theory has been developed into an instrument that allows high precision calculations for electromagnetic processes. Analogously, the field theory for the strong interaction between quarks is Quantum Chromodynamics* (QCD), with gluons as field quanta carrying the colour charge. In contrast to the field quanta of QED, the photons, gluons can interact with each other. This and the large value of

*The term is derived from $\chi\rho\tilde{\omega}\mu\alpha$, greek for colour.

the strong coupling constant, at low energies $\alpha_s \simeq 1^\dagger$, makes exact calculations at low momenta impossible. For processes with high values of the momentum transfer, α_s decreases, so that for large enough momentum transfers the strong interaction becomes in principle calculable exactly by means of perturbative calculations (perturbative QCD, or pQCD).

The existence of partons inside the hadrons is well established by now through the scattering of energetic electrons off protons. At high electron energies the inelastic electron-proton scattering is viewed as elastic scattering of the electron from a “free” quark inside the proton. However, the internal structure of hadrons cannot be calculated from first principles. It can be studied by investigating collective observables of the bound systems. Electromagnetic form factors of hadrons reflect the distribution of charge and current in the hadron. Therefore the study of hadronic form factors can give insight into the internal structure of hadrons. Since no exact calculations can be done in the non-perturbative regime of QCD, the challenge of describing the strong interaction at small values of momentum transfer is one of finding effective models for the non-perturbative part. Input from experimental data is needed to constrain those models.

The pion as a pQCD laboratory has a number of advantages over other hadrons. Being a spin-zero particle, it only has one electromagnetic form factor, F_π , which depends solely on the square of the four-momentum transfer[‡], Q^2 . As a meson, the valence structure of the pion is a bound state of two quarks, whereas nucleons consist of three valence quarks. Therefore a minimum of only one gluon has to be exchanged between the quarks in order to keep the pion intact when an electron scatters off one of its quarks, whereas at least two gluons have to be exchanged in the case of the proton. Since the transferred momentum has to be divided among the gluons, the regime of applicability of perturbative QCD is expected to start at much lower values of Q^2 for F_π than for the nucleon form factors. Furthermore, the pion is easily produced experimentally. And, last but not least, the behaviour of F_π in the asymptotic limit $Q^2 \rightarrow \infty$ is known. It is normalized by f_π , the pion decay constant known from the weak decay of the pion ($\pi \rightarrow \mu + \nu_\mu$). In contrast, no normalization of the nucleon form factors in the asymptotic limit is known.

In this thesis the electromagnetic form factor of the charged pion is studied for values of Q^2 between 0.6 and 1.6 (GeV/c)², where non-perturbative contributions largely outweigh the perturbative ones. Theoretical models for F_π need to satisfy two boundary conditions: the very low Q^2 behaviour must conform to the well

[†]For comparison, the electromagnetic coupling constant is $\alpha \simeq 1/137$.

[‡]The square of the transferred four-momentum q^2 is always negative in electron scattering. Hence, commonly, $Q^2 \equiv -q^2$ is defined.

known pion charge radius, and the very high Q^2 behaviour must approach the perturbative prediction. The differences between the models are therefore largest in the region of a few $(\text{GeV}/c)^2$. For this reason the measurements presented here are a sensitive test for the various theoretical models that make predictions at intermediate values of Q^2 .

Pions are easily produced off nucleons in inelastic scattering processes, but they are not stable. Hence, no free pion targets are available for elastic electron-pion scattering experiments. Instead, highly energetic pions have been produced and scattered off atomic electrons in experiments at CERN and other laboratories. In this way F_π has been measured to a very high accuracy for low values of Q^2 . These measurements have been used to determine the pion charge radius, but they were limited to values of Q^2 of up to $0.28 (\text{GeV}/c)^2$. Much larger values of Q^2 can be reached by scattering electrons off pions. For lack of a free pion target one has to resort to pion electroproduction on a nucleon. This process can be viewed as scattering of the electron off a virtual pion in the nucleon. The price paid for the higher values of Q^2 is that *a priori* it is not clear whether the process is really quasi-free scattering from a pion or whether it is a pion production process.

The pion exchange process that dominates the longitudinal part of the forward pion electroproduction cross section includes F_π . In this context, “forward” means that the pion is emitted along the direction of the virtual photon. Hence, the part of the cross section that is due to longitudinally polarized photons (σ_L) needs to be separated from the part that is due to transversely polarized photons (σ_T). This is done in a so-called Rosenbluth separation, for which measurements at different electron energies, but for constant values of Q^2 and invariant mass W of the photon-nucleon system are necessary. In order to minimize contributions to the cross sections from other processes, such as nuclear resonances, the measurements are best done at values of W above the resonance region, *i.e.*, above about 2 GeV. The extraction of F_π from the separated pion electroproduction data is done using a theoretical model (Regge or Born term models) for the electroproduction cross section, in which F_π is a parameter that is used to adjust the model prediction for the longitudinal cross section σ_L to the experimental data. This method for extracting F_π from experimental data means that the result depends on the theoretical model used in the analysis.

Older F_π data exist from one experiment at DESY (Ref. [Bra77]) and from four experiments done at CEA (Cambridge, Massachusetts) and Cornell (Ref. [Beb78]). In the former experiment pion electroproduction data for a value of Q^2 of $0.7 (\text{GeV}/c)^2$ were taken and the longitudinal and transverse cross sections were determined in a Rosenbluth separation. A Born term model (Ref. [Gut72])

was used to extract a value for F_π from the data on σ_L . The experiments from CEA and Cornell were done over the course of several years and cover a range in Q^2 of 0.28-9.77 (GeV/c)². Each of the experiments produced either high or low electron energy data. A Rosenbluth separation was attempted for some data points for which both high and low electron energy data had been taken, but the result suffered from large uncertainties. Therefore, σ_L was calculated for each measurement by subtracting a simple model for σ_T from the measured total cross section. A Born term model (Ref. [Ber70]) was used to extract values for F_π from these data. However, the results are still inconsistent, and due to their large systematic and statistical uncertainties have in fact no power to constrain theoretical models for F_π .

Clearly, reliable data for F_π are needed for values of Q^2 above 0.7 (GeV/c)². The data presented here fill this void. The measurements have been done in the fall of 1997 at the Thomas Jefferson National Accelerator Facility (TJNAF, or Jefferson Lab), which has been operating since 1995 in Newport News, Virginia. The accelerator (CEBAF) delivered electrons with energies of up to 4 GeV at a high intensity and with a high duty factor. Upgrades to the accelerator are bringing the electron energy to 6 GeV, and in a later stage, to 12 GeV. The present data represent the first phase of measurements of forward pion electroproduction at Jefferson Lab. They provide consistent sets of data for a Rosenbluth separation for values of Q^2 up to 1.6 (GeV/c)². A second phase with measurements for values of Q^2 of up to 3.2 (GeV/c)² has been approved and is planned to be done in 2001-2002.

This thesis consists of seven chapters.

The second chapter lays the theoretical ground for the extraction of separated cross sections from the experimental data and the theoretical model that is used in the analysis to extract values for F_π . The existing data from DESY and CEA/Cornell are discussed in detail. The chapter ends with the discussion of the calculations of F_π in perturbative QCD and in various non-perturbative models.

The experimental apparatus at Jefferson Lab used in the experiment is presented in chapter three.

A corner stone of the present analysis is the understanding of the magneto-optical properties of the two magnetic spectrometers of Jefferson Lab's experimental Hall C, where the experiment took place. The changes to the magnetic setup of one of the spectrometers, the investigation of the focussing properties, calibration measurements, and analysis of the calibration data are discussed in chapter four.

Chapter five contains the description of the analysis of the experimental data. In the first part of this chapter the particle identification, calculation of experimental efficiencies and dead times are described. The second part discusses the Monte

Carlo simulation program and its center piece, the model for the cross section for forward pion electroproduction for values of Q^2 between 0.4 and 1.8 (GeV/c)² that is used to extract cross sections from the experimental data. The chapter ends with a discussion of the statistical and systematic uncertainties in the extraction of separated cross sections.

In the sixth chapter the experimental cross sections are presented and the pion form factor is extracted from the data using the Regge model of Ref. [Van97]. Furthermore, the older data for F_π and the way they were extracted are discussed. In order to render the older data comparable to the ones presented here, the $Q^2=0.7$ (GeV/c)² DESY data are re-analyzed using the same model as for our data, and also the CEA/Cornell data are re-analyzed using information on σ_T from the present experiment. The chapter ends with a discussion of the findings.

The last chapter is a summary of the work presented in this thesis.

Chapter 2

Theoretical background and existing data

2.1 Introduction

The interaction of a photon with a charged pion is described by the matrix element*

$$(p_2 + p_1)_\mu F_\pi(Q^2) = \langle \pi(p_2) | J_\mu^{em} | \pi(p_1) \rangle, \quad (2.1)$$

where the amplitude F_π is the electromagnetic pion form factor and J_μ^{em} is the electromagnetic current operator, describing the coupling of the photon to the quarks. The operator is expressed in terms of quark fields q_f of flavor f and electric charges e_f as $J_\mu^{em} = \sum_f e_f \bar{q}_f \gamma_\mu q_f$. The incoming and outgoing pions have four-momenta p_1 and p_2 , respectively. The quantity $-Q^2$ is the square of the four-momentum of the photon.

At low values of Q^2 , F_π has been measured in the 1980's at Fermilab and CERN by scattering high-momentum pions off atomic electrons. In this case one was limited to values of Q^2 of up to $0.28 \text{ (GeV}/c)^2$. Higher momentum transfers can be reached in the $^1\text{H}(e, e'\pi^+)n$ reaction (see Fig. 2.1), where a high momentum electron scatters off a pion from the virtual pion cloud of the proton. This reaction was used in the present experiment and is discussed in Section 2.2. Although it provides data at higher values of Q^2 , the fact that the pion is produced on the proton means that it is off-shell before the interaction with the photon occurs. The implications of this for the extraction of F_π are discussed in Subsection 2.2.5.

*Throughout this thesis natural units are used, *i.e.*, $\hbar = c = 1$.

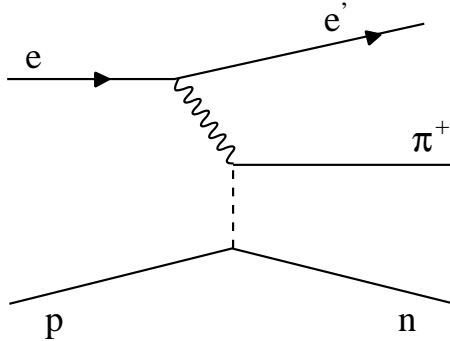


Figure 2.1: Schematic diagram representing quasielastic electron scattering off a pion in the proton.

The value of F_π is well known in the timelike region ($Q^2 < 0$) (e.g., Refs. [Ame84, Bar85, Bis89]) and for small spacelike (positive) values of Q^2 , where F_π is dominated by the ρ meson, with the normalization $F_\pi(Q^2 = 0) = 1$. Experimental F_π data in the spacelike region from earlier experiments are presented in Section 2.3. In the asymptotic limit of $Q^2 \rightarrow \infty$ there exists a rigorous prediction for F_π from perturbative Quantum Chromodynamics (pQCD). This and other calculations for F_π are discussed in Section 2.4.

2.2 Pion electroproduction

2.2.1 Kinematics

The kinematics of the $(e, e' \pi)$ reaction that has been used to study the Q^2 dependence of F_π is displayed in Fig. 2.2. The three-momentum vectors of the incoming and of the scattered electron are denoted by \mathbf{k} and \mathbf{k}' , respectively. Together they define the scattering plane. The corresponding four-momenta are k and k' . The electron scattering angle is θ_e . The transferred four-momentum $q \equiv (\omega, \mathbf{q})$ is defined by $q \equiv k - k'$. The square of the four-momentum vector $q^2 = q_\mu q^\mu = \omega^2 - |\mathbf{q}|^2$ is always negative in electron scattering. Therefore, one commonly defines $Q^2 \equiv -q^2$, which is positive. The three-momentum vectors of the neutron and the pion define the reaction plane. The angle between the scattering plane and the reaction plane is denoted by ϕ_π , the angle between \mathbf{p}_π and \mathbf{q} in the reaction plane is θ_π .

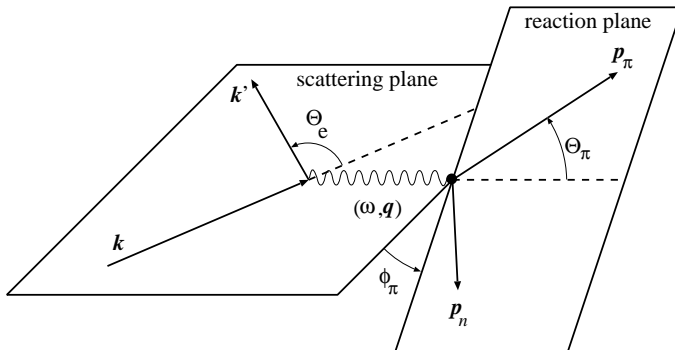


Figure 2.2: Representation of the $(e, e'\pi)$ reaction in the laboratory frame.

In the ${}^1\text{H}(e, e'\pi^+)n$ reaction the missing energy and missing momentum are defined as:

$$E_m = E_e - E_{e'} - E_\pi, \quad (2.2)$$

$$\mathbf{p}_m = \mathbf{q} - \mathbf{p}_\pi. \quad (2.3)$$

From these two quantities, one calculates the missing mass $M_m = \sqrt{E_m^2 - \mathbf{p}_m^2}$.

It is useful to describe the ${}^1\text{H}(e, e'\pi^+)n$ reaction in terms of three Lorentz invariants. In addition to Q^2 one uses the Mandelstam variables s and t . For the present reaction these are defined as

$$\begin{aligned} s &= (q + p_p)^2 = (p_\pi + p_n)^2, \\ t &= (p_\pi - q)^2 = (p_n - p_p)^2. \end{aligned} \quad (2.4)$$

Instead of s , the invariant mass of the photon-target system $W = \sqrt{s}$ is used here, which can be expressed as $W = \sqrt{M_p^2 + 2M_p\omega - Q^2}$. The quantity t is the square of the four-momentum transfer to the nucleonic system. It can be written as

$$t = (E_\pi - \omega)^2 - |\mathbf{p}_\pi|^2 - |\mathbf{q}|^2 + 2 |\mathbf{p}_\pi| |\mathbf{q}| \cos \theta_\pi. \quad (2.5)$$

In the present reaction t is always negative. The minimum value $-t_{\min}$ of $-t$ is reached for $\theta_\pi = 0$. The minimum value of $-t$ increases for increasing Q^2 and decreasing W .

2.2.2 Cross sections

In the one-photon-exchange approximation (OPE) the $(e, e'\pi)$ cross section can be written as the contraction of a lepton tensor $L_{\mu\nu}$ and a hadron tensor $W_{\mu\nu}$ [Mul90]:

$$\frac{d^6\sigma}{d\Omega_{e'}dE_{e'}d\Omega_\pi dE_\pi} = |\mathbf{p}_\pi| E_\pi \frac{\alpha^2}{Q^4} \frac{E_{e'}}{E_e} L_{\mu\nu} W^{\mu\nu}. \quad (2.6)$$

The lepton tensor can be calculated exactly in QED. The explicit structure of the hadron tensor depends on the specific process under investigation. If the final state is discrete as in the case of the $^1\text{H}(e, e'\pi^+)\text{n}$ reaction, the cross section reduces to a five-fold differential form:

$$\frac{d^5\sigma}{dE_{e'}d\Omega_{e'}d\Omega_\pi} = \Gamma_v \frac{d^2\sigma}{d\Omega_\pi}. \quad (2.7)$$

On the right-hand side of Eq. (2.7) the electron part of the cross section is contracted into a virtual photon flux factor

$$\Gamma_v = \frac{\alpha}{2\pi^2} \frac{E_{e'}}{E_e} \frac{q_L}{Q^2} \frac{1}{1-\epsilon}, \quad (2.8)$$

where α is the fine structure constant, the factor $q_L = (W^2 - M_p^2)/(2M_p)$ is the equivalent real-photon energy, which is the laboratory energy a real photon would need to produce a system with invariant mass W , and

$$\epsilon = \left(1 + \frac{2|\mathbf{q}|^2 \tan^2 \frac{\theta_e}{2}}{Q^2}\right)^{-1} \quad (2.9)$$

is the polarization of the virtual photon.

The result of the contraction of the lepton tensor and the hadron tensor is decomposed into four structure functions corresponding to the polarization states of the virtual photon: a longitudinal (L), a transverse (T) and two interference terms (LT and TT). The two-fold differential cross section in Eq. (2.7) can be expressed in terms of the structure functions as:

$$\frac{d^2\sigma}{d\Omega_\pi} = \epsilon \sigma_L + \sigma_T + \sqrt{2\epsilon(\epsilon+1)} \sigma_{LT} \cos\phi_\pi + \epsilon \sigma_{TT} \cos 2\phi_\pi, \quad (2.10)$$

where the σ_X , shorthand for $d\sigma_X/d\Omega_\pi$, depend on Q^2 , W and t .

The four structure functions can be separated if measurements are done at different values of ϵ and ϕ_π , while W , Q^2 and t are kept constant. The photon polarization ϵ can be varied by changing the electron energy and scattering angle (the so-called ‘‘Rosenbluth-’’ or L/T-separation). The angle ϕ_π can be varied by

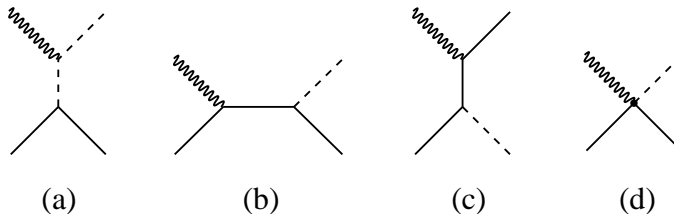


Figure 2.3: Born terms contributing to pion electroproduction: (a) pion-pole, (b) nucleon-pole, (c) crossed nucleon-pole, (d) contact (“seagull”) term. The wavy line, broken line and solid line represent the virtual photon, pion and nucleon, respectively.

measuring the pion left and right of the \mathbf{q} -vector (for σ_{LT}), and additionally out of the scattering plane (for σ_{TT}). At $\theta_\pi = 0$, that is if the pion is detected in the direction of the \mathbf{q} -vector (parallel kinematics), the interference terms are zero, and only σ_L and σ_T are left over.

2.2.3 Models for pion electroproduction

Born term models

In the one-photon-exchange approximation a single photon γ_v is assumed to be emitted by the scattered electron, which couples to the hadronic system. The amplitude for the process is described as a sum of Feynman amplitudes for all mechanisms that contribute to the process $\gamma_v + p \rightarrow \pi^+ + n$. In Fig. 2.3 the Born term diagrams that contribute to pion electroproduction are shown. Diagrams (a), (b) and (c) correspond to t, s and u-channel processes, respectively. Higher order processes involve, *e.g.*, nucleon resonances, additional pions, or the exchange of other mesons. When using pseudovector coupling of the photon the contact term (d) is needed to restore gauge invariance. Furthermore, when form factors are used at the vertices, they must be chosen such that gauge invariance is conserved.

In the context of the pion form factor the interest is focussed on the t-channel process, as it corresponds to the quasielastic scattering on a virtual pion (Fig. 2.1). Born term models (*e.g.*, Refs. [Ber70, Gut72]) indicate that for values of W above the resonance region and for small values of $-t$, the longitudinal part σ_L of the cross section for pion electroproduction is dominated by the t-channel process. Other processes contribute as well, but they are small in forward kinematics (at small

values of $-t$) and do not possess a pole[†] at $t = M_\pi^2$. At small $-t$ the t-pole term leads to the expression

$$\sigma_L \sim \frac{-t Q^2}{(t - M_\pi^2)^2} g_{\pi NN}^2(t) F_\pi^2(Q^2, t). \quad (2.11)$$

The fact that F_π in Eq. (2.11) depends also on t reflects the fact that the initial state pion is not free (see Subsec. 2.2.5). The factor $g_{\pi NN}(t)$ comes from the πNN vertex and can be seen as the probability amplitude to have a virtual π^+ meson inside the proton at a given t . It is generally parametrized in a monopole form as $g_{\pi NN}(0)/(1 - t/\Lambda_{\pi NN}^2)$ with $\Lambda_{\pi NN} \simeq 0.85$ GeV/ c . The precise value of $\Lambda_{\pi NN}$ is a matter of controversy and may vary between 0.4 and 1.5 GeV/ c depending on the context in which it is used. For instance, in models for meson exchange in nucleon-nucleon interaction it provides an effective description of the short-distance interaction with $\Lambda_{\pi NN} \gtrsim 1.3$ GeV/ c (Ref. [Mac87]). Lattice QCD calculations, however, give a value of $\Lambda_{\pi NN} = 750$ MeV/ c (Ref. [Liu95]) and QCD sum rule calculations yield $\Lambda_{\pi NN} \approx 800$ MeV/ c (Ref. [Mei95]). The value of $\Lambda_{\pi NN}$ will be examined using data from the present experiment in the thesis of K. Vansyoc (Old Dominion University, Norfolk, Virginia).

Regge model

More recently a Regge model of pion electroproduction has been developed by Vanderhaeghen, Guidal and Laget (VGL, Ref. [Van97]). In this model the exchange of high-spin, high-mass particles is taken into account by replacing the pole-like Feynman propagators of Born term models with Regge propagators. These include trajectories in the spin-mass squared plane (see Fig. 2.4). Effectively, the interaction is thus described by the exchange of a family of particles with the same quantum numbers instead of the exchange of one particle. As a consequence, the model predicts different W dependences for the contributions from the π and ρ trajectory exchanges, and hence for σ_L and σ_T .

Many of the parameters have been selected from the literature in such a way that the model describes charged pion photoproduction well. The pion form factor and the $\rho\pi\gamma$ form factor (F_ρ for short) are treated as free parameters. The pion form factor is parametrized with a monopole form as $F_\pi(Q^2) = [1 + Q^2/\Lambda_\pi^2]^{-1}$. Existing experimental data (Ref. [Beb78], see Section 2.3) are described well with $\Lambda_\pi^2 = 0.462$ (GeV/ c)². The ρ form factor is parametrized with a monopole form as well, but the cutoff parameter Λ_ρ is not as well constrained as Λ_π^2 . Gauge

[†]It should be noted that the pion pole cannot be reached experimentally since t is always negative.

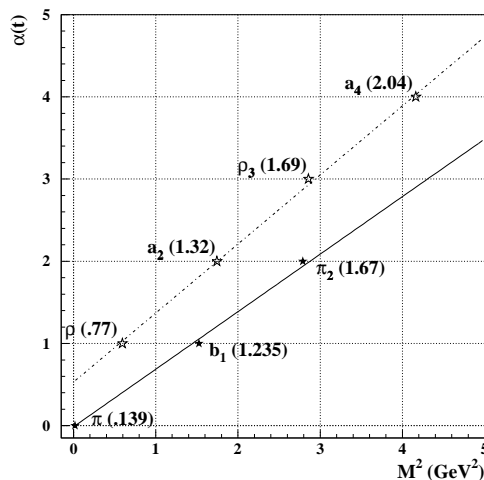


Figure 2.4: Regge trajectories $\alpha(t)$ for the π (solid line) and for the ρ -like mesons (dash-dotted) used in [Van97]. The variable t is the Mandelstam variable. Discrete values of α correspond to the spins of the particles.

invariance is implemented by taking the isovector proton form factor F_1^V equal to F_π . No $g_{\pi NN}(t)$ form factor is included in the model.

In Ref. [Van97] the authors compare the outcome of their model cross sections to experimental data (Refs. [Beb76, Ack78]). This is done for the Regge model and for a Born term model that is obtained by replacing the π and ρ Regge propagators by the corresponding π and ρ Feynman propagators. The Born term version of the model fails to describe the t dependence of the differential pion electroproduction cross sections at different values of W even if a t -dependent pion-nucleon form factor is included in the calculation. The agreement of the Regge model prediction with the data is satisfactory. Furthermore, data for π^-/π^+ electroproduction ratios from Ref. [Bra76] are described well in the Regge model.

In the VGL model the ρ exchange contribution has little influence on σ_L at small $-t$, while σ_T is sensitive to it. The authors conclude that their Regge model can be used to extract the pion form factor using experimental data at small values of $-t$. The sensitivity to the ρ exchange of the model prediction for σ_T may be used to estimate F_ρ within the model.

2.2.4 Isoscalar contributions

The t-pole contribution to σ_L is given in Eq. (2.11). If one is to rely on σ_L for the extraction of F_π , it is necessary to know whether the t-pole is indeed dominant in the kinematic region that is being studied. A way to estimate other contributions is to evaluate the contributions of isoscalar and isovector photon amplitudes A_S and A_V ($I=0$ and $I=1$, respectively[‡]) to the cross section. This is done as follows: During the present experiment, measurements were done for quasi-free π^+ and π^- electroproduction on a deuterium target at each kinematic setting. The ratio of the cross sections for these two reactions can be written in terms of isoscalar and isovector amplitudes A_S and A_V :

$$R \equiv \frac{\sigma(\gamma_n n \rightarrow \pi^- p)}{\sigma(\gamma_p p \rightarrow \pi^+ n)} = \frac{|A_V - A_S|^2}{|A_V + A_S|^2}. \quad (2.12)$$

As the t-channel reaction proceeds purely via isovector amplitudes, any deviation of R from unity indicates the presence of isoscalar processes. When σ_L and σ_T are extracted for both reactions it is possible to determine separately the ratios R_L and R_T as well.

At small values of $-t$, where the t-pole dominates, the photon couples to the charge of the pion. Since this is a purely isovector process, R should be unity. With increasing $-t$ the photon may probe individual quarks rather than the pions. In the limit of large $-t$, R is expected to approach $1/4$, the square of the ratio of the quark charges involved. Preliminary data on R indicate that this simple picture is qualitatively correct [Vol99a]. Preliminary data on the separate ratios R_L and R_T provide a more detailed picture: R_L is consistent with unity over the whole range in $-t$, while R_T decreases as a function of $-t$ [Mkr00pc]. These findings confirm the expectation that σ_L in the studied kinematical region is indeed dominated by the t-pole term.

2.2.5 Extraction of F_π

The off-shellness of the initial state pion needs to be addressed in the extraction of F_π from pion electroproduction data.

One approach to this problem is the Chew-Low extrapolation technique (Refs. [Fra59, Dev72]). If the data on σ_L lie on a smooth curve in a range in t , one can factor out the pole term $(t - M_\pi^2)^2$ from Eq. (2.11) and extrapolate to the pion pole in the unphysical region, at $t = M_\pi^2$. The extrapolation has two benefits: the off-shell

[‡]This is true for the electroproduction of charged pions. In other processes there may also be $I=2$ amplitudes.

character of F_π vanishes at the pion pole and non pion-pole contributions to σ_L are multiplied with $(t - M_\pi^2)^2$ and thus vanish at the pion pole, too. Drawbacks are the strong dependence on the choice of a fit function to the data (see *e.g.*, Ref. [Dev72]) and the possibly large error due to extrapolating in t (*e.g.*, $|t|_{\min} = 0.15 \text{ (GeV/c)}^2$ for $W=1.95 \text{ GeV}$ and $Q^2=1.6 \text{ (GeV/c)}^2$).

The approach used in the analysis of the present data (see Chapter 6) is to use a model like the VGL Regge model. The free parameters F_π and F_ρ are adjusted in such a way that the predictions for the separated response functions agree with the experimental data. This method of extracting of F_π is dependent on the the model parameters for both the π and ρ trajectories. The authors of Ref. [Van97] have shown, however, that σ_L from their model at small values of $-t$ is insensitive to the contribution from ρ exchange and therefore is a good indicator for F_π .

2.3 Existing data

The pion form factor is well known for small values of Q^2 from the scattering of high energy pions off atomic electrons. In this way F_π has been measured at Serpukhov, Fermilab and CERN with pion energies up to 300 GeV and values of Q^2 up to 0.28 (GeV/c)^2 [Ady77, Dal82, Ame86]. The results of the CERN experiment are shown in Fig. 2.5. The slope of F_π at $Q^2 = 0$ was used to determine the pion charge radius to be $0.662 \pm 0.006 \text{ fm}$.

The first pion electroproduction experiment above the resonance region ($W > 2 \text{ GeV}$) was done at the Cambridge Electron Accelerator (CEA) [Bro73]. In that experiment data were taken for $Q^2 = 0.18 - 1.19 \text{ (GeV/c)}^2$ at one high ϵ point only, so that σ_L could not be extracted. Instead, a Born term model [Ber70] was fitted to the unseparated $\sigma_T + \epsilon\sigma_L$ data with F_π as the only free parameter. A similar experiment was done at Cornell ("Cornell I") [Beb74] for $Q^2 = 0.62 - 2.01 \text{ (GeV/c)}^2$, and values for the pion form factor were extracted using the same model as in the Cambridge experiment.

Later work at Cornell ("Cornell II") [Beb76] added measurements for $Q^2 = 1.22 - 3.99 \text{ (GeV/c)}^2$ and included a re-analysis of the older CEA and Cornell I data. In the Cornell II data an isoscalar component was found in the unseparated response that had to be subtracted from the older data. Because of this, the values for F_π from those data were lowered by 3%-7%.

The third Cornell experiment ("Cornell III") added measurements at $Q^2 = 1.18 - 9.77 \text{ (GeV/c)}^2$, acquiring only low ϵ data [Beb78]. In the analysis it was attempted to combine the new data with older high ϵ data in order to extract σ_L and σ_T . However, while the low ϵ data span a range in Q^2 from 1.18 to 9.77 (GeV/c)^2 ,

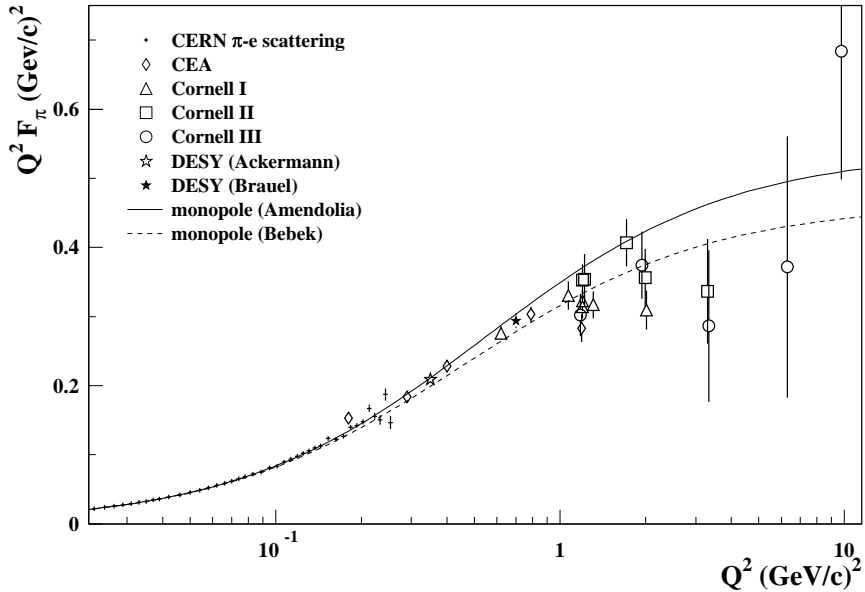


Figure 2.5: Semi-logarithmic plot of pion form factor data from CERN, the Cornell III analysis of the CEA, Cornell I, II and III data, and the DESY points. Error bars are statistical only. The dashed curve is the monopole fit to the Cornell III analysis results ($\langle r_\pi^2 \rangle^{1/2} = 0.711$ fm, Ref. [Beb78]), the solid curve is the monopole fit to the CERN data ($\langle r_\pi^2 \rangle^{1/2} = 0.662$ fm, Ref. [Ame86]).

the high ϵ data have a maximum Q^2 value of only 3.99 $(\text{GeV}/c)^2$. Consequently, the L/T separation could only be done in the overlap region. The uncertainties in σ_L , however, were very large so that the separated data were not used to extract F_π . Instead, σ_T was taken to be proportional to the total photoproduction cross section, which provided a reasonable description of σ_T in the region of low Q^2 . This contribution was subtracted from the data to get σ_L . The relation for σ_T was extrapolated to the high Q^2 region where only low ϵ data had been taken. The W dependence was assumed to be the same as that of the s - and u -channel Born terms. In the same publication, the older data (CEA, Cornell I and II) were re-evaluated using a Born term model by Berends (Ref. [Ber70]), which includes dispersion integral corrections to the cross section. The extraction of F_π from the data relied on the assumption that the longitudinal response is due to the t-channel

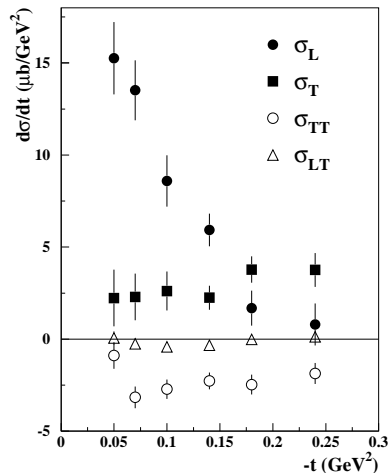


Figure 2.6: Separated differential cross sections for forward pion electroproduction at $Q^2 = 0.7$ (GeV/c) 2 and $W = 2.19$ GeV [Bra77].

one-pion exchange Born term. Therefore only data with angles $\theta_\pi < 3^\circ$ were used in the Cornell III analysis. The F_π data from this analysis are shown in Fig. 2.5. The error bars shown are statistical only. If one would include the systematic uncertainty (to be estimated for instance by the spread of the results from different measurements at comparable values of Q^2) and model dependences, *e.g.*, due to the assumptions used for σ_T , the total error bars would be typically at least twice as large, so that comparisons with theoretical data would have little discriminating power above $Q^2 = 1$ (GeV/c) 2 .

In two DESY experiments (Refs. [Ack78] and [Bra76, Bra77]) L/T separations were performed at Q^2 values of 0.35 and 0.7 (GeV/c) 2 and W values of 2.10 and 2.19 GeV, respectively. In both cases F_π was extracted using the Born term model of Ref. [Gut72], in which (off-shell) nucleon form factors were adjusted to fit the data. Furthermore the pion pole amplitude in Ref. [Gut72] was multiplied with a fitted exponential function, which the authors associate with the πNN vertex, in order to improve the fit to the unpolarized cross sections (*i.e.*, $\sigma_T + \epsilon\sigma_L$) from the data of Ref. [Dri71].

The separated differential cross sections for the $Q^2 = 0.7$ (GeV/c) 2 measurement (Ref. [Bra77]) are shown in Fig. 2.6. As expected, the longitudinal cross section dominates the cross section at low values of $|t|$. The transverse cross section σ_T

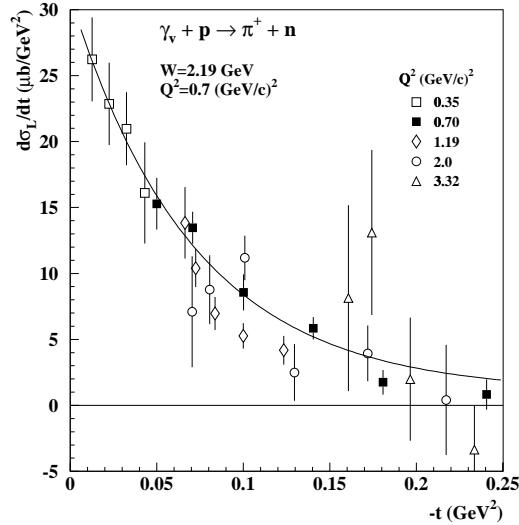


Figure 2.7: Longitudinal cross section for $\gamma_v + p \rightarrow \pi^+ + n$ from various Q^2 and W , scaled towards $W = 2.19 \text{ GeV}$ and $Q^2 = 0.7 \text{ (GeV/c)}^2$ (from Ref. [Bra77]).

increases slightly with increasing $-t$. The cross section σ_{TT} is consistently negative and σ_{LT} is small.

In the same publication similarities of data for σ_L in a range in W and Q^2 were studied for the data from the two DESY experiments and the Cornell III data set. Within the sizeable error bars the data follow a universal curve if they are scaled towards common values of Q^2 and W (see Fig. 2.7). The authors scaled the longitudinal cross section data assuming that the cross section is proportional to $Q^2 F_\pi^2(Q^2)$ and $(W^2 - M_p^2)^{-2}$. The scaled data can be parametrized with an exponential curve.

2.4 Calculations for F_π

In quantum theory the pion form factor is given by the overlap integral over the wave functions of the initial and final state pion [Rad91]

$$F_\pi(Q^2) = \int \phi_\pi^*(p) \phi_\pi(p+q) dp. \quad (2.13)$$

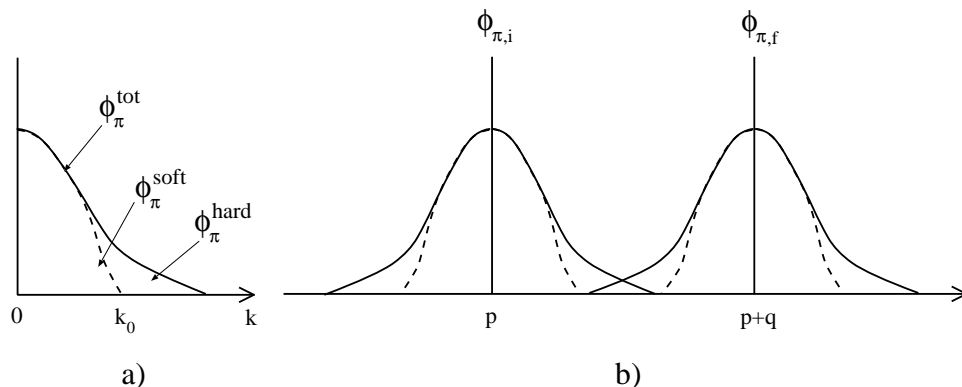


Figure 2.8: a) The total wave function (solid line) consists of a non-perturbative soft part ($k < k_0$, dashed line) and a perturbatively treatable high-momentum tail. b) Pion wave function overlap in momentum space.

As shown in Fig. 2.8, the pion wave function can be separated into a soft part (ϕ_π^{soft}) with only low-momentum ($k < k_0$) contributions and a hard tail (ϕ_π^{hard}) with the high-momentum contributions to the wave function. While ϕ_π^{hard} can be treated in perturbative QCD, ϕ_π^{soft} cannot. From the theoretical point of view the study of the Q^2 dependence of F_π thus focusses on finding a description for the soft and hard contributions to the pion wave function ϕ_π .

2.4.1 Asymptotic behaviour of F_π

At very high values of Q^2 the only contributions to the overlap integral Eq. (2.13) come from the $q\bar{q}$ valence quark Fock state and there ϕ_π can be taken to be the two-body bound-state wave function of the $q\bar{q}$ system. In order to study the behaviour of $F_\pi(Q^2)$ in the asymptotic limit (*i.e.*, in the limit $Q^2 \rightarrow \infty$) it is necessary to have a closer look at ϕ_π^{soft} and ϕ_π^{hard} .

Hard scattering picture

Lepage and Brodsky (Ref. [Lep79]) were the first to introduce the theorem that in the asymptotic limit lepton-hadron scattering processes can be separated into a soft part containing the long-range dynamics and a hard part due to the scattering kernel T_H for the high-momentum exchange between the lepton and the valence

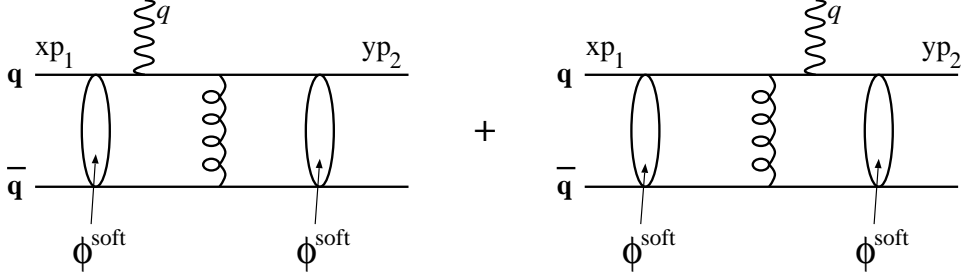


Figure 2.9: *Hard-scattering picture: one-gluon exchange diagrams contributing to the hard scattering amplitude. The quantities p_1 and p_2 are the total momenta of the pion in the initial and final state, x and y are the momentum fractions carried by the individual valence quarks in the initial and final state, respectively.*

quarks of the parton[§] (hard scattering picture, see Fig. 2.9). The overlap integral from Eq. (2.13) can thus be written as the sum of contributions from the purely soft overlap, which vanishes as $\mathcal{O}(1/Q^4)$ or faster, and the dominating integral over the hard contribution to F_π

$$F_\pi^{\text{HSP}}(Q^2) = \int \int dx dy \phi_\pi^*(x) T_H(x, y, Q^2) \phi_\pi(y). \quad (2.14)$$

The transverse momentum carried by the quarks is neglected in this formula. Thus the wave functions $\phi_\pi(q)$ are replaced by distribution amplitudes $\phi_\pi(x)$ and $\phi_\pi(y)$, where x (y) is the fraction of the pion momentum p_1 (p_2) carried by the individual quarks in the initial (final) state, with $0 < x$ (y) < 1 . The hard scattering kernel T_H is a sum over contributions from one-gluon exchange (OGE), two-gluon exchange and so on. At high values of Q^2 the OGE term dominates, since it decreases as $\mathcal{O}(1/Q^2)$, while all higher order terms vanish as $\mathcal{O}(1/Q^4)$ or faster.

Since in the limit $Q^2 \rightarrow \infty$ the OGE term dominates all others, Eq. (2.14) can be written as (Ref. [Far79, Lep79])

$$F_\pi^{\text{HSP}}(Q^2) \xrightarrow{Q^2 \rightarrow \infty} \int_0^1 \int_0^1 dx dy \frac{2g^2}{3xyQ^2} \phi_\pi^*(x) \phi_\pi(y), \quad (2.15)$$

where $g^2 = \frac{4\pi}{3}\alpha_s$ is the square of the quark-gluon coupling constant, and xyQ^2 is the “virtuality” of the exchanged gluon. The gluon virtuality sets the scale for the

[§]In this picture the hard pion wave function ϕ_π^{hard} can be identified with the high momentum components generated by the one-, two- etc. gluon exchanges.

running QCD coupling constant $\alpha_s(Q^2, \mu)$ and can be understood generally as a measure for the applicability of perturbative QCD to the interaction.

In the asymptotic limit $Q^2 \rightarrow \infty$ the pion distribution amplitude evolves into a simple form [Lep79] (see Fig. 2.10):

$$\phi_\pi(x) \xrightarrow{Q^2 \rightarrow \infty} \phi_\pi^{\text{as}}(x) = 6f_\pi x(1-x), \quad (2.16)$$

where the normalization factor $f_\pi = 133$ MeV, the pion decay constant, is known from the β -decay of the pion. Using Eqs. (2.15) and (2.16), one gets the prediction for the pion form factor

$$F_\pi(Q^2) \xrightarrow{Q^2 \rightarrow \infty} 8\pi\alpha_s f_\pi^2 / Q^2. \quad (2.17)$$

This result distinguishes F_π from the nucleon form factors, where the asymptotic behaviour is not known.

2.4.2 F_π at low Q^2 in perturbative QCD

Equation (2.17) is exact in the asymptotic limit of $Q^2 \rightarrow \infty$. Now one can look how well this formula can describe the existing data for F_π . Taking a typical value $\alpha_s \approx 0.3$ at low Q^2 ($\simeq 1$ GeV²), one finds that $Q^2 F_\pi(Q^2) \approx 0.13$. This value is by a factor of 3 lower than the existing experimental data (see Fig. 2.5). In the beginning it was not clear whether to attribute this discrepancy to soft contributions or whether it could be reconciled within perturbative QCD.

Chernyak-Zhitnitsky distribution amplitude

Chernyak and Zhitnitsky (CZ, Ref. [Che82]) made an attempt to reconcile the discrepancy within the framework of perturbative QCD. Neglecting soft contributions, they derived a pion distribution amplitude from QCD sum rules that differs from the asymptotic one at low values of Q^2 but evolves into ϕ_{as} in the limit $Q^2 \rightarrow \infty$. The distribution amplitude ϕ_{CZ} in the low- Q^2 limit is written as

$$\phi_\pi^{\text{CZ}} = 30f_\pi x(1-x)(1-2x)^2 \quad (2.18)$$

and is shown in Fig. 2.10. The definitions are as for Eq. (2.16). The use of ϕ_π^{CZ} in the overlap integral of Eq. (2.15) at low Q^2 increases the result by a factor of 25/9 with respect to the asymptotic result. This brings the prediction into agreement with the experimental data.

However, the approach with the CZ distribution amplitude was criticized for having most of the contributions come from regions with low x or y , where the gluon

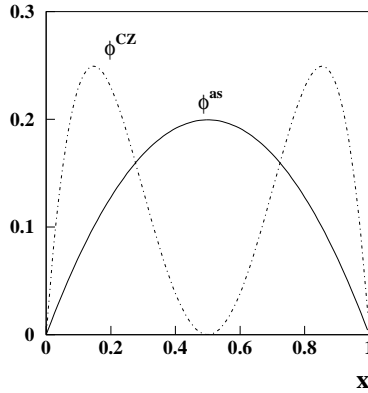


Figure 2.10: The asymptotic distribution amplitude (solid line) and the Chernyak-Zhitnitsky distribution amplitude (dash-dotted) as function of the quark momentum fraction x .

virtuality xyQ^2 is so small that the applicability of perturbative QCD is in doubt (Ref. [Isg84]). Further evidence against this approach came from the experimental side. The $\gamma^*\gamma\pi^0$ transition form factor was measured at DESY (Ref. [Beh91]) and at Cornell (Ref. [Gro98]). In the latter paper predictions from perturbative QCD calculations (Ref. [Jak96]) using the asymptotic and the CZ distribution amplitude are compared with the experimental data. The theoretical result calculated with the asymptotic distribution amplitude is in very good agreement with the data, whereas that from the CZ distribution amplitude lies significantly above the data.

Most recently, the diffractive dissociation of high momentum pions was studied at Fermilab (Ref. [Ash99]). In this process the pion breaks up on a nuclear target without imparting energy to it. The quark and antiquark hadronize into two jets whose total momenta are measured. This is in effect a direct measurement of the momentum distribution of the valence quarks in the pion, hence of the pion distribution amplitude. The preliminary results reported in Ref. [Ash99] conclude that for Q^2 values as low as 10 (GeV/c)² the pion distribution amplitude consists to more than 90% of the asymptotic distribution amplitude and to less than 10% of the CZ distribution amplitude. These results combined lead to the conclusion that the pion distribution amplitude is close to its asymptotic form even at values of Q^2 as low as 10 (GeV/c)².

Transverse degrees of freedom

Isgur and Llewellyn-Smith (Ref. [Isg84]) and Bakulev and Radyushkin (Ref. [Bak91]) raised the issue that at momentum transfers of a few (GeV/c) the contributions from the end point regions of the pion distribution amplitude where x or $(1-x)$ are close to zero cannot be calculated consistently in perturbative QCD, since at low values of xyQ^2 the coupling constant α_s becomes too big. The picture is modified when transverse degrees of freedom are included into the perturbative calculation.

Up to this point it had been assumed in the perturbative QCD calculations that effects due to the transverse momenta and the transverse separation of the valence quarks in the pions are negligible. Sterman *et al.* (Ref. [Ste89]) included Sudakov suppression into their calculation. This correction accounts for the fact that the amplitudes for the radiation of soft gluons from the individual quarks do not cancel when the quarks have a large spacial separation. This suppresses contributions from the end point regions. The authors conclude that the regime in which perturbative calculations can be done consistently is extended into the experimentally accessible region by the inclusion of Sudakov suppression.

However, by suppressing contributions from the end-point regions, the Sudakov suppression lowers the resulting value of F_π . Even when using the Chernyak-Zhitnitsky distribution amplitude $Q^2 F_\pi^{CZ}$ now lies below the data.

This work was followed up by Jakob and Kroll (Ref. [Jak93, Jak96]), who in addition to Sudakov corrections included an explicit transverse momentum dependence into the distribution amplitude. The term $(xyQ^2)^{-1}$ in Eq. (2.14) is replaced by $(xyQ^2 + (k_\perp + l_\perp)^2)^{-1}$, where k_\perp and l_\perp are the transverse momenta of the valence quarks in the initial and final state, respectively, and the singularity at $xyQ^2 \rightarrow 0$ is avoided. Through this modification the end point regions (and F_π) are suppressed even more strongly at low values of Q^2 than by Sudakov suppression alone. The authors conclude that through the inclusion of the intrinsic transverse momentum dependence of the pion distribution amplitude the consistency of perturbative calculations extends to values of Q^2 as low as $1-4$ (GeV/c)².

Perturbative leading-order calculations of $Q^2 F_\pi$ thus fall short of the experimental data by more than a factor of two. The missing strength is commonly attributed to soft contributions. These are estimated in Ref. [Jak93], where the authors find that with the asymptotic distribution amplitude the soft contributions have the right magnitude to explain the difference between perturbative contributions and the experimental data. In the case of the CZ distribution amplitude most of the strength is concentrated in the end point regions, so the estimated soft contributions are very large and lie clearly above the data. The calculations for both wave func-

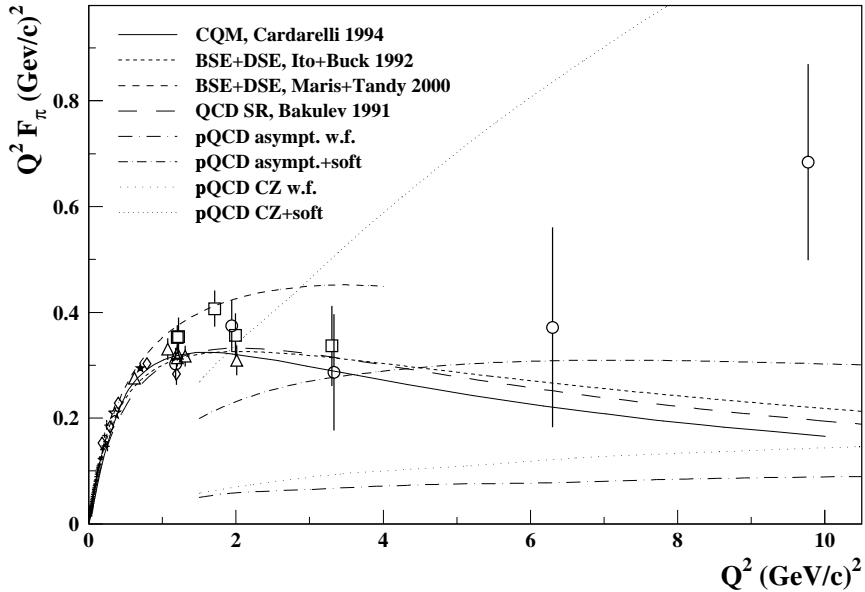


Figure 2.11: Pion form factor data as in Figure 2.5. The curves are from a constituent quark model (solid line, Ref. [Car94]), Bethe-Salpeter + Dyson-Schwinger equation (short dashed, Ref. [Ito92, Mar00]), QCD sum rules (long dashed, Ref. [Bak91]), perturbative QCD with the asymptotic distribution amplitude with and without estimated soft contributions (dashed-dotted, Ref. [Jak93]), and with the Chernyak-Zhitnitsky distribution amplitude (dotted, same reference).

tions with and without the estimated soft contributions are included in Fig. 2.11. The authors conclude that in the region of $Q^2 = 1 - 10 (\text{GeV}/c)^2$ more than 50% of the strength comes from soft contributions.

Recently, Braun *et al.* (Ref. [Bra00]) calculated soft and next-to-leading order (NLO) perturbative contributions to F_π . The authors found that though soft terms can be large, they partly cancel with NLO perturbative terms. Soft contributions and NLO perturbative contributions combined amount to only 30% in this calculation of F_π .

2.4.3 Models for soft contributions

Constituent Quark models

Constituent quark models are effective theories for the non-perturbative regime, which describe the pion as being composed of constituent quarks and with a wave function constructed from an effective $q\bar{q}$ interaction potential. The constituent quarks possess mass and a non-trivial electromagnetic structure. The models in Refs. [Chu88, Car94] incorporate a relativistic treatment of effective constituent quarks with masses $M_u = M_d = 0.220$ GeV and charge form factors. The $q\bar{q}$ interaction potential is composed of a linear confining term and a one-gluon-exchange term, which is dominant at short quark-separations and generates configuration mixing.

The authors in the more recent work (Ref. [Car94]) conclude that F_π is strongly affected by high momentum contributions to the wave function. For pointlike constituent quarks the best agreement with the experimental data on F_π up to Q^2 values of a few $(\text{GeV}/c)^2$ is achieved with a wave function that is constructed only from the confining part of the interaction, where the high momentum contributions to the distribution amplitude are weak. However, the pion charge radius is strongly underestimated if the full interaction potential is used. The agreement with the experimental value is restored when the constituent quarks are attributed a charge form factor with a corresponding quark charge radius of $\sqrt{\langle r_q^2 \rangle} = 0.480$ fm. The thus calculated F_π is also shown in Fig. 2.11.

Bethe-Salpeter equation and Dyson-Schwinger equations

The Bethe-Salpeter equation (Ref. [Sal51]) is an integral equation for the two-body bound state. It is a relativistic analogon of the two-body Schrödinger equation and describes the bound state distribution amplitude by means of the Bethe-Salpeter amplitude and an interaction kernel for the $q\bar{q}$ interaction.

An example where the Bethe-Salpeter equation is used within the framework of QCD is the work by Farrar and Jackson (Ref. [Far79]), who showed that in the asymptotic limit ($Q^2 \rightarrow \infty$) this approach leads to the $1/Q^2$ behaviour of F_π when using an interaction kernel derived from the one-gluon exchange mechanism. Jacob and Kisslinger (Ref. [Jac90]) used a wave function based on a potential fitted to the pion charge radius that lacked hard gluonic contributions and found that their model described the low- Q^2 behaviour of F_π . To investigate the behaviour of F_π at intermediate values of Q^2 , the authors chose an effective kernel for the Bethe-Salpeter equation consisting of a linear confining piece and a perturbative piece derived from

one-gluon exchange. The constraints at very low and asymptotic values of Q^2 were preserved in the model by using a pion charge radius of $\sqrt{\langle r_\pi^2 \rangle} = 0.644$ fm and a pion mass $M_\pi = 356$ MeV. The latter deviates significantly from the experimentally determined pion mass of 140 MeV. The authors comment that the model does not reproduce well the interplay between confinement and the effective quark mass, which enters into the calculation of the pion mass. The model predictions agree with the experimental data for F_π , whereby the perturbative part completely dominates over the nonperturbative contributions at $Q^2 > 15$ (GeV/c)² and contributes more than half of the strength already at $Q^2 \approx 5$ (GeV/c)².

A refinement to the Bethe-Salpeter models is achieved by accounting for medium effects in the quark propagator (dressed quarks). These effects are calculated using the Dyson-Schwinger equation, which yields a system of coupled integral equations for the contributions to the quark propagator from self-energy terms. The model parameters are fixed by requiring a good description of a range of pion observables. Ito, Buck and Gross (Ref. [Ito92]) used this technique to calculate F_π . In their model the self-energy term, which is calculated from the Dyson-Schwinger equation, is included in the calculation of F_π in terms of an effective quark mass. The interaction model is evaluated without gluon-exchange contributions. Its two parameters (the effective quark mass and a scale parameter) are fitted to f_π and the decay width for the $\pi \rightarrow \gamma\gamma$ process. With these parameters the F_π data are well reproduced, while the pion charge radius is overpredicted. The authors also investigate the influence of a two-body current and of vector mesons on F_π and find that both lower the prediction for F_π .

Maris and Tandy (Ref. [Mar98, Tan98]) calculate F_π using a Bethe-Salpeter amplitude with alternatively a bare-quark propagator and a Dyson-Schwinger equation solution for a dressed-quark propagator. The comparison with low- Q^2 data shows that the former calculation fails to describe the data while the Dyson-Schwinger equation approach agrees with the data and reproduces the experimental value for the pion charge radius to better than 10%. A new calculation by the same authors (Ref. [Mar00]) is based on this work. The model parameters are constrained by the pion mass M_π and the pion decay constant f_π . The calculation reproduces the pion charge radius to within 3%, but at higher values of Q^2 overpredicts the value of $Q^2 F_\pi$.

Dispersion relations and QCD sum rules

QCD sum rules are based on quark-hadron duality, *i.e.*, the possibility to describe the same object in terms of either quark or hadronic fields (*e.g.*, Ref. [Bak91]).

When applied to the pion form factor case the quark aspect is expressed in working out the matrix element $T(p_1^2, p_2^2, q^2)$ for the $\pi\pi\gamma$ vertex in the operator product expansion

$$T(p_1^2, p_2^2, q^2) = T^{\text{pert}}(p_1^2, p_2^2, q^2) + c_1 \frac{\langle GG \rangle}{(p^2)^3} + c_2 \frac{\alpha_s \langle \bar{q}q \rangle^2}{(p^2)^4} + \dots, \quad (2.19)$$

where p_1 , p_2 and q are the four-momenta of the initial and final pion and of the photon, respectively. The hadron aspect is expressed in the dispersion relation

$$T(p_1^2, p_2^2, q^2) = \frac{1}{\pi^2} \int_0^\infty ds_1 \int_0^\infty ds_2 \frac{\rho(s_1, s_2, q^2)}{(s_1 - p_1^2)(s_2 - p_2^2)} + \text{“subtractions”}. \quad (2.20)$$

The timelike spectral density $\rho(s_1, s_2, q^2)$ contains F_π and describes transitions between free-quark $q\bar{q}$ states with invariant masses s_1 and s_2 , respectively. Since a similar dispersion relation exists for T^{pert} one can combine Eqs. (2.19) and (2.20) and obtain an expression for F_π

$$f_\pi^2 F_\pi(Q^2) = \frac{1}{\pi^2} \int_0^{s_0} ds_1 \int_0^{s_0} ds_2 \rho^{\text{pert}}(s_1, s_2, q^2) e^{\frac{s_1+s_2}{2M^2}} + a \frac{\alpha_s \langle GG \rangle}{24\pi M^2} + b \frac{16\pi\alpha_s \langle \bar{q}q \rangle^2}{81M^4} + \dots, \quad (2.21)$$

where the coefficients a and b are specified by the operator product expansion and s_0 is the effective threshold for higher states production. The perturbative spectral density ρ^{pert} can be calculated, and the condensates are known phenomenologically. Using standard techniques to find optimal values for s_0 and M one gets a prediction for F_π that agrees well with the experimental data (see Fig. 2.11).

The authors of Ref. [Bak91] used this approach both to show that at values of Q^2 between 0-10 $(\text{GeV}/c)^2$ soft contributions dominate over hard contributions and that the derivation of the Chernyak-Zhitnitsky distribution amplitude from QCD sum rules is accompanied by large soft contributions.

2.4.4 Concluding remarks

Two results emerge from the discussion of the existing data and theoretical models. The data clearly show that at values of Q^2 of a few $(\text{GeV}/c)^2$ the pion form factor is largely dominated by soft contributions (see Fig. 2.11). Because of the way they were obtained, the experimental data for F_π at values of Q^2 above 3.3 $(\text{GeV}/c)^2$ cannot be trusted to describe the true Q^2 dependence of F_π , let alone to address the question at what value of Q^2 hard processes will provide, for instance, more than half of the strength of F_π .

The theoretical interest in the pion form factor also at lower values of Q^2 is evident from the range of available model calculations for F_π in the nonperturbative

regime. However, even at values of Q^2 below $3.3 \text{ (GeV}/c)^2$ the existing data suffer from large systematic uncertainties, which can be estimated from the range in F_π in which the data scatter. In this region of Q^2 , theoretical model predictions differ strongly. They disagree, for instance, in the position and the value of the maximum of the $Q^2 F_\pi$ distribution, which is constrained by the pion charge radius at low Q^2 and by the asymptotic behaviour at very high Q^2 . The existing data, however, do not have the accuracy that is necessary to constrain the models or to discriminate between them. New data for F_π with smaller uncertainties should therefore help to constrain models that are fitted to match the F_π data, and to discriminate between those that do not use the F_π data as an input.

Chapter 3

Experimental apparatus

The Pion Form Factor experiment described in this thesis was performed in Hall C of the “Thomas Jefferson National Accelerator Facility” (TJNAF) in the fall of 1997. This chapter gives an overview of the experimental apparatus used during the run period. Section 3.1 contains a brief description of the electron accelerator and the beam line instrumentation. The targets used are described in Section 3.2. The design and properties of the two spectrometers in Hall C are discussed in Section 3.3. Finally, the detector packages and trigger logic are reviewed in Sections 3.4 and 3.5.

3.1 Accelerator

The experiment made use of the unpolarized, continuous wave (CW, 100% duty factor) electron beam provided by CEBAF, the “Continuous Electron Beam Accelerator Facility”. This accelerator is designed to deliver beam currents of up to a total of 200 μA to three experimental halls simultaneously. The accelerator produces short beam bunches at a repetition rate of 1497 MHz, which are in turn delivered to each of the three experimental halls, resulting in a 2 ns bunch structure in each hall. The width of each bunch as measured in the injector is typically 1 ps*. The beam current can be adjusted for each hall individually in the injector.

The accelerator (Fig. 3.1) has a loop configuration of a pair of linear accelerators (linacs) interconnected through a series of recirculation arcs. In the standard

*This bunch structure is referred to as CW because the time spread in the arrival of events in the detectors of the two spectrometers is larger than the time between pulses. The distribution of events is thus quasi-continuous.

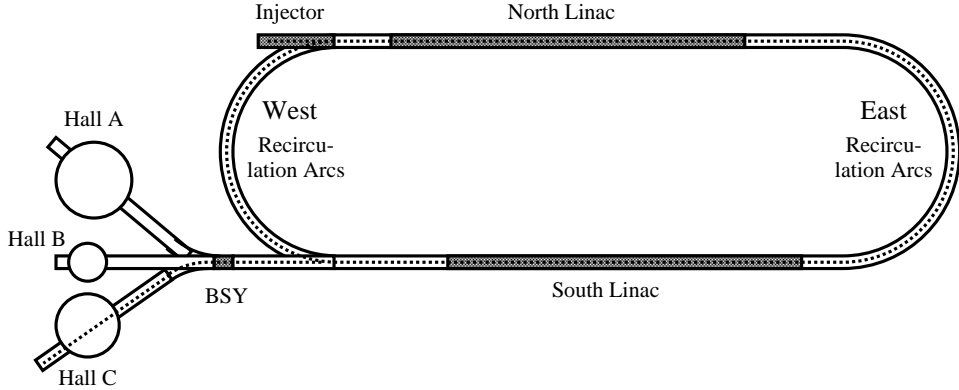


Figure 3.1: Schematic view of the CEBAF accelerator.

setting, electrons are injected into the North linac at an energy of 45 MeV[†] and undergo between one and five “passes” through the linacs and the arcs, in which the electrons gain 400 MeV per linac, or 800 MeV per pass. In this setup, the maximum total energy is 4.045 GeV. At the end of the second linac each beam pulse is either recirculated or directed towards the beam switch yard (BSY), where the successive pulses are directed in turn towards each of the three experimental halls. The linacs were tuned between approximately 370 and 440 MeV during the experiment, leading to energies of 2.448, 2.673 (3 passes), 3.007, 3.544 (4 passes) and 4.044 GeV (5 passes). The beam current delivered to Hall C was between 10 and 100 μA .

The beam is delivered through an arc into Hall C (see Fig. 3.2). This arc is equipped with a number of dipole and quadrupole magnets to steer and focus the beam. There are several monitors in the arc and in the beamline inside the hall to measure the position, profile, and current of the beam.

A beam profile monitor (“Superharp”) consists of a frame with three wires, one horizontal and two vertical. The frame is moved back and forth through the beam at an angle of 45°, thereby scanning the horizontal and vertical profile and position with a resolution of about 10 μm . Such a measurement is destructive and cannot be performed during data taking. The electron beam had a width of typically 100 μm at the target[‡].

[†]The electron energy at the end of the injector is fixed to 11.25% of the linac energy.

[‡]Throughout this thesis widths and resolutions are given by the standard deviation σ , unless stated otherwise

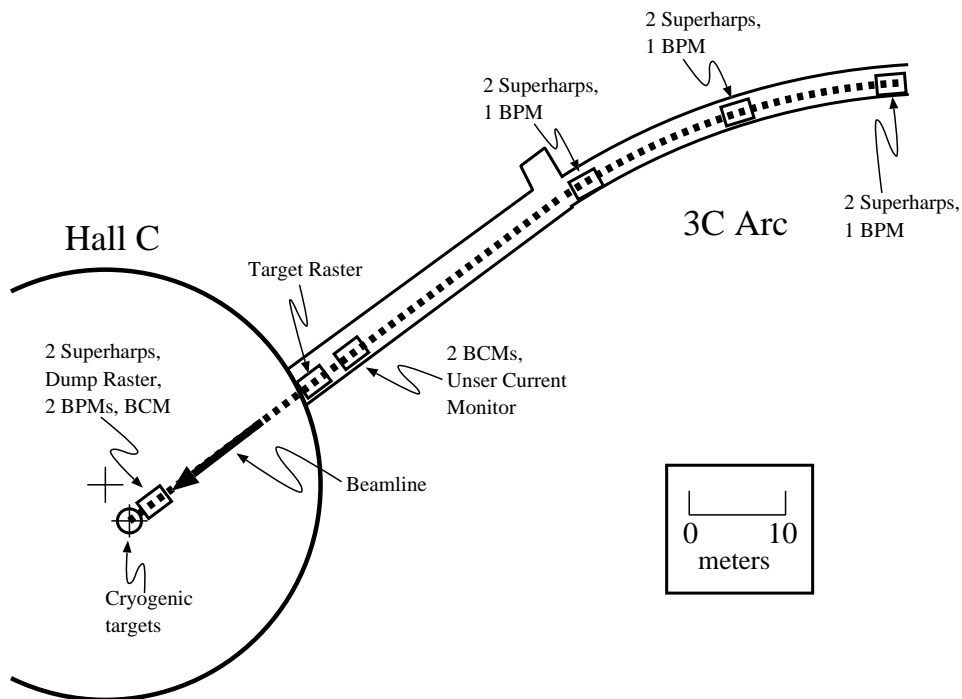


Figure 3.2: Schematic view of the arc and its instrumentation.

Five beam position monitors (BPM), three beam current monitors (BCM) and an Unser current monitor perform nondestructive measurements of beam positions and currents during data taking. The position and angle of the beam on target was determined from the information from the two BPMs closest to the target. The accuracy of the position measurement was 1 mm. The currents were measured to 0.5% precision. A detailed documentation of the beam current measurements and the calibration of the BCMS can be found in Refs. [Arm98, Kra93].

The beamline is also equipped with a pair of fast raster magnets. Their purpose is to reduce local density reductions of liquid targets due to the small size of the electron beam. The two fast raster magnets steer the beam in a sinusoidal pattern at 17 kHz in the vertical and 24.2 kHz in the horizontal direction. The result is a rectangular pattern with relatively more intensity at the edges of the rectangle (see Fig. 3.3). The ratio of frequencies is chosen to be close to $\sqrt{2}$. The close to irrational ratio helps to achieve a uniform distribution of the energy deposition in the target by preventing the formation of standing Lissajous patterns. The amplitude

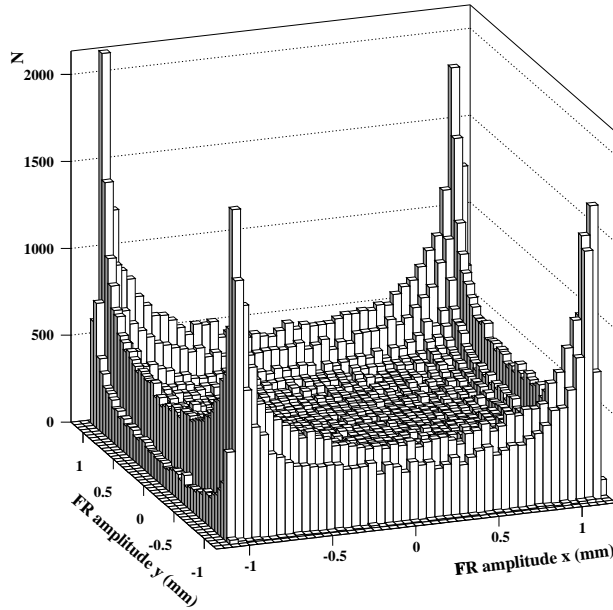


Figure 3.3: *Rectangular Fast Raster beam pattern on the target; the amplitude is 1.2 mm.*

of the raster pattern on the target was 1.2 mm in both directions during the present experiment. The raster position was recorded per event.

Electron energy measurements can be performed by using the arc as a spectrometer. For the energy measurement only the dipole magnets inside the arc are energized to bend the beam, the other magnets are degaussed in order to minimize residual fields. A couple of dipole corrector magnets are left on to correct for the earth's field. The dispersion of the arc is then 12 cm/%. The position and direction of the beam is measured using BPMs or Superharps at the entrance and the exit of the arc. This knowledge is combined with the well known field integral $\int B \cdot dl$ of the arc dipoles as a function of the current [Har89] to calculate the electron energy via the relation:

$$p = \frac{e}{\Theta_{arc}} \int B \cdot dl, \quad (3.1)$$

where p is the particle momentum, e is the electron charge and Θ_{arc} is the bend angle of the arc (34.40°). More detailed discussions of this technique can be found in Refs. [Jla99, CEB92, Yan93].

Several changes to the procedure were made for the present experiment. The cycling procedure for the arc dipole magnets was changed from a maximum current of 220 A to 300 A so that it would be consistent with the hysteresis curve with which the field integral data in the software were taken [Yan93]. Since the Superharps were not operational during parts of the experiment, the following procedure using the BPMs was adopted: the incoming beam was centered on the BPM at the arc entrance. The current in the dipoles was adjusted until the outgoing beam was centered on the BPM at the arc exit. The field integral was calculated using the dipole currents. This type of measurement was performed once at each energy. The results were later corrected by another method, which is discussed in Sect. 4.5.

3.2 Target and scattering chamber

The Hall C target ensemble consists of a three-loop cryogenic target stack together with an optics target assembly. The latter is designed for the calibration of the optics of the magnetic spectrometers (see Ch. 4). The target ensemble is mounted inside a vacuum scattering chamber in such a way that the stack of cryogenic cells and optics target can be moved up and down as a whole. The cylindrical scattering chamber has an inner radius of 61.6 cm and a height of 150 cm. The beam exit windows are made of 0.4 mm and 0.2 mm thick aluminium foils on the sides of the HMS and SOS spectrometers (see Sect. 3.3), respectively. The spectrometers are not vacuum-coupled to the scattering chamber.

Both the scattering chamber and the cryogenic target system are standard Hall C equipment and have been described in detail elsewhere [Mee98, Ter98]. Only the cryogenic target and the optics target are discussed in some detail in this section.

3.2.1 Cryogenic target

Fig. 3.4 shows the cryogenic cells. The cryogenic target consists of three loops for circulating cryogenic liquids with two target cells of different length in each loop. The long target cells were not used during the present experiment. Cooling is provided by helium at a temperature of 15 K. Loop 1 contains liquid hydrogen (LH_2), cooled down to 19.0 K and held at a density of $0.0723 \pm 0.0004 \text{ mg/cm}^3$ (at a pressure of 165.5 kPa). The second loop is kept empty. The third loop contains liquid deuterium, cooled to a temperature of 22.0 K and a density of

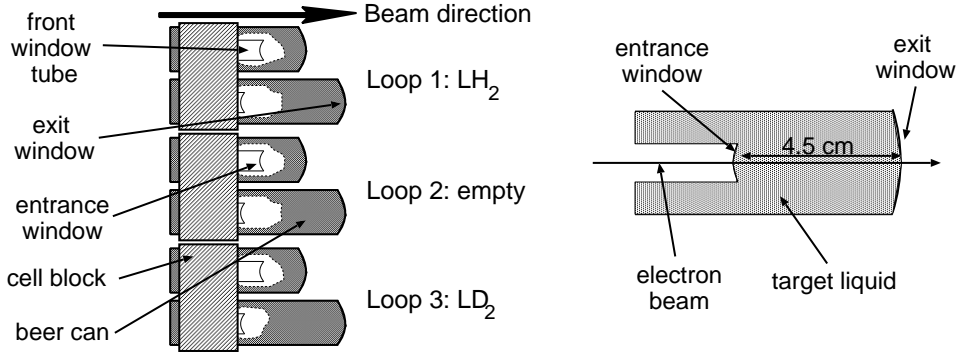


Figure 3.4: *Left: schematic view of the Hall C cryogenic cell stack. Each of the three loops contains two target cells. The cells consist of an inner and an outer cylinder, between which the target liquid flows. Right: vertical cut through one of the short target cells. The electron beam passes through 4.0 (LD₂) and 4.5 cm (LH₂) of target liquid. In the long target cells the distance is 12.5 cm.*

$0.167 \pm 0.001 \text{ mg/cm}^3$ (at 137.9 kPa). The chosen temperatures are 2 K below the boiling temperature. Samples of H_2 taken from the target system after the experiment were pure to better than 99.9%, samples of D_2 contained a hydrogen contamination of 1.7% [Gue98pc].

The entrance windows are made of $71 \mu\text{m}$ thick aluminium. The rest of the target cells consists of aluminium with thicknesses of $130 \mu\text{m}$ at the side and between $104 \mu\text{m}$ (loop 1) and $120 \mu\text{m}$ (loop 3) at the downstream end. The length of the short H_2 cell when cooled down is $4.53 \pm 0.01 \text{ cm}$. This value is derived from measuring the length at room temperature and correcting for thermal contraction (about 0.4% at 20 K). These and other information about the cryogenic target cells can be found in Ref. [Dun98].

3.2.2 Optics target

We designed a special thin target assembly (“Quintar”) for the optics calibration of this experiment. The design of this target incorporates three functions: an optics target, optimized for the experiment, that defines five interaction points along the beam axis (*cf.* Ch. 4); a dummy aluminium target imitating the walls of the 4.5 cm long LH₂ and LD₂ cells.

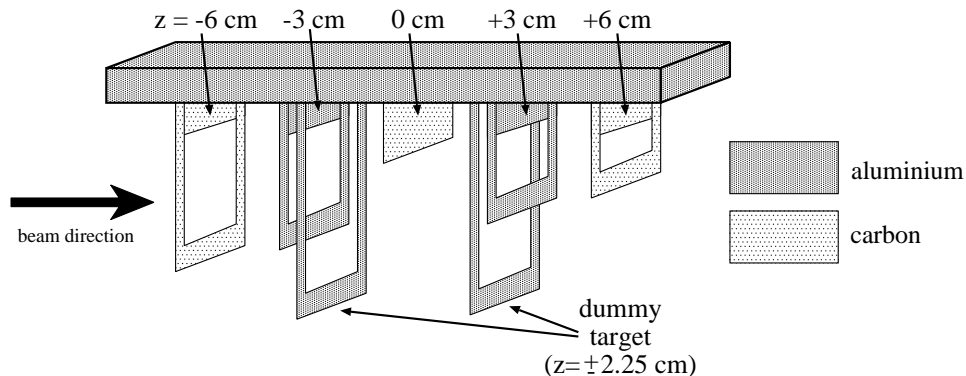


Figure 3.5: Schematic view of the optics target assembly “Quintar” (not to scale).

The design of the Quintar is shown in Fig. 3.5. Due to a combination of limited bellows travel and a shallow bottom of the scattering chamber, the vertical space for the optics target was limited to 8 cm. Five 1 mm thick and 7 mm high targets are mounted at a horizontal spacing of 3 cm. The target materials are carbon and aluminium. At ± 2.25 cm two more 1 mm thick aluminium dummy targets are mounted in order to simulate the walls of the 4.5 cm cryotarget cells, which themselves are about ten times thinner. The targets are shaped such that by moving the target stack vertically each single target (and the empty target pair) can be moved into the beam individually (see Fig. 3.5). In the lowest position all five optics targets are exposed to the beam simultaneously, excluding the dummy targets. At different vertical positions of the assembly one has either one of the five targets in the beam, and hence a precise calibration for the vertex position along the beam direction.

In previous experiments the interaction point of the beam with the target along the beam axis could be chosen continuously by vertically moving a solid target ladder with a slanted carbon target. This was a separate target ladder which had to be rotated into the electron beam. With that target arrangement the knowledge of the absolute target position along the beam axis depends on the knowledge of the precise vertical position of the target stack position with respect to the beam. This dependence is avoided with the new optics target assembly.

3.3 Spectrometers

Hall C is equipped with two medium resolution magnetic spectrometers, which both have relatively large momentum and solid angle acceptances (see Table 3.1). They are equipped with similar and highly versatile detector packages (see Sect. 3.4) so that they can both be used as an electron or as a hadron detector.

The design concepts of the two spectrometers are very different. While the High Momentum Spectrometer (HMS) with its maximum central momentum of 7.5 GeV/ c will accomodate the anticipated upgrade of the CEBAF accelerator to 6 GeV and more, the Short Orbit Spectrometer (SOS) with its short flight path is optimized for the detection of short-lived particles at the cost of its maximum momentum, which is about 1.75 GeV/ c .

During the present experiment the HMS was used to detect pions, because their momenta exceeded the maximum central momentum of the SOS. The pions had to be detected at very forward angles. In order to avoid interfering with the beam line, the magnetic configuration of the HMS had to be changed from its nominal (HMS-1) tune to a new optics tune (HMS-100, see Ch. 4). The necessary hardware changes are discussed in Sect. 3.3.1.

3.3.1 High Momentum Spectrometer

The HMS (Fig. 3.6) is a 25° vertical bend spectrometer with superconducting magnets in a $QQQD$ configuration, since its commissioning used in a point-to-point tune for the central ray (see Subsect. 4.1.1).

All magnets are supported by one carriage, which can be moved on rails around a rigidly mounted central bearing. The quadrupole string can be moved as a whole along the optical axis. A detailed description of the spectrometer hardware is given in Ref. [Arr98]. Performance specifications are given in Table 3.1.

A collimator box is attached to the first quadrupole, which contains two octagonal collimators of different size, a sieve slit and an empty frame. The octagonal collimators are made of 6.35 cm thick heavymet[§]. The sieveslit, made of the same material, is 3.175 cm thick. In the original HMS configuration with the HMS-1 tune the front face of the collimator is at a distance of 126.2 cm from the center of the target. A vacuum extension (“snout”) in front of the collimator box limits the amount of air between the target chamber vacuum and the vacuum inside the HMS to 15 cm. In this configuration the minimum central angle is 12.5°. In order to get to smaller angles, a new configuration was created by pulling back the string of

[§]Heavymet consists of 90% tungsten and 10% CuNi and has a density of 17.0 g/cm³.

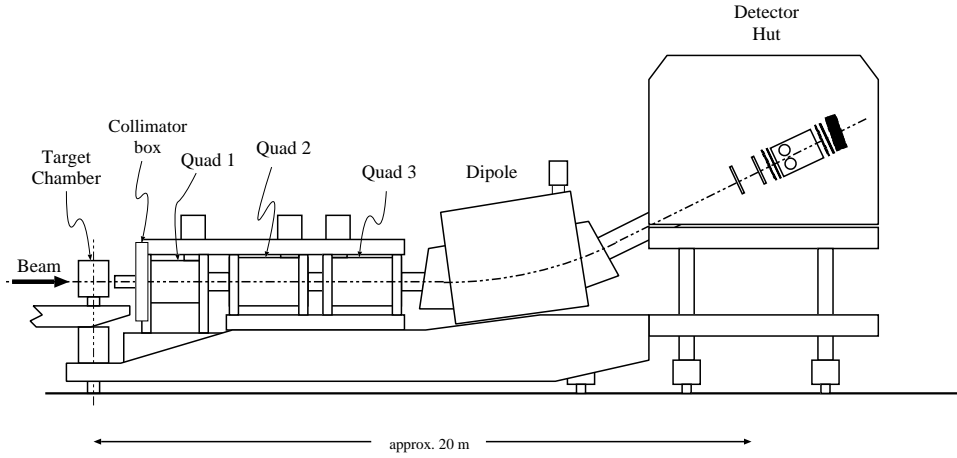


Figure 3.6: Schematic view of the High Momentum Spectrometer (HMS).

Quantity	Specification	
	HMS	SOS
Maximum Central Momentum	7.4 GeV/ c	1.75 GeV/ c
Optical Length	26.0 m	7.4 m
Angular Range	10.5° to 85°	13.4° to 165°
Momentum Acceptance	$\pm 10\%$	$\pm 20\%$
Momentum Resolution	$< 0.1\%$	0.1%
Solid Angle ^a	6.7 msr	7.5 msr
In-Plane Angular Acceptance ^a	± 27.5 mrad	± 57.5 mrad
Out-of-Plane Angular Acceptance ^a	± 70 mrad	± 37.5 mrad
In-Plane Angular Resolution	1.0 mrad	2.5 mrad
Out-of-Plane Angular Resolution	2.0 mrad	0.5 mrad
Extended Target Acceptance	± 7 cm	± 1.5 cm
Vertex Reconstruction Accuracy	2 mm	1 mm

^aThe solid angle and angular acceptances are given for the HMS-100 tune and for the large collimators in both the HMS and SOS spectrometers.

Table 3.1: Nominal specifications for the High Momentum Spectrometer and the Short Orbit Spectrometer. The angular range of the HMS is given for the HMS-100 tune.

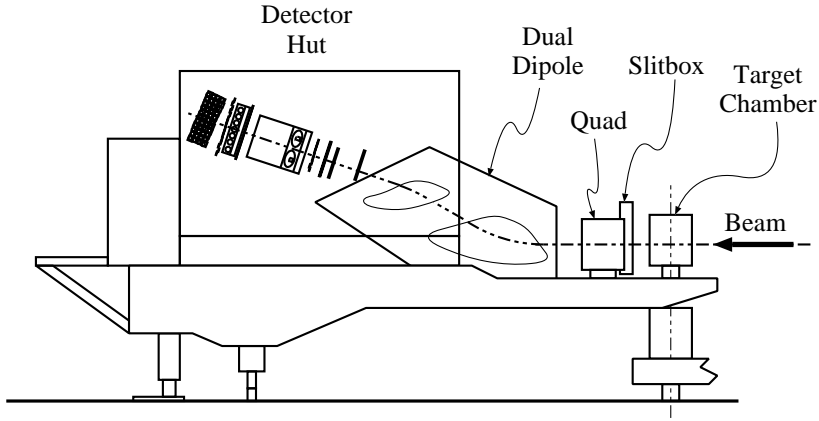


Figure 3.7: Schematic view of the Short Orbit Spectrometer (SOS).

quadrupoles and the collimator box by 40 cm, thus reducing the minimum central angle to 10.5° . A new tune (“HMS-100”) was necessary to achieve a point-to-point imaging in this new configuration.

From a Monte-Carlo study of both configurations [Vol96] it was concluded that the movement of the quadrupoles does not seriously affect the angular, target and momentum acceptance of the spectrometer. Therefore, a new collimator was built for the HMS-100 tune to match the angular acceptances of the large HMS-1 collimator (see Table 3.1). The surfaces on the inside of the octagonal slit are flared. A new vacuum extension became necessary because of the increased distance from the target to the collimator. Using Monte Carlo studies of beam envelopes, a longer snout was designed, built and installed, so that the HMS vacuum was extended again to 15 cm from the exit window of the scattering chamber.

3.3.2 Short Orbit Spectrometer

The design of the SOS (see Fig. 3.7) is based on that of the Medium Resolution Spectrometer at LAMPF [CEB90]. One quadrupole and two dipoles form a $QD\bar{D}$ configuration. The quadrupole focusses in the non-dispersive direction, the first dipole bends particles with the central momentum up by 33° and the second one bends them down by 15° . The SOS was also used in a point-to-point tune for the optical axis. The three magnets are non-superconducting and water-cooled. They rest on a common carriage. A collimator box with two octagonal collimators and a sieve slit is attached to the front of the quadrupole. Their materials and

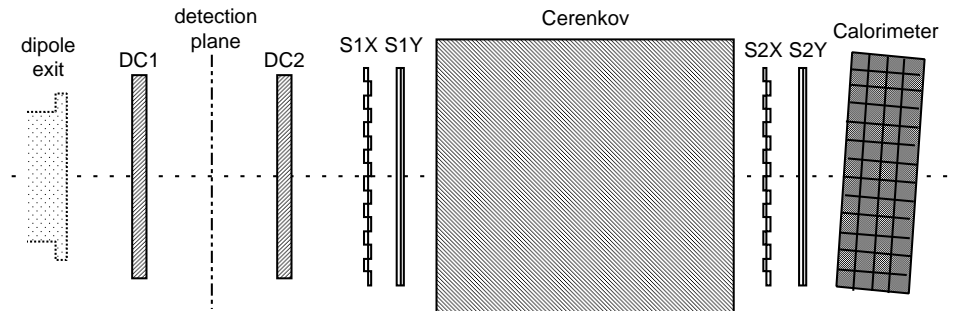


Figure 3.8: Schematic view from the side of the HMS detector package. The lead glass calorimeter is tilted at an angle of 5° relative to the central ray in order to prevent any losses that would result from particles travelling through the spaces between the blocks.

thicknesses are identical to those of the HMS. Likewise, a vacuum extension in front of the collimator box leaves a gap of 15 cm between the vacua of the target chamber and the SOS.

In addition to the quadrupole magnet, focussing is provided by the fringe fields arising from the curved shape of the pole tips of the dipole magnets. This makes the optics sensitive to magnet saturation effects at high field strengths (see Sect. 4.6). Specifications of the SOS are given in Table 3.1.

3.4 Detector packages

The detector packages of HMS and SOS, which are located in the detector huts of the spectrometers, are standard Hall C equipment. Detailed descriptions of all the components can be found in Refs. [Arr98, Mee98, Nic98, Wes99]. The detector packages of both spectrometers contain similar elements, though their dimensions differ. This similarity is crucial to making the HMS and the SOS interchangeable as electron and hadron detector.

Fig. 3.8 shows a schematic representation of the detector package of the HMS, which is representative for both spectrometers. A particle enters the hut through the dipole exit on the left. Two drift chamber packages (DC1 and DC2) provide information about the trajectory of the particle. A pair of scintillator hodoscopes (S1X and S1Y) is located before a gas Čerenkov detector, another one (S2X and S2Y) behind it. The last detector is a segmented electromagnetic lead-glass calorimeter.

3.4.1 Drift chambers

Both spectrometers are equipped with a pair of drift chambers. In all chambers the sense wires are spaced 1 cm apart. High spatial resolution is achieved by measuring the drift time of the free electrons that are created when a charged particle ionizes gas atoms on its way through the chamber. The necessary homogeneity of the electric field is achieved by surrounding the sense wires with non-sensing field wires in a rectangular pattern. Each drift chamber contains six planes of sense wires. The wires are strung in three (SOS) and four (HMS) different orientations in order to allow the measurement of the x and y position of a particle. The redundancy helps to resolve the ambiguity of multiple hits, to determine on which side of a wire a particle had passed (“left-right ambiguity”), and allows a single-chamber estimate of the particle trajectory (“stub”). A trajectory is fitted if the stubs found in the two drift chambers line up. The trajectory information of the two drift chambers is then combined to determine the track.

A description of the HMS drift chambers can be found in [Bak95]. The wire planes are ordered x, y, u, v, y', x' . The x and y planes measure the vertical and horizontal track position, respectively. The u and v plane wires are rotated by $\pm 15^\circ$ with respect to the x wires. This small angle makes the u and v planes x -like, with the effect that the redundancy in the x direction is good, but poor in the y direction. The position resolution for the HMS drift chambers is approximately $150\ \mu\text{m}$ per plane, which is mainly determined by multiple scattering of the passing particles in the drift chamber gas. The two drift chambers are placed at distances of 40 cm before and after the detection plane of the HMS. Prior to the present experiment, the HMS drift chambers were taken out of the hut and all the wires were replaced. After reinstallation the positions of the drift chambers in the hut were surveyed again. The drift chambers were replaced to within 1 mm of their original positions.

The planes in the SOS drift chambers are ordered u, u', x, x', v, v' . There are no explicit y planes, but the u and v wire planes are rotated by $\pm 60^\circ$ with respect to the x wires. As a result, the y resolution of the SOS detector is better than in the HMS. Unlike in the HMS, the wire planes form pairs with the sense wires offset by half a cell spacing (0.5 cm). That means that the left-right ambiguity is resolved if both planes of a pair are hit. The position resolution of the SOS drift chambers is approximately $200\ \mu\text{m}$ per plane. The two drift chambers are placed 25 cm before and after the nominal focal plane of the SOS.

3.4.2 Hodoscopes

The hodoscopes are located before and after the gas Čerenkov counter (see Subsect. 3.4.3). Each hodoscope consists of two scintillator planes. In the HMS the first plane of each hodoscope is segmented in the vertical, the second one in the horizontal direction. In the SOS the order is reversed. The hodoscopes serve two purposes: triggering of the data acquisition system and measuring the particle velocity using the time-of-flight between the two scintillator pairs. Each of the hodoscope segments (“panels”) in the HMS has a thickness of 1.0 cm and a width of 8 cm, with an overlap of 0.5 cm, while the corresponding panels in the SOS have thicknesses of 1.0 cm and widths of 7.5 cm, with an overlap of 0.5 cm. Each panel is read out by phototubes at both ends. The signals of all photomultipliers on each side of the plane are ORed and the signals from the two sides then are ANDed to form the signals S1X, S1Y, S2X and S2Y. The signal S1 (S2) is the OR of S1X with S1Y (S2X with S2Y). The role of the hodoscope signals in the trigger system is discussed in Sect. 3.5.

3.4.3 Gas Čerenkov counter

The Čerenkov counters are used to discriminate between electrons and other charged particles. The HMS gas Čerenkov detector is filled with Perfluorobutane (C_4F_{10}) at a pressure of 79 kPa, resulting in a refractive index of 1.0011, or equivalently a pion threshold of about 3 GeV/ c . The highest momentum pions in the present experiment were about 2.6 GeV/ c . The Čerenkov light is reflected by two parabolic mirrors and focussed onto two phototubes placed on top and at the bottom of the counter. The SOS Čerenkov detector has four such mirrors and four phototubes. Prior to the present experiment the old mirrors with spots of poor reflectivity were replaced by new mirrors. The detector is filled to a pressure of 101 kPa with Freon-12 (CCl_2F_2), with a refractive index of 1.00108, also yielding a pion threshold of 3 GeV/ c , well above the maximum momentum setting of the SOS. A more detailed description of the Čerenkov detectors can be found in Ref. [Wes99].

3.4.4 Lead-glass calorimeter

The lead-glass calorimeters are used to provide additional electron-hadron discrimination. They are built out of blocks of lead glass, measuring 10 cm x 10 cm x 70 cm, read out on one side, stacked four layers deep and 13 blocks high in the HMS (11 in the SOS). More detailed information about the calorimeter system hardware can be found in Ref. [Arr98].

3.5 Trigger system and data acquisition

The single-arm trigger logic for both HMS and SOS is shown in Fig. 3.9. The purpose of the single arm trigger logic is to generate a pretrigger signal when an electron or other particle arrives. Electron pretriggers (ELREAL) can be produced in two ways. A low-level electron trigger (ELLO) requires that at least two out of the three following conditions are met: at least one of the two scintillator layers of each hodoscope has fired (STOF = S1 AND S2); at least three of the four scintillator layers of both hodoscopes have fired (SCIN); the sum of the signals of the segments in the first calorimeter layer exceeds a low threshold (PRLO). This signal (ELLO) is vetoed by the negated Čerenkov signal. The second path, a high level electron trigger (ELHI) requires that all of the following conditions are met: the SCIN signal; the sum of the signals of the first calorimeter layer exceeds a high threshold (PRHI); the sum of all calorimeter signals exceeds a low threshold (SHLO). The electron trigger ELREAL is an OR of ELLO and ELHI. The idea behind defining two electron trigger paths is to provide redundancy, reduce trigger inefficiency and to make the best use of the electron-hadron discrimination by the Čerenkov detector and the lead-glass calorimeter. The low-level trigger ELLO is the Čerenkov signal in combination with good time-of-flight information (if SCIN is firing, STOF should be, too), or with some basic time-of-flight information and a calorimeter signal. The high-level trigger ELHI does not use the Čerenkov signal. Instead, it uses the full calorimeter information for electron identification, in combination with a good scintillator signal (SCIN).

The ELREAL signal is fanned out into four logic units with dead times set between 30 and 120 ns in order to allow a measurement of the electronic dead time (see Ch. 5).

The trigger for all other particles (PION) just requires the SCIN signal, vetoed by the Čerenkov signal. The possibility of using a prescaling circuit (PIPRE) in order to take prescaled PION triggers along with the electron triggers was not used. Some runs were taken with only the SCIN requirement on the electron arm.

The pretrigger signals of both spectrometers are fed into a trigger supervisor circuit (TS). The TS consists of two modules. One logic module has as input the pretriggers from the spectrometer trigger logic units and the TS control signals (GO, ENABLE, BUSY). Its output are HMS, SOS and COIN (coincidence) pretriggers and triggers, depending on the BUSY state of the TS. Both trigger and pretrigger signals are fed into scalers, providing information about the computer dead time. The trigger signals are then fed into a module that controls the processing of the trigger signals and initiates the readout of all ADC's and TDC's. A fourth kind

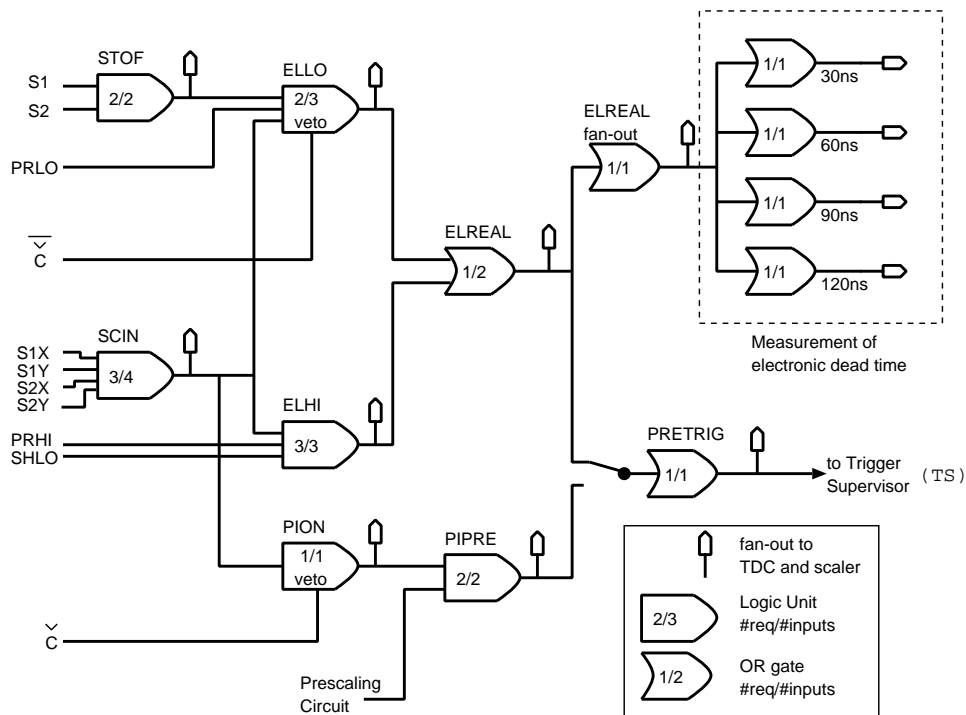


Figure 3.9: Schematics of the single arm trigger logic. Numbers like e.g. 2/3 inside the logic unit symbols indicate that two out of the three inputs to the unit must receive a logic 1 in order for the unit to produce an output.

of trigger events are pedestal events (PED). When starting a run, one thousand artificial events are created by the TS and recorded in all ADC channels in order to measure the threshold values of all channels. This is not possible during normal data taking, since, in order to reduce the number of data words per event, channels with ADC values consistent with the threshold are not written to disk.

The data acquisition software used in this experiment was CODA (CEBAF On-line Data Acquisition) version 1.4 [Abb95]. CODA ran on a Hewlett-Packard 735 workstation and performed the run control and event building. FastBus crate controllers and VME/CAMAC computers served as the interface between the data acquisition computer and the detector electronics. CODA merges the event fragments from the individual FastBus crates into complete events and writes them to disk. The runs are later backed up in the TJNAF tape storage facility.

Typical events rates handled by CODA and written to disk were several hundred Hz, with a data flow of several hundred kB/s at an average event size of approximately 1 kB.

Further details of the trigger supervisor, data acquisition and slow controls system are discussed in Ref. [Nic98].

Chapter 4

Spectrometer calibrations

The magnetic spectrometers of Hall C are discussed in this chapter. In Sect. 4.1 the description of the optical properties of magnetic spectrometers is given. Sect. 4.2 describes the procedure for finding new settings for the HMS quadrupole magnets after adapting the HMS configuration for small angles. Sect. 4.3 gives the methods of setting the HMS and SOS magnetic fields. The results of the optimization of the HMS and SOS matrix elements are discussed in Sects. 4.4.1 and 4.4.2. The determination of offsets (Sect. 4.5) and saturation effects in the SOS (Sect. 4.6) conclude this chapter.

4.1 Introduction to spectrometer optics

4.1.1 Definitions

In the pion form factor experiment the two magnetic spectrometers, HMS and SOS, were used to detect pions and electrons from the $^1\text{H}(e, e'\pi^+)\text{n}$ reaction, respectively. Before discussing the optical properties (“spectrometer optics”), it is necessary to give a number of definitions. The right-handed laboratory system is defined as follows:

- **z** points along the beam direction (downstream),
- **x** points to the right of the beam (looking downstream), in the horizontal plane,
- **y** points down towards the floor.

The spectrometer coordinate system is different [Blo86]:

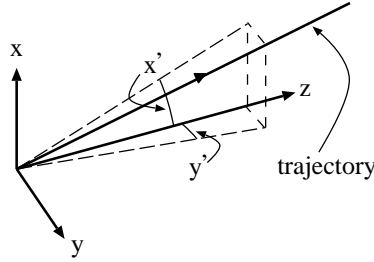


Figure 4.1: Definition of the angles x' and y' in the spectrometer coordinate system.

- z points along the optical axis at any point inside the spectrometer (see below),
- x points outwards in the bending (the dispersive direction), hence the xz plane coincides with the symmetry plane of the spectrometer,
- y completes the right-handed system in the non-dispersive direction.

A central ray is defined as the trajectory of a particle entering the spectrometer through the center of the entrance aperture, or in the case of the HMS and SOS along the optical axis of the first quadrupole magnet. The detection plane is defined as the plane in the middle between the two consecutive drift chambers detecting the charged particles. Taking p as the particle momentum and B as the central magnetic field of the dipole magnet, central rays for different values of p/B reach the detection plane at different positions. The optical axis is defined as the central ray that passes through a chosen point, the “center” of the detection plane. The momentum of particles traveling along the optical axis is called the central momentum p_0 or the “excitation” of the spectrometer.

Two frames in the spectrometer coordinate system are commonly used. One has its origin in the center of the detection plane. For historical reasons the subscript fp (focal plane) is used. However, in the case of the two spectrometers of Hall C, the focal plane and the detection plane do not coincide (see below). Thus by definition $z_{fp}=0$ at the detection plane. The trajectory of a particle in this frame is characterised by its values x_{fp} and y_{fp} in the detection plane and its angles x'_{fp} and y'_{fp} with respect to the yz and xz planes (see Fig. 4.1).

The other frame has its origin at the target (subscript tar). The trajectory of a particle in it is characterized by the two angles x'_{tar} and y'_{tar} (defined as above),

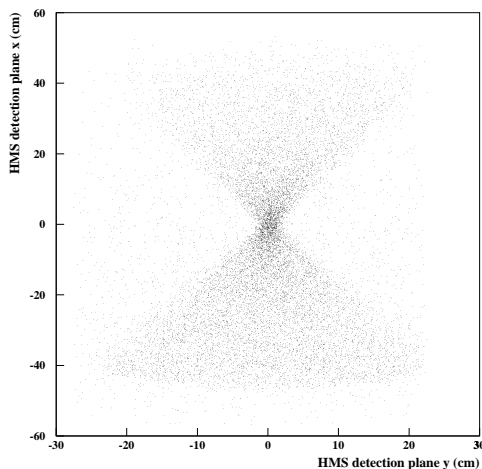


Figure 4.2: Typical “hourglass” distribution of pions in the HMS detection plane in a run with 4.5 cm long LH_2 target, $\Theta_{HMS} = 11.5^\circ$.

and the point of origin y_{tar} . It is assumed that $x_{tar}=0$ (see also Subsection 4.1.2). The particle momentum p is expressed relative to the momentum p_0

$$\delta = \frac{p - p_0}{p_0}. \quad (4.1)$$

The strengths of the quadrupole fields for a given field B of the dipole magnet, called the tune of the spectrometer, have been chosen such that for both HMS and SOS there is point-to-point focussing in both directions (x and y) for particles travelling along the optical axis, i.e. with $p = p_0$, or $\delta = 0$. For central rays with other values of δ the x focus of the HMS behaves in such a way that for $\delta > (<)$ 0 it is at $z_{fp} > (<) 0$. The behaviour of the y focus is more complicated: it moves from positive z_{fp} to $-\infty$ and then from $+\infty$ to negative z_{fp} , depending on δ . Fig. 4.2 shows the resulting x_{fp} , y_{fp} distribution in the detection plane. The waist of the hourglass distribution at $x_{fp}=0$, $y_{fp}=0$ is the point where x and y focal planes and the detection plane coincide.

4.1.2 Reconstruction of target quantities

The reconstruction of target quantities from focal plane quantities is done by means of a Taylor expansion [Blo87]:

$$a = \sum_{i,j,k,l} A_{i,j,k,l}^a (x_{\text{fp}})^i (x'_{\text{fp}})^j (y_{\text{fp}})^k (y'_{\text{fp}})^l, \quad i + j + k + l \in [0, N], \quad (4.2)$$

where $a \in (\delta, x'_{\text{tar}}, y_{\text{tar}}, y'_{\text{tar}})$, N is the order of the expansion, and $A_{i,j,k,l}^a$ are the elements of the reconstruction matrix. Note that δ (or p) is reconstructed, and not x_{tar} . Therefore, it has to be assumed that the beam is centered at $x_{\text{tar}}=0$ and that its vertical spread can be neglected. Because of the left-right symmetry of the spectrometers some matrix elements are zero. Those are called “forbidden” matrix elements. For instance, δ and x'_{tar} are left-right symmetric, and therefore δ and x'_{tar} matrix elements with odd values of $k + l$ in Eq. (4.2) are forbidden. On the other hand, y_{tar} and y'_{tar} matrix elements have antisymmetric dependences on y_{fp} and y'_{fp} . Therefore y_{tar} and y'_{tar} matrix elements with even $k + l$ are forbidden. If the midplane symmetry of the spectrometer is broken, these forbidden matrix elements may have non-zero values.

The matrix elements have to be optimized, which is done in the following way: First the HMS and SOS magnetic properties are modelled with the COSY INFINITY program [Ber95]. The model reconstruction matrix is taken as starting point of a fitting procedure. The matrix elements are fitted to optics calibration data, including:

- *δ scans*: The momentum of elastically scattered electrons is well defined and depends only on the incoming electron energy, the scattering angle and the mass of the target nucleus. Protons and ^{12}C nuclei were used as target nuclei. The elastically scattered electrons occupy a narrow band in the detection plane. This band is moved across the focal plane by changing either the field (and thus p_0) or the angle of the spectrometer.
- *y_{tar} scans*: Different vertex points along the beam axis are generated by using the five targets of the quintar (see Subsection 3.2.2). The data are taken in the resonance region in order to assure full δ coverage.
- *$x'_{\text{tar}}, y'_{\text{tar}}$* : Electrons with discrete values of x'_{tar} and y'_{tar} are generated by doing the y_{tar} scan with sieve slits instead of the octagonal collimators. The sieve slits are 3.175 cm thick heavymet plates (see Section 3.3) with a regular pattern of holes (see Subsections 4.4.1 and 4.4.2).

For an extensive discussion of the fitting procedure see Ref. [Ass97]. The first step is to merge the δ -scan runs into one run. Care is taken that electrons are selected inside the band region occupied by elastically scattered electrons in the detection plane. In a similar way the runs from the y_{tar} scan taken with the five targets of the quintar are merged.

In the fitting program (CMOP, Ref. [Wel94]) the fitting of x'_{tar} and y'_{tar} matrix elements is done by reconstructing the target variables from the measured focal plane variables for each event by means of the Taylor expansion of Eq. (4.2). Using the reconstructed target variables, the particle is projected to the sieve slit and the hole closest to the trajectory is determined. If the distance to that hole is smaller than a predefined cutoff value, the event is retained for a fit of the matrix elements, with the distance as weight in the fit. In the first iteration of the fitting procedure the model reconstruction matrix is used. In the following iterations the reconstruction is done with the matrix derived in the previous iteration.

The fitting of matrix elements for the δ and y_{tar} reconstruction works similarly, but instead of using the proximity to a sieve slit hole, the selection criterium (and weight) is taken to be the difference between the reconstructed and the calculated particle momentum and the distance between the reconstructed and the known y_{tar} , respectively.

4.2 The HMS-100 tune

In the present experiment for the first time particles in the HMS had to be measured at central angles as small as 10.5° . Since the minimum angle prior to the present experiment was 12.5° , when the first quadrupole magnet would hit the beampipe downstream of the target, this angle could not be reached with the standard HMS configuration (“HMS-1”). In order to make room, the string of three quadrupole magnets was pulled back by 40 cm (see also Ch. 3). Since the magnetic configuration of the spectrometer was changed, the strengths of the magnetic fields of the quadrupole magnets had to be altered in order to restore a point-to-point focus.

New values for the quadrupole field strengths were obtained from a TRANSPORT simulation [Bro80] with the new magnet positions. Because the effective field lengths of the quadrupole fields were only known to approximately 1%, the TRANSPORT values were multiplied with the ratio between empirical values and TRANSPORT values for the old HMS-1 tune. With these adjusted magnet settings sieve slit data of inelastically scattered electrons* were obtained and the location

*The field strength of the dipole magnet was chosen such that the 4.4 MeV excited state of ^{12}C lies at $x_{\text{fp}}=0$ in the detection plane.

	x focus	y focus
$\frac{dz}{dQ_1}$	-36 cm/%	+40 cm/%
$\frac{dz}{dQ_2}$	+21 cm/%	-286 cm/%
$\frac{dz}{dQ_3}$	-27 cm/%	+57 cm/%

Table 4.1: *Dependence of the movement in the z direction of the x and y focal planes on changes of the quadrupole field strengths. The values were obtained with TRANSPORT studies.*

in z_{fp} and x_{fp} of the interception of the x and the y focal planes was identified. The criterion for this was that the x_{fp} and y_{fp} positions are independent of x'_{tar} and y'_{tar} , respectively. The dependence of the movement in z_{fp} of both foci on the quadrupole field strengths (Q_1 , Q_2 and Q_3 for short) known from TRANSPORT studies (see Table 4.1) was used to calculate improved values for the quadrupole settings, whereby the ratio $Q_1:Q_3$ was held fixed. After two iterations, the interception point converged at $x_{fp}=y_{fp}=z_{fp}=0$. The new configuration and tune was named “HMS-100”.

4.3 Magnet setting and cycling

4.3.1 HMS quadrupole magnet setting procedure

Since the commissioning of the HMS in 1994 it had been observed that the point of interception of the x and the y foci changed as a function of the excitation of the spectrometer [Ent99pc]. The clearest signal was that the waist of the hourglass distribution in the detection plane (Fig. 4.2) shifted by up to seven centimeters from the lowest excitation of a few hundred MeV/ c to the highest excitation of 4 GeV/ c . The explanation is that the ratio of the field integrals of the quadrupole and dipole magnets changed as a function of the spectrometer excitation.

The problem was that the superconducting quadrupole magnets are set by current. In the original magnet setting program the dependence $B(I)$ of the magnetic field B on the current I was assumed to be linear without residual fields. In order to be able to account for such residual fields in a new magnet setting program we measured the hysteresis curves of the quadrupole fields, using Hall probes placed close to the pole tips in the center of the magnets. The measurements revealed that there are non-negligible residual fields in all three quadrupole magnets. Taking into account residual fields in the magnet setting procedure is particularly important

because the third quadrupole magnet (Q3) is operated at very small fields, and hence a tune measured at low excitation will scale poorly with current. To account for these effects, we added an offset B_0 to the linear response:

$$B^\pm(I) = \pm B_0 + \alpha I. \quad (4.3)$$

The $+$ and $-$ signs denote positive and negative current I in the magnets, respectively.

In using this parametrization one has to make sure that the magnets are reproducibly set on the hysteresis curve that has been parametrized. The quadrupole magnets are set on the downward slope of the hysteresis curve. An effective and fast procedure for setting the HMS quadrupole magnets was found to be[†]:

- After polarity changes, remnant residual fields from the previous polarity setting are eliminated by ramping the current to 500 A, and back to 0 (the magnets do not have to be cycled again until the next polarity change).
- If the next setpoint is higher than the previous one, the current is ramped to a value 100 A higher than the required setpoint, but at maximum to 500 A. Then the current is ramped down to the setpoint.

If the next setpoint is lower than the previous one, the new setpoint is set directly.

The reproducibility of the magnetic fields is at the level of one part in 10^4 .

The result of the new setting procedure and the new parametrization of the hysteresis curves is a stability of the waist of the hourglass distribution to within ± 0.5 cm for excitations ranging from 0.8 to 3.2 GeV/ c^\ddagger .

4.3.2 HMS dipole magnet setting procedure

The HMS dipole magnet is equipped with an NMR (nuclear magnetic resonance) probe and is set by field. The magnet is cycled when the polarity is switched. The cycling is done by ramping the current up to a value of 1500 A, which corresponds to a magnetic field of 1.28 T (or an excitation of 4.6 GeV/ c) and then ramping down to the setpoint.

Setting the dipole magnet to a new setpoint is done by ramping the current to a value near the setpoint. When the current is near the setpoint, a field control

[†]The procedure is described here for positive currents only because it is mirrored in positive and negative polarity.

[‡]This was the range of HMS excitations during the present experiment. Later experiments report that the stability of the hourglass distribution extends to even lower and higher excitations.

program using the feedback from the NMR probe is started. The program initiates a setting procedure for the dipole magnet involving overshooting the setpoint, followed by an undershoot, before the setpoint is reached. The values of the overshoot and the undershoot depend on the difference with the previous setpoint. At both levels the magnet is allowed to settle for two minutes. Once the setpoint is reached, the magnet is allowed to settle for seven minutes. After that the field control program regulates the current in order to stabilize the field to within one part in 10^5 .

4.3.3 SOS magnet setting procedure

The SOS magnets are equipped with Hall probes and are set by field. The setting procedure is such that the residual fields are set to zero (*i.e.*, the magnets are “degaussed”) and then the magnets are set on the upward slope of the hysteresis curve. Once on that curve, higher setpoints can be reached without degaussing. If either the polarity is changed or a lower setpoint is needed, the magnets have to be degaussed. The degaussing procedure is as follows:

1. ramp down to 0 and switch polarity, if needed,
2. ramp up to the maximum current of 1000 A,
3. return to 0, switch polarity, and ramp to a current around 200 A. This sets the magnet onto a hysteresis curve with no residual field at 0,
4. return to 0, switch polarity, and ramp to the setpoint.

At every stage the magnets have to settle for two minutes. Repeated degaussing cycles show a short term reproducibility in the Hall probe readings of ± 1.5 G. The long term stability of the Hall probes on a time scale of a few months is of the order of a few parts in 10^4 [Pot99pc].

4.4 Results from matrix element fitting

4.4.1 Results for the HMS

The HMS was set at an angle of 15° during all of the optics data taking. The following data were used for fitting matrix elements:

- *δ -scan*: Using a one-pass beam with an electron energy of 0.850 GeV, the HMS detected electrons that had scattered elastically off a thin ^{12}C target. The excitation of the HMS was changed in eleven steps from 0.9327 GeV/ c ($\delta=+13.1\%$) to 0.7555 GeV/ c ($\delta=-8.4\%$).

- *y_{tar}-scan*: In this case a continuous δ spectrum is needed. Using a three-pass beam with an energy of 2.673 GeV, the HMS, set to $p_0=2.2$ GeV/c, detected inelastically scattered electrons passing through a sieve slit. Measurements were done with all targets of the quintar.

The position of the target with respect to the HMS mid-symmetry plane is deduced from the focal plane pattern of the particles originating from the five targets of the quintar that pass through the central hole. Events coming through the central hole form a line with $y_{fp}=0$ and $y'_{fp}=0$ when plotting x_{fp} versus y_{fp} and y'_{fp} , respectively, if the central target is exactly in the mid-plane of the spectrometer. If the target is not in the mid-plane, the lines will be tilted and shifted to $y_{fp} \neq 0$ and $y'_{fp} \neq 0$ at $x_{fp}=0$. From the measured data the position of the central target was determined to be -0.45 cm in the beam- z direction with respect to the symmetry plane of the HMS.

The HMS reconstruction matrix was expanded up to fifth order in the fitting. Fitting strategies included gradually decreasing the cutoff for the distance of a trajectory to the nearest sieve slit hole, giving more weight to areas in phase space that are scarcely populated, and gradually opening up forbidden matrix elements (up to fifth order). The latter improved the reconstruction significantly, especially for y_{tar} and y'_{tar} . It was later found [Pot99pc] that the breaking of midplane symmetry (which leads to forbidden matrix elements) is most likely caused by a rotation of Q2 by 0.2° around its optical axis.

Fig. 4.3 displays the sieve slit reconstruction of the HMS, overlaid with the nominal hole positions and the acceptance as defined by the HMS-100 octagonal collimator. The center of the sieve slit is located at a distance of 168.0 cm from the center of the target. It has holes of 0.508 cm diameter, grouped in seven (nine) columns at intervals of 1.524 cm (2.540 cm) in the horizontal (vertical) direction, corresponding to steps in x'_{tar} and y'_{tar} of 15.1 mrad and 9.1 mrad, respectively. The central hole has a diameter of 0.254 cm. As a check of the sieve slit orientation there are no holes at $+1.524$ cm/ $+2.540$ cm and -1.524 cm/ -5.080 cm. The outermost vertical sieve slit holes are at ± 10.160 cm, corresponding to ± 60.5 mrad. For particles passing the octagonal collimator beyond this range the reconstruction relies on the extrapolation of the Taylor series (Eq. 4.2) to a region where it has not been fitted, and the resolution worsens considerably. Therefore only a range of ± 60 mrad in x'_{tar} was used during the analysis of our π^+ data.

Fig. 4.4 shows the reconstruction of the z_{tar} position of the five quintar targets, and the reconstruction of the sieve slit holes in the vertical (x') and the horizontal direction (y'). The distributions in the z_{tar} reconstruction have strong non-Gaussian

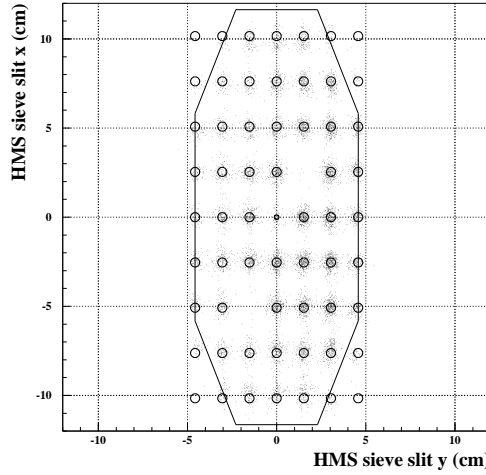


Figure 4.3: Reconstruction of the HMS sieve slit hole pattern. Overlaid is the acceptance as defined by the octagonal collimator. The lack of events in the sieve slit holes in the corners is caused by limited acceptance. Data from all five quintar positions are displayed together.

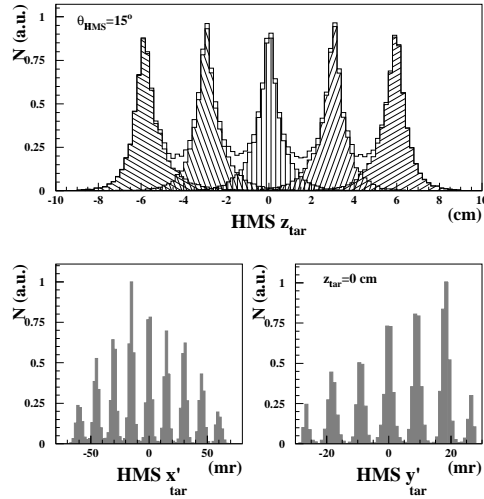


Figure 4.4: HMS quintar and sieve slit reconstruction. Top: reconstruction of the quintar z_{tar} co-ordinate. The distribution shown is the sum of the five individual targets. Bottom: reconstruction of the vertical (left) and horizontal (right) sieve slit hole patterns (central target only).

tails, because the y_{tar} resolution in the HMS is strongly δ dependent. Near the peak of the distributions the value of σ is typically 0.4 cm, corresponding to approximately 0.1 cm in the variable y_{tar} , since the HMS was facing the target at an angle of 15° . As a result of the non-Gaussian tails the mean y_{tar} resolution is 0.2 cm.

The σ values of the peaks in x'_{tar} (Fig. 4.4) are between 1.95 and 2.30 mrad. For the y'_{tar} distribution only data from the central target of the quintar are used, because with a shift in y_{tar} the y'_{tar} pattern will shift, thus obscuring the pattern. The peaks have σ values between 1.10 and 1.25 mrad.

The resolutions in x'_{tar} and y'_{tar} of the HMS itself are determined by quadratically subtracting the σ of the shape of the holes from the values given above. The holes are circular, for which the σ is given by $\frac{R}{2}$, where R is the radius of the circle. The angular σ is thus 0.76 mrad for holes with a diameter of 0.508 cm at a distance of 168.0 cm from the target center. Hence, the resolution of the HMS, integrated over each row or column of holes, is 1.8 mrad in the center and 2.1 mrad at the edges for x'_{tar} , and 0.8 mrad in the center and 1.0 mrad at the edges for y'_{tar} . The degradation of the resolution for rows and columns of holes towards the edges results from the way the fitting is done. The Taylor series expands around the center of the acceptance and is weighted to where most of the events are, so that the best reconstruction is obtained there. The resolutions are summarized in Table 4.2. They are good enough for the intended L/T-separation. The influence of the resolutions on the determination of cross sections is discussed in Ch. 5.

4.4.2 Results for the SOS

The reactions and kinematic settings used for the optics data taking for the SOS were:

- *δ -scan*: Using a two-pass beam (1.797 GeV/c), the SOS detected electrons that scattered elastically off protons (4.5 cm long LH₂ target) passing the large collimator. The SOS excitation was 1.4116 GeV/c. The SOS was rotated in 10 steps from 20° ($\delta=+15.1\%$) to 46° ($\delta=-17.7\%$) relative to the beam direction.
- *y_{tar} -scan*: Using a three-pass beam (2.673 GeV/c), the quintar and the sieve slit, the SOS detected inelastically scattered electrons. The SOS was placed at an angle of 20° . Its excitation was 1.65 GeV/c.

The SOS reconstruction matrix is expanded to sixth order. The focal plane pattern of the central sieve slit hole shows that the central quintar target lies in the mid-plane of the SOS, hence no target offsets were applied in the fitting. The

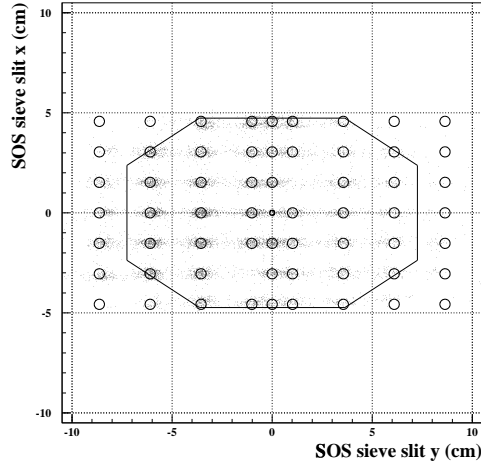


Figure 4.5: Reconstruction of the SOS sieve slit hole pattern, overlaid with the acceptance as defined by the octagonal collimator. The lack of events in the sieve slit holes in the corners is caused by limited acceptance.

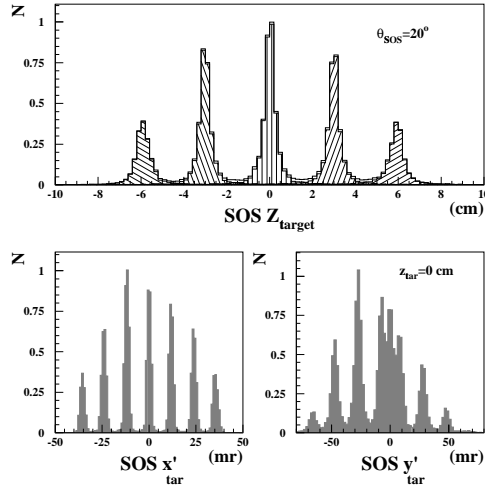


Figure 4.6: SOS quintar and sieve slit reconstruction. Top: reconstruction of the quintar z_{tar} co-ordinate. The distribution shown is the sum of the five individual targets (hashed). Bottom: reconstruction of the vertical (left) and horizontal (right) sieve slit hole pattern.

	HMS	SOS
x'_{tar} (indiv. holes)	1.8 mrad	0.3-0.5 mrad
x'_{tar} (columns)	1.8-2.1 mrad	0.3-0.8 mrad
y'_{tar} (indiv. holes)	0.3-0.7 mrad	2.4-2.7 mrad
y'_{tar} (rows)	0.8-1.0 mrad	3.1-3.3 mrad
y_{tar} (mean)	2 mm	0.9-1.1 mm

Table 4.2: Resolutions (σ) of HMS at 2.2 GeV/c and SOS at 1.65 GeV/c. The resolutions x'_{tar} and y'_{tar} are shown for individual holes and for rows and columns of holes in order to provide information about the size of systematic effects in the sieve slit reconstruction.

fitting strategy resembles that of the HMS case. Forbidden matrix elements were used to sixth order.

The center of the SOS sieve slit (see Fig. 4.5) is located at a distance of 127.8 cm from the center of the target. It has holes of 0.508 cm diameter, at regular intervals of 1.524 cm in the vertical direction and 2.540 cm in the horizontal direction. The central three rows of holes in the horizontal direction are spaced at intervals of 1.016 cm. This corresponds to steps of 11.9 mrad in x'_{tar} , and of 7.9 mrad and 19.9 mrad in y'_{tar} for the inner and outer holes, respectively. The central hole has a diameter of 0.254 cm. The orientation can be checked by means of the missing holes at +1.016 cm/+1.524 cm and -1.016 cm/-3.048 cm.

The top plot in Fig. 4.6 shows the reconstruction of the quintar target with the SOS positioned at an angle of 20° with respect to the beam. The σ values of the three innermost z_{tar} peaks are between 0.26 and 0.31 cm, which at an SOS angle of 20° means that the σ value of y_{tar} is between 0.09 and 0.11 cm.

The bottom two plots of Fig. 4.6 show the SOS x'_{tar} and y'_{tar} sieve slit patterns (the latter for the central quintar target). After quadratically subtracting the σ due to the holes (1.0 mrad), the angular resolutions (σ) for individual holes are between 0.3 and 0.5 mrad for x'_{tar} and between 2.4 and 2.7 mrad for y'_{tar} . Integrated over the rows and columns of holes, the resolutions are 0.3 and 0.8 mrad in x'_{tar} and between 3.1 and 3.3 mrad in y'_{tar} . This is due to distortions in the reconstruction of the sieve slit pattern which broaden the integrated peaks. In x'_{tar} , the distortions are small, but in y'_{tar} the deviation of the reconstructed hole position from the true value can be 1-2 mm, or 0.8-1.5 mrad. The resolutions are summarized in Table 4.2. They are good enough to allow the intended L/T-separation. The effect of distortions on the determination of cross sections is discussed in Section 5.7.

E_e (GeV)	$p_{e'}$ (GeV/c)	$\theta_{e'}$ (deg)	p_p (GeV/c)	θ_p (deg)
2.446	1.564	38.40	1.559	38.50
2.669	1.715	36.50	1.648	38.24
3.007	1.234	56.49	2.541	23.89
3.549	1.670	45.36	2.655	26.58
4.044	1.634	48.87	3.215	22.51

Table 4.3: Nominal experimental settings for the $^1\text{H}(e, e'p)$ coincidence runs. The electrons were detected in the SOS, the protons in the HMS.

4.5 Determination of experimental offsets

After the optimization of matrix elements the spectrometer quantities δ , x'_{tar} , y_{tar} and y'_{tar} should be reconstructed correctly. However, small deviations are possible due to saturation effects (see below) or to changes of the vertical electron beam position.

Physics quantities like W , Q^2 or t are calculated with the reconstructed spectrometer quantities plus the electron energy E_e and the spectrometer angles θ_{HMS} and θ_{SOS} . The electron energy is known to approximately one part in 10^3 and the spectrometer angles are surveyed, but small deviations cannot be excluded. Such deviations from assumed values are referred to as experimental offsets. They result in deviations in the physics quantities from their real values.

Most of the experimental offsets can be traced by analyzing coincident $^1\text{H}(e, e'p)$ data. This reaction is kinematically overdetermined, which allows one to inspect the following physics quantities:

- W , the invariant mass of the photon-target system. Its value should be the proton mass.
- $E_m = E_e - E_{e'} - T_p$, the missing energy, where E_e is the energy of the incoming electron, $E_{e'}$ the energy of the scattered electron and T_p the kinetic energy of the recoiling proton. Since all participating particles are detected, no energy should be missing and E_m should be zero.
- The three components p_m^{par} , p_m^{per} and p_m^{oop} of the missing momentum $\mathbf{p}_m = \mathbf{p}_e - \mathbf{p}_{e'} - \mathbf{p}_p$. They are defined as the components parallel to the momentum transfer vector $\mathbf{q} = \mathbf{p}_e - \mathbf{p}_{e'}$, perpendicular to \mathbf{q} lying in the scattering plane,

E_e	E_m	W	p_m^{par}	p_m^{per}
before <i>Heepcheck</i>				
2446	-4.5	+1.1	-4.9	+2.7
2669	-21.1	-20.1	-11.9	-10.5
3007	-5.3	+6.2	-7.1	+5.0
3549	-9.9	-11.8	-5.4	-1.7
4044	-12.6	-4.7	-10.9	+0.7
4044	-11.9	-5.9	-9.6	+0.7
after <i>Heepcheck</i>				
2448	+0.3	-0.2	+0.8	+1.3
2673	+2.1	0.0	-0.4	+2.8
3007	-1.3	-0.7	+0.9	-0.4
3544	+0.5	-0.4	+0.7	0.0
4043	+3.5	-0.3	-0.1	+0.1
4043	+2.1	+0.2	+1.0	+0.3

Table 4.4: Actual assumed electron energies and deviations in reconstructed quantities before (top) and after (bottom) applying the experimental offsets found in the *Heepcheck* analysis. Units are MeV or MeV/c.

and out of the scattering plane. The subscripts are defined as above. The mean values of all three components should be zero.

The seven experimental quantities that are checked are E_e , the momenta of the scattered electron and the recoiling proton $p_{e'}$ and p_p , their angles $\theta_{e'}$ and θ_p , and their out-of-plane angles $\phi_{e'}$ and ϕ_p . The quantities $\phi_{e'}$ and ϕ_p are related to p_m^{oop} , while the other ones are related to the four quantities W , E_m , p_m^{par} and p_m^{per} .

The dependences of the values of the physics quantities on those of the experimental ones are used in the so-called “*Heepcheck*” analysis[§] [Vol99b]. In the *Heepcheck* analysis a set of experimental offsets is found that minimizes the deviations of the values of the physics quantities from their nominal values.

A few notes on the *Heepcheck* analysis are in order:

- The experimental offsets are expected to be small. Offsets on the electron energy, spectrometer momenta and angles should not be larger than $\pm 0.2\%$ and ± 2 mrad, respectively.

[§]The name *Heepcheck* is a concatenation of the notation of the $^1\text{H}(e, e'p)$ reaction and the check of experimental offsets.

Quantity	Spectrometer	
	HMS	SOS
in-plane angle	+1.0 mrad	-0.4 mrad
out-of-plane angle	+2.4 mrad	+2.6 mrad
central momentum	-0.33%	-0.67% to +0.45% ^a
incident energy	-0.15% to +0.14%	

^aFor SOS momentum offsets see Section 4.6.

Table 4.5: *Experimental offsets found in the Heepcheck analysis.*

- The offset in a spectrometer angle is taken to be independent of the angle.
- Deviations of E_e from nominal values can be different at each new electron energy. Hence, each electron energy is corrected with a different offset. The values for these offsets are taken as a correction on the energy measurement described in Section 3.1.
- The offset in the HMS spectrometer momentum is taken as constant for all excitations. In the case of the SOS, saturation effects at high excitation cause the offset to be a function of the central momentum (see Section 4.6).

During the experiment, $^1\text{H}(e, e'p)$ runs were taken at each electron energy. The kinematic conditions of these measurements are displayed in Table 4.3. The deviations in reconstructed quantities before and after applying the experimental offsets from *Heepcheck* are shown in Tab. 4.4 along with the electron energies with and without the *Heepcheck* corrections. The deviations have decreased dramatically after applying the *Heepcheck* offsets. Especially the components of \mathbf{P}_m need to be reconstructed correctly, since t and ϕ_π depend sensitively on the reconstruction of \mathbf{P}_m . The remaining deviations are small enough to be acceptable for the further analysis of the pion electroproduction data. The experimental offsets found in the *Heepcheck* procedure are listed in Tab. 4.5. The offsets on the electron energies are smaller than 0.2%, and the offsets on the spectrometer angles are smaller than 2 mrad. The offsets on the spectrometer momenta on the other hand were found to be larger than 0.2% (for the SOS, see Sect. 4.6).

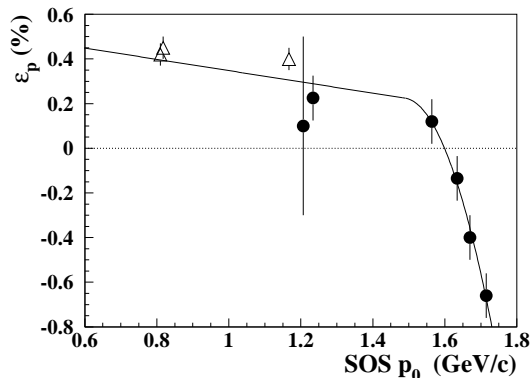


Figure 4.7: Correction to the SOS central momentum due to the decrease of the effective field length. The circles are from the present Heepcheck analysis, the triangles are from experiment E91-003. The solid line represents the used parameterization.

4.6 Saturation effects in the SOS

The SOS magnets are made of iron. Up to a certain magnetic field strength the shape of the magnetic field does not change. Beyond that point the iron starts to saturate, the field shape changes and the effective field length decreases. Although the actual field changes are not measured, the effect on the particle trajectories can be seen.

We observed two effects, which are corrected for in the reconstruction of target variables. The first effect is a decrease of the SOS central momentum $p_0 = \Gamma B$ at higher excitations, which can be explained by a decrease of the effective field length[¶]. This effect has been observed in previous experiments [Arr98, Dut99, Wes99], but has never been analyzed consistently.

The corrected p_0 can be written as $p_0^{corr} = p_0(1 + \epsilon_p)$, where ϵ_p is a function of p_0 . The present data and those from the next experiment, E91-003 [Jac91, Gas99pc], were used to obtain a parametrization of $\epsilon_p(p_0)$ (see Fig. 4.7). Above $p_0 = 1.5$ GeV/c, the function is $\epsilon_p = a + b(p_0 - 1.5)^2$, with $a = 0.002$ and $b = -0.17$. Below 1.5 GeV/c, ϵ_p depends linearly on p_0 , with $\epsilon_p(0) = 0.006$ and $\epsilon_p(1.5) = 0.002$.

The second effect is a dependence of the reconstructed δ , hence of the momentum p , on x'_{fp} (see Fig. 4.8). This effect arises from changes in the shape of the fringe fields when saturation sets in. It is corrected for on an event-by-event basis.

[¶]Note that the field measured in the center of the magnets is used to define p_0 .

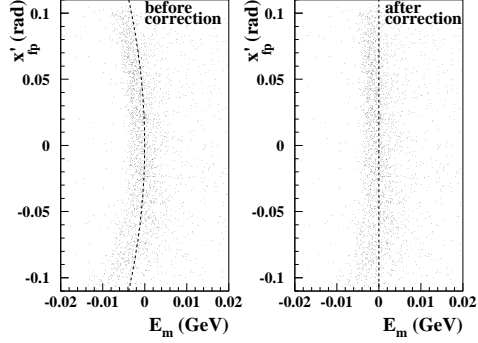


Figure 4.8: Saturation effect: x'_{fp} dependent missing energy reconstruction. Left: before, right: after correction. The SOS central momentum is 1.67 GeV/c.

The value of the reconstructed δ in the SOS is obtained by adding a central momentum dependent quadratic correction to δ :

$$\delta^{corr} = \delta + \epsilon_\delta, \quad (4.4)$$

where the correction is calculated as

$$\epsilon_\delta = (x'_{\text{fp}})^2 \left[\sum_{i=0}^3 a_i \cdot p_0^i \right], \quad (4.5)$$

with x'_{fp} is in units of rad, and with $a_0=0.47$, $a_1=-1.37$, $a_2=1.81$ and $a_3=-0.76$ for p_0 above 1 GeV/c. For $p_0 < 1$ GeV/c we have used the simple correction $\epsilon_\delta=0.15(x'_{\text{fp}})^2$. At the largest x'_{fp} (± 0.1 rad) and the largest central momentum ($p_0 = 1.715$ GeV/c), ϵ_δ is -0.004 .

Both corrections, ϵ_p and ϵ_δ , are positive at low central momentum and negative at high momenta. The reason is that the calibration of the SOS matrix elements was done at relatively high central momenta where saturation effects are non-negligible. The fact that the values of the central momentum where ϵ_p and ϵ_δ change their signs, coincide with the central momenta of the optics calibration data (δ -scan and ϵ_p at 1.4 GeV/c, y_{tar} -scan and ϵ_δ at 1.65 GeV/c), is a nice consistency check between the actual data and the calibrations.

Chapter 5

Data analysis

This chapter is devoted to the experiment and the analysis of the experimental data. It starts with the pion electroproduction kinematics (Sect. 5.1). Cross sections are obtained by comparing measured yields to those generated by a Monte-Carlo simulation program. The data analysis thus consists of two main tasks: deriving normalized yields from the measured data (Sects. 5.2–5.4), and adapting the Monte-Carlo program (Sect. 5.5) to generate yields close to the experimental data. Sect. 5.6 covers the extraction of cross sections, the L/T separation and the discussion of uncertainties.

5.1 Choice of kinematics

The choice of kinematics for the experiment is based on maximizing the range in Q^2 at high values of the invariant mass W , as well as the difference in the photon polarization ϵ between two measurements, one at low and one at high electron energy. This makes the L/T separation at each Q^2 point possible. Constraints on the kinematics were imposed by the maximum achievable electron energy, the maximum central momentum of the SOS, the minimum HMS angle and the minimum angle separation between the two spectrometers (see Ch. 3). The choice was made to keep the central value of W constant for the four Q^2 points. The kinematic restrictions dictated that W was 1.95 GeV. The nominal central kinematics are shown in Table 5.1.

The left hand plot of Fig. 5.1 shows the phase space covered in W and Q^2 for the two electron energy settings of the highest Q^2 point. The high electron energy setting provides a larger coverage in W and Q^2 by a factor of three to four in area.

Q^2 (GeV/c) ²	ϵ	E_e (GeV)	$\theta_{e'}$ ($^\circ$)	$E_{e'}$ (GeV)	θ_π ($^\circ$)	P_π (GeV/c)	$ t _{min}$ (GeV/c) ²
0.60	0.37	2.445	38.40	0.567	9.99 ^a	1.856	0.030
0.60	0.74	3.548	18.31	1.670	14.97	1.856	0.030
0.75	0.43	2.673	36.50	0.715	11.46	1.929	0.044
0.75	0.70	3.548	21.01	1.590	15.45	1.929	0.044
1.00	0.33	2.673	47.26	0.582	10.63	2.048	0.071
1.00	0.65	3.548	25.41	1.457	15.65	2.048	0.071
1.60	0.27	3.005	56.49	0.594	10.49	2.326	0.150
1.60	0.63	4.045	28.48	1.634	16.63	2.326	0.150

^aThis value of θ_π denotes the angle of the momentum transfer θ_q . The smallest achievable central HMS angle was 10.5° .

Table 5.1: Values of central kinematic settings. The quantity $|t|_{min}$ is the minimum value of $|t|$ achievable at the central values for a given kinematic setting.

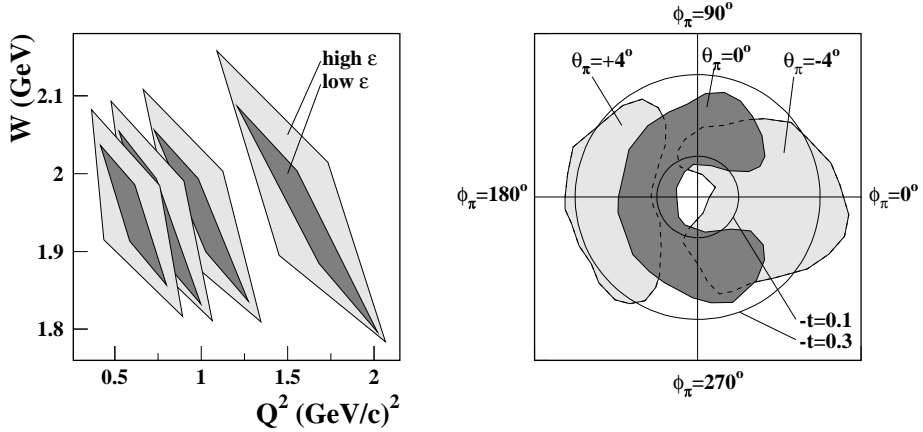


Figure 5.1: Left: Phase space in W and Q^2 at low and high ϵ (dark and light shades) for the four Q^2 kinematics. Right: Polar plot of the $|t| - \phi_\pi$ phase space ($Q^2 = 1.6$ (GeV/c)², high ϵ measurement). The Mandelstam variable $-t$ is plotted as the radial component (circles with $-t = 0.1$ and 0.3 (GeV/c)²), while ϕ_π progresses counter-clockwise ($\phi_\pi = 0^\circ$ at the right). Plotted are the distributions of the $+4^\circ$, central and -4° HMS settings.

The number of $^1\text{H}(e, e'\pi)$ events taken is at least 10,000 (40,000) at each low (high) ϵ setting, providing comparable statistics in the overlapping region. The right hand plot of Fig. 5.1 shows in a polar coordinate system the ϕ_π coverage of the high ϵ data at $Q^2 = 1.6 \text{ (GeV}/c)^2$. Even in parallel kinematics, *i.e.*, when the pion spectrometer is situated in the direction of the \mathbf{q} vector, the acceptances of the two spectrometers do not provide a uniform coverage in ϕ_π . Therefore, additional measurements were done with the HMS (pion arm) at angles of four degrees more forward and backward than the parallel kinematics value. The more forward setting was possible only at the high ϵ settings.

5.2 Upgrades to the replay engine

The standard “Hall C replay engine”, which has been extensively documented elsewhere (*e.g.*, Refs. [Arm98, Arr98]), extracts all usable information from the raw detector data and converts them into a condensed set of measured (physics) quantities. The information includes all available data per event from the detectors of the two spectrometers as well as data from the beam line equipment and data on the status of the cryotarget system.

For each event the engine collects all detector data and calculates detector responses. The tracking code identifies particle tracks and reconstructs the target vertex information from the drift chamber data (*cf.* Subsect. 4.1.2). Physics quantities like Q^2 , W or M_m are calculated from the reconstructed momenta and scattering angles at the vertex. All the physics and detector quantities that are used for further analysis are written to disk event-by-event.

In addition to including corrections for magnet saturation effects to the reconstruction of vertex variables (discussed in Sect. 4.6), the engine was upgraded in a few points:

- The part of the code where physics quantities are reconstructed was rewritten. The code now recognizes which spectrometer detects the electrons and uses the appropriate coordinate system (Ref. [Blo98]).
- Particles lose energy traversing layers of material on their way from the target to the detector hut. The calculated energy loss is added to the reconstructed particle energy at the interaction vertex (a writeup can be found in Ref. [Vol98]):
 - For hadrons, a density correction factor is added to the basic Bethe-Bloch formula (*e.g.*, Ref. [Leo87]) used in the standard engine. It accounts for

relativistic effects and introduces a correction of up to 15% to the energy loss calculation for pions.

- For electrons, the calculation of the most probable energy loss of a Landau shape distribution was replaced by a calculation based on the Bethe-Bloch equation with a relativistic correction for electrons (Ref. [Leo87]). The relative change in the calculated values of the energy loss amounts to 20-80%, depending on electron momentum, material and layer thickness.

The change in the calculation of energy loss is between 0.5 and 3 MeV. This is comparable to the accuracy needed in the determination of experimental offsets (see Sect. 4.5). Therefore these changes constitute a significant improvement and are now part of the standard replay engine.

5.3 Identification of good events

The identification of true ${}^1\text{H}(e, e'\pi^+)$ events depends on the correct identification of electrons and pions in the two spectrometers (Subsect. 5.3.1) and on precise coincidence timing information for the separation of true and random coincidence events (Subsect. 5.3.2).

5.3.1 Particle identification

In the SOS negatively charged pions are detected along with the electrons. The contamination of pions that were not rejected by the electron trigger and that possess the correct coincidence timing (see above) and reconstructed missing mass was 2.7% in the worst case. The Čerenkov detector and the lead-glass calorimeter are used in suppressing those pions. The selection criteria (“cuts”) used for electron identification were more than 0.5 photo electrons in the Čerenkov detector and a “*shower sum*” of more than 0.6. The “*shower sum*” is the amount of energy deposited in the calorimeter normalized to the momentum. The loss of electrons that fail these cuts is smaller than 0.1%, whereas the suppression of pions is better than 99%. In all cases the pion contamination is thus smaller than 0.03%.

In the HMS, where pions are desired, the contaminating particles are protons and positrons. The rejection of positrons is done via the signal from the Čerenkov detector. Positrons that were not rejected by the HMS pion trigger contribute up to 2.2% of all events with the desired coincidence timing and reconstructed missing mass. The limit of 0.2 photo-electrons in the Čerenkov detector provides positron rejection to better than 99.4%. The remaining positron contamination

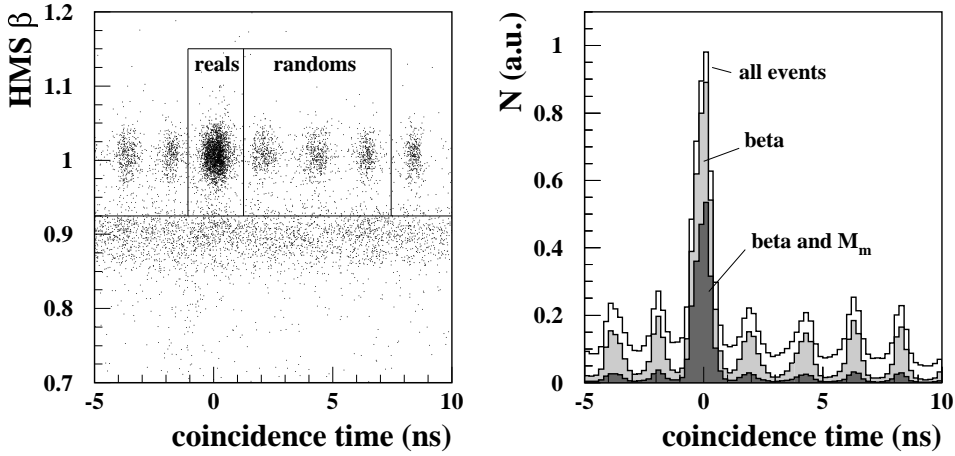


Figure 5.2: Left: HMS β versus coincidence timing. The bounded area on the left contains the real electron-pion coincidences, those in the area on the right are used for random background subtraction. The protons below $\beta = 0.925$ (continuous in time) are rejected. Right: coincidence timing spectrum (reals at 0 ns). Both the HMS β cut and the cut on the reconstructed missing mass mainly reduce the contribution of random events.

is thus always smaller than 0.02%. The contamination of random electron-proton coincidence events with the coincidence timing of the real electron-pion events that have missing mass values in the accepted region is 2.9% in the worst case. The rejection of such random coincidences is discussed in Subsection 5.3.2. Proton rejection is facilitated by means of the relative particle speed β , calculated from the time-of-flight difference between the two hodoscopes. The β distributions for pions and protons of similar momentum overlap, especially for the high Q^2 points, where the pion and proton momenta are high. With the chosen limit of $\beta = 0.925$ the loss of pions is negligible. This is shown in the left hand plot of Fig. 5.2. In this plot, the protons appear as a band because the calculation of the coincidence timing is optimized for particles with $\beta = 1$. The proton contamination is reduced by 50-80%, depending on the kinematics. Since the coincidence timing of the real electron-proton events differs significantly (between 3 and 8 ns) from that of the real electron-pion coincidences, all remaining protons are treated as random background (see Subsect. 5.3.2).

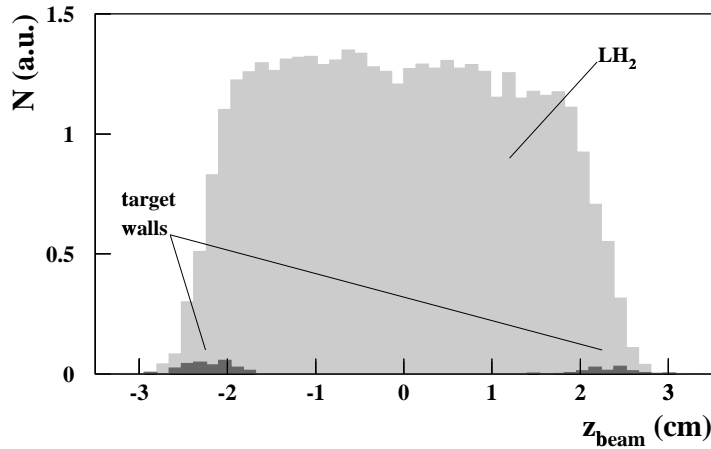


Figure 5.3: Vertex position (calculated from $SOS y_{tar}$) for events from the liquid hydrogen target (light shade). The dark shaded distribution contain properly weighted events from the dummy target (about 1% of all events).

5.3.2 Subtraction of backgrounds

The experimental data contain two types of non-physics background: random coincidences stemming from unrelated electrons, pions and protons, and coincident electrons and pions originating from the aluminium walls of the target cell. Random coincidences occur between events from any two beam bursts within the coincidence timing gate. The resulting coincidence timing structure of random coincidences is peaked every 2 ns. The random events under the real coincidence peak cannot be identified. These random contributions are estimated by selecting a number of random peaks and subtracting their properly weighted contribution from the data in the real coincidences peak (see Fig. 5.2). We chose three random bursts which had full coincidence trigger efficiency and where no real protons were leaking in (the left hand region of Figure 5.2). The random background to the real coincidences is between 2 and 5%, depending on the kinematic conditions.

Contributions from the target walls are estimated by taking data with the dummy target (*cf.* Subsect.3.2.2) and subtracting them from the data taken with the LH_2 target. The dummy yield is weighted with a factor of 0.071 (0.104) for the front (exit) windows to account for the ratios of the thicknesses of the cell walls and the dummy target. Fig. 5.3 shows the contribution of events from the cell walls.

5.4 Efficiencies, dead times and other correction factors

The experimental yields Y_{exp} that are used to calculate cross sections are obtained for each measurement (“run”) by the relation

$$Y_{\text{exp}} = \frac{N}{\epsilon_{\text{tot}} Q_{\text{tot}}}, \quad (5.1)$$

where N is the number of events in a run, ϵ_{tot} is a total efficiency factor and Q_{tot} is the accumulated charge. In the case of multiple runs for one kinematic setting, the weighted mean of the yield is taken with Q_{tot} per run as weight. In the following, the calculation of the inefficiencies and dead times that contribute to ϵ_{tot} and the calculation of Q_{tot} are described.

5.4.1 Tracking efficiencies

The tracking efficiency is defined as the probability that a particle that is identified as an electron or pion is associated with a valid track from the wire chambers. Note that this depends on both the efficiency of the wire chambers and on the tracking algorithm.

In the HMS a particle is considered valid if it is identified as a pion (though the cuts are set more loosely than those described in Subsect. 5.3.1). Also, there must be a signal in at least three of the four hodoscope planes, and it must be detected inside a coincidence time window of 140 ns with a particle in the SOS. Similar constraints mark a valid event in the SOS, although the particle has to be identified loosely as an electron (high Čerenkov signal) instead of as a pion.

The failure of the tracking algorithm to find a valid track can be caused by a wire chamber inefficiency, or a failure of the tracking algorithm itself. Inefficient wire chamber planes can cause the algorithm to fail by offering it too little information for a fit. Noisy wires can mimic a high number of multiple hits, which the tracking algorithm is unable to handle. In order to keep the computing time needed for the tracking algorithm within reasonable limits, while keeping sufficiently high tracking efficiencies, a maximum number of hits per wire chamber of 25 was used.

While processing the raw data, the replay engine keeps count of the number of events with and without a track. Fig. 5.4 shows the thus obtained tracking efficiencies in HMS and SOS per run as a function of the event rate on the scintillator detectors. The HMS tracking efficiency is generally above 0.98 and shows a weak dependence on the scintillator event rate. The SOS tracking efficiency, however, is

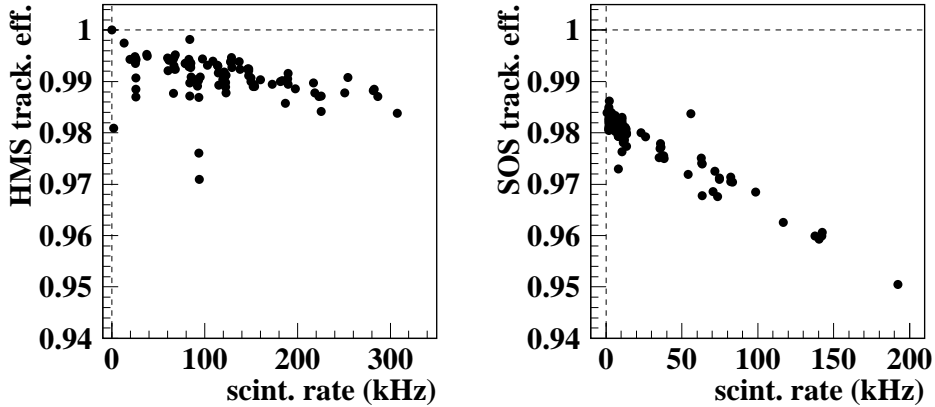


Figure 5.4: *Tracking efficiencies for HMS and SOS, plotted against the count rate on the first layer of scintillator detectors.*

slightly worse, but still generally above 0.96. The reason for its being worse can be sought in the fact that for the SOS there had to be a signal in 5 out of the 6 wire planes per chamber, while for the HMS it was sufficient if there were signals from 4 of the 6 wire planes.

Another kind of tracking efficiency is the beta tracking efficiency. Reconstructed tracks are projected to the hodoscopes. The signals from the hodoscope panels that lie in the path of the trajectory are taken, and their time difference is used to calculate the particle speed $\beta = v/c$. In the case of multiple hits of adjacent panels, a fitting algorithm has to decide what combination of hits from the different hodoscope layers has the highest likelihood of being the correct one. If the algorithm picks a combination of hits stemming from different particles, the resulting speed information is wrong, and because of that the event is rejected. Because the particle speed information is used only in the HMS to separate pions from protons, only the beta tracking efficiency of the HMS is important. A systematic study showed that the dependence of the beta tracking efficiency on the event rate is relatively weak (Ref. [Mac99pc]). A common correction factor of 0.9825 ± 0.0025 for the beta tracking efficiency has been used during the analysis (see also Table 5.2).

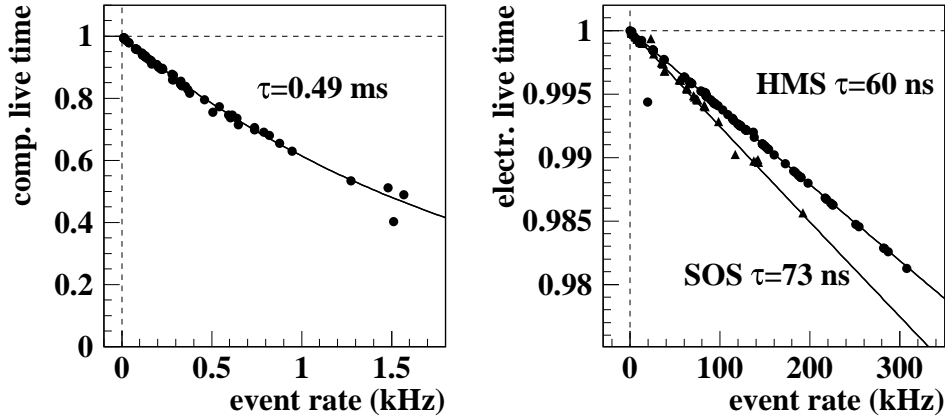


Figure 5.5: Left: computer live time versus the rate of events offered to the Trigger Supervisor. The fit corresponds to a time constant $\tau \approx 0.49 \text{ ms}$. Right: electronic live time for the HMS (bullets) and SOS (triangles), with time constants of 60 ns and 73 ns.

5.4.2 Computer and electronics dead times

Dead times result from the rejection of valid events when either the trigger electronics are still processing the previous event and are unable to accept the new one (electronic dead time), or because the Trigger Supervisor is still processing the signals from the previous event and writing it to disk (computer dead time). The live time is defined as the complement to unity of the dead time.

The probability of n events occurring in an interval τ for a certain event rate r is given by the Poisson distribution

$$P(n) = \frac{(r\tau)^n e^{-r\tau}}{n!}. \quad (5.2)$$

The live time, or the probability of zero events occurring in the interval t is thus $P(0) = e^{-r\tau}$. For small rt this can be approximated by $P(0) = 1 - r\tau$.

The left hand plot of Fig. 5.5 shows the computer live time against the rate at which events are presented to the Trigger Supervisor. The computer live time is calculated per run as the ratio of the number of triggers over the number of pretriggers. The curve represents a fit with a time constant $\tau \approx 0.49 \text{ ms}$. This is about the time it takes the Trigger Supervisor to read out the electronics crates and the data acquisition computer to write an event to disk. The run-by-run computer live time scatters because other factors, such as the network traffic or the ratio of

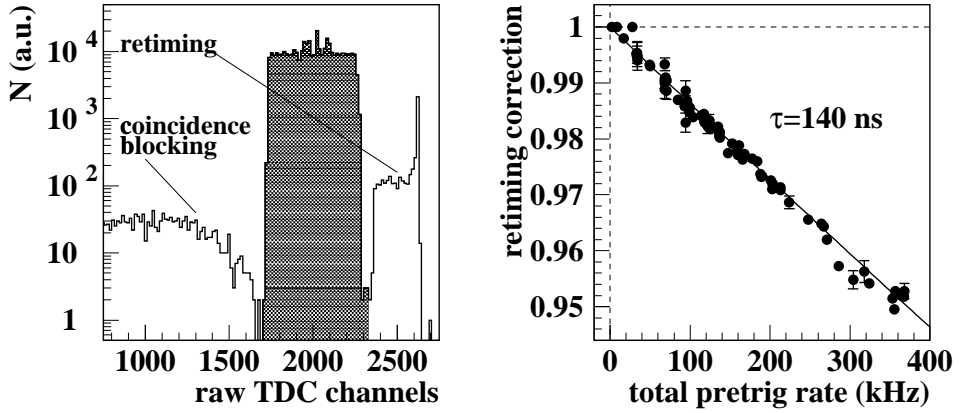


Figure 5.6: *Left: logarithmic plot of a typical HMS coincidence time raw TDC spectrum. The shaded area corresponds to the 140 ns coincidence window and contains the events with the correct timing information. The other events suffered from coincidence blocking (left) or retiming (right). Right: total coincidence blocking and retiming correction as a function of the sum of the HMS and SOS pretrigger rates.*

singles events to coincidence events (which take longer to read out) have influence on the computer live time. This jitter, however, does not contribute to the systematic uncertainty, since the fit is not used in the calculation of yields. The data acquisition system was used in an unbuffered mode because of potentially serious problems with loss of synchronization. This made the computer dead time relatively large. The event rate was commonly chosen such that computer dead time was below 40%. The right hand plot shows the electronic live time of HMS and SOS plotted against the rate of pretrigger events. In the case of the HMS the slope is determined by the 60 ns input gates of the logic modules that combine the scintillator signals into logic signals. The 30 ns Čerenkov veto gate makes a negligible contribution of up to 0.02%. In the case of the SOS logic module input gates are 73 ns long. The electronic dead time in HMS and SOS is always below 2%.

5.4.3 Coincidence blocking and retiming correction

The coincidence timing plays a crucial role in separating random background events from good ones. It is determined by a clock that starts counting when an HMS signal arrives and is stopped when the next SOS signal arrives. Two effects can cause

the coincidence timing for good events to fail. In the first case, a random SOS single arriving before the coincident particle can stop the clock too early, effectively blocking the coincidence. A cut on the coincidence time will largely remove these events. The second effect is that a late SOS trigger can confuse the timing logic in such a way that the coincidence timing clock, which is usually started by the HMS and stopped by the SOS, is started and stopped by the SOS (“retiming”). Fig. 5.6 shows a typical TDC spectrum for the coincidence timing, with good events in the shaded area. Wrongly timed events appear at lower (coincidence blocking) and higher (retiming) TDC channel numbers. The right hand plot shows the total correction, calculated as the ratio of the number of events in the shaded area to all events, as a function of the sum of the pretrigger rates of the HMS and SOS. The time constant t corresponds to a coincidence time window of 140 ns. The correction is between 0% and 5%. A detailed discussion of this effect can be found in Ref. [Moh99].

5.4.4 Pion absorption

A certain percentage of the pions coming from the target are lost because they undergo nuclear interactions with nuclei in the various layers of material they have to pass before reaching the detectors of the HMS. The absorption of pions was not measured directly. Instead the absorption of protons from the elastic ${}^1\text{H}(e, e'p)$ reaction was measured and used for the pions under the assumption that the total absorption cross section for pions on nuclei is about equal to that for protons. This assumption is justified by the difference of less than 15% in the πd and pd absorption cross section (Ref. [Cas98]).

For the measurement of proton absorption, data were taken for elastic electron scattering off protons. The ${}^1\text{H}(e, e')$ and the ${}^1\text{H}(e, e'p)$ reactions were measured simultaneously. From the kinematics of the singles electrons the kinematics of the corresponding protons was calculated. If such a proton was inside the acceptance of the HMS and not detected, it was counted as absorbed. The ratio of the number of absorbed protons to the number of tagged protons inside the HMS acceptance is the proton absorption factor.

The proton absorption amounted to between 2.8% and 5.5%, depending on the proton momentum. To account for pion absorption, a correction of $4 \pm 1\%$ was used. The uncertainty is chosen to be 1% because the momentum range of the pions (between 1.7 and 2.4 GeV/ c , see Table 5.1) is much smaller than that of the protons in the study of the elastic ${}^1\text{H}(e, e'p)$ reaction (between 1.5 and 3.2 GeV/ c , see Table 4.3).

5.4.5 Target density correction

The electron beam deposits energy along its path through the liquid hydrogen target. Because of the small dimensions of the beam this causes local boiling and a reduction of the density of the target liquid. The amount of energy deposited in the target liquid is proportional to the electron current and almost independent of the electron energy in the range between 2.4 and 4.0 GeV. The effect of boiling is reduced by depositing the energy in a larger volume. To that end the beam was rastered in a rectangular pattern (Sect. 3.1).

In order to measure the reduction of target thickness from this effect, data were taken for the $^1\text{H}(e, e')$ elastic scattering reaction, at an electron energy of 4.0 GeV. The scattered electrons were detected in the HMS at a scattering angle of 12.5° . The measurement was done for electron beam currents between 10 and $80\ \mu\text{A}$. The analysis was based on the pretrigger rates, corrected for dead times. For the LH_2 target and a fast raster amplitude of $\pm 1\ \text{mm}$, a reduction of pretrigger counts of $5.6\%/100\mu\text{A}$ was found. An analysis of the same data based on reconstructed physics variables and corrected for tracking efficiencies and dead times resulted in a yield reduction of $6.2\%/100\mu\text{A}$. Therefore, a value for the correction of $6\pm 1\%/100\mu\text{A}$ has been assumed (Ref. [Mac99pc]).

5.4.6 Charge measurement

The electron beam current and accumulated charge per run were measured with the beam current monitors located on the beam line in front of the target. These were frequently calibrated against the Unser monitor, which could be calibrated absolutely with known currents in a wire. The Unser monitor could not be used for normal operation because of its poor signal-to-noise ratio and offset drift. During beam current monitor calibration beam was sent to Hall C in a series of increasing and decreasing beam currents, interrupted by periods of no beam. The beam-off periods served to determine the zero-offset of the Unser monitor. The gain of the BCMS were then calibrated against the well-known gain of the Unser monitor (Ref. [Arm98]).

The total charge is obtained by integrating the current. However, when the beam goes off, integrating a small nonphysical current due to electronic offsets is avoided by stopping the integration when the beam current was lower than $1\ \mu\text{A}$. The random error attributed to the accumulated charge is 0.5% (Ref. [Mac99pc]).

5.5 SIMC

5.5.1 Overview of SIMC

The Hall C Monte Carlo package SIMC, which was used for the analysis of several previous experiments, has been described in detail elsewhere (*e.g.*, Refs. [Arr98]). Therefore an overview of the program should suffice.

The SIMC code simulates real events. The code generates homogeneously the position z_{tar} of the interaction in the target (the “vertex”), the electron and pion (or proton) direction in the laboratory frame and the electron momentum (the momentum of the hadron is then determined by energy and momentum conservation). The outgoing particles are followed through the target, the target foils, and the air between the target chamber and the spectrometer entrance foil. Energy losses and multiple scattering are calculated for the passage of the particles through matter. The particles are followed through the collimators and the spectrometer magnets to the wire chambers and other detectors. COSY generated matrix elements* are used for both spectrometers to trace the particles through the magnetic fields and apertures inside the spectrometers. In this way the acceptances of the spectrometers are simulated (see Subsec. 5.5.3). The reconstruction of target quantities is done as described in Ch. 4, with realistic wire chamber resolutions and matrix elements that are consistent with those used to trace the particles through the spectrometers†. The code also takes into account radiative processes and pion decay (see below). Multiple scattering, wire chamber resolutions and radiative processes cause the reconstructed quantities to differ from the original vertex quantities.

Each event is weighted with a luminosity factor and a cross section. For events that fall inside the detector acceptances, all physical variables needed for further analysis are calculated and written to a file. The reconstructed quantities are used in the comparison of the simulated and experimental distributions in various variables (for instance focal plane variables, Q^2 or W , see Fig. 5.7). The comparisons are done for one- and two-dimensional distributions. The boundaries are simply chosen within the phase space in both the simulated and experimental data. This is discussed in Subsec. 5.5.3). When the boundaries are well described, differences in magnitude between the simulated and the experimental distributions indicate that the real cross section differs from the one used in the model. In Subsec. 5.5.4 it is

*The COSY model consists of sets of “forward matrix elements”, which model the magnetic field in steps from one aperture to the next.

†The reconstruction matrix elements are inverted from the forward matrix elements. The inversion is truncated at sixth order.

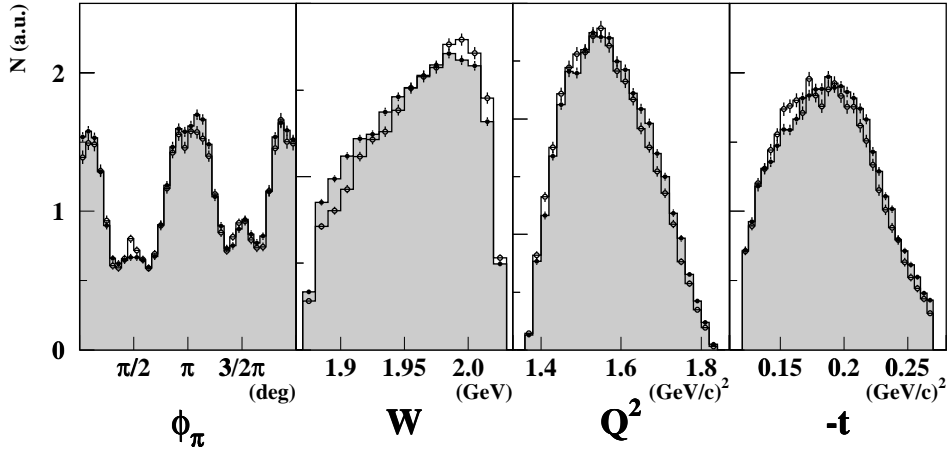


Figure 5.7: Comparison of the distributions of experimental data (empty area, circles) and SIMC generated distributions (shaded area, crosses) in ϕ_π , W , Q^2 and $-t$ for $Q^2 = 1.6 \text{ (GeV/c)}^2$, high ϵ settings. The error bars are statistical only. The dependence of the cross section was fitted in t , Q^2 and ϕ_π , but not in W . Due to the correlation of W with Q^2 and t , the linear discrepancy of the distributions in W is reflected in the other two variables.

discussed how the model cross section is derived and how it is used to extract cross sections from the experimental data.

Radiative processes

The program simulates external radiative processes by letting a fraction of the generated electrons and pions or protons radiate a photon in the direction of motion. Internal radiative processes (including the vertex correction factor) for electrons and protons are included following the method described in Refs. [Mak94, Mak98]. As shown in Fig. 5.9, the simulation of the radiative tail works well for the $^1\text{H}(e, e'p)$ process. In order to provide an approximate description of the radiation of the much lighter pion, the code for proton radiation is used, with the proton mass changed into the pion mass. Obviously, the weighting of the event in which a photon was radiated is done with the model cross section for pion electroproduction instead of for proton knockout. The effect of pion radiation on the cross section was studied by extracting cross sections with and without pion radiation in SIMC and comparing

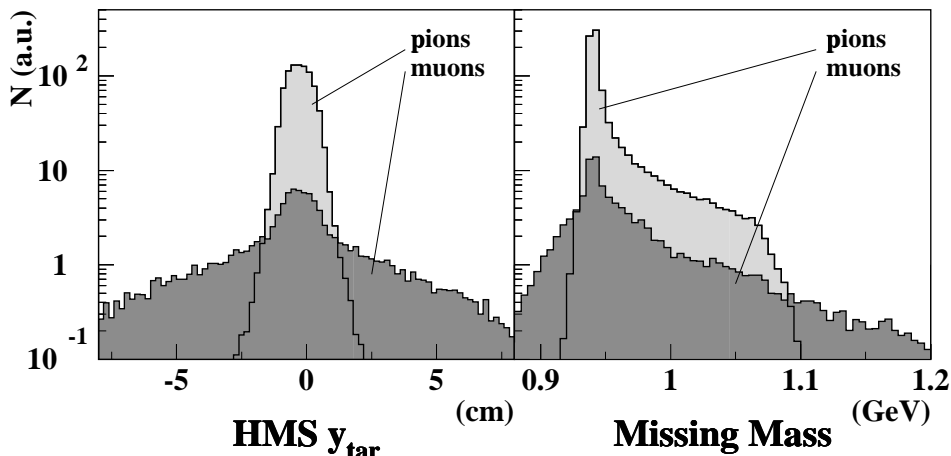


Figure 5.8: Reconstructed pion and muon distributions (light and dark shades, respectively) from SIMC. Left: HMS y_{tar} distribution, right: missing mass distribution. The pion distribution drops steeply above 1.07 GeV (the energy of the radiated photons is limited to 200 MeV in the simulation).

the results. The difference is less than 3% over the accepted phase space. The uncertainty due to the use of the simple model for pion radiation is taken to be 1%, and 0.5% for the electron radiation. Since the pion kinematics are the same for the low and high ϵ measurements, the uncertainty from pion radiation is correlated in ϵ , whereas the uncertainty from electron radiation is uncorrelated in ϵ .

Pion decay

The possibility that pions decay into muons and muon neutrinos is included in the simulation. In SIMC the pion can decay at any point along its path in field free regions and at fixed points in the magnetic fields of the HMS. The muon momentum is calculated in the pion center-of-mass frame, where the angular distribution is uniform and the muon momentum is fixed. The muon is then followed through the spectrometer to the detector hut. Like in the experimental data, the muon is treated as if it were a pion in the reconstruction of target variables. In both the experimental and simulated data the muons constitute a background that is not removed by means of particle identification. However, in Fig. 5.8 it is shown that the distribution of the muons in various reconstructed quantities is much broader

than that of the pions. While roughly 20% of all pions decay on their way to the HMS detector hut, only a quarter of the muons fall within the acceptance and pass all cuts. The muon contamination after applying all cuts is thus only 5-6%. The uncertainty associated with pion decay in field free regions (continuous decay) is negligible, since the decay length of the pion is known very well and the branching ratio for this reaction channel is very close to unity. The error made by allowing the pion to decay only at fixed positions inside the magnetic field is small, too. A muon from a pion decay that occurred early on its path to the detectors is more likely to fail cuts on reconstructed quantities than one from a decay close to the detectors. More than 85% of all simulated muons that survive all cuts originate in the field free region behind the HMS dipole. An estimated uncertainty of 1% due to pion decay can therefore be considered safe.

5.5.2 $^1\text{H}(e, e'p)$ in SIMC

In addition to providing information on experimental offsets (see Sect. 4.5), the elastic $^1\text{H}(e, e'p)$ reaction also serves to check the accuracy of the phase space model in SIMC, and it can be used to study the accuracy of the calculated yields. The model cross section used was (see Ref. [Hal84])

$$\frac{d^2\sigma}{d\Omega_{e'}} = \frac{\alpha^2}{4E^2} \frac{\cos^2 \frac{\theta_{e'}}{2}}{\sin^4 \frac{\theta_{e'}}{2}} \frac{E'}{E} \left(\frac{G_E^p{}^2 + \tau G_M^p{}^2}{1 + \tau} + 2\tau G_M^p{}^2 \tan^2 \frac{\theta_{e'}}{2} \right), \quad (5.3)$$

where E is the incoming electron energy and E' and $\theta_{e'}$ are the energy and scattering angle of the outgoing electron, α is the fine structure constant, and $\tau = Q^2/4M_p^2$. For G_E^p and G_M^p , fits to the world data (given in Ref. [Bos95]) were used.

Data for the elastic $^1\text{H}(e, e'p)$ reaction were taken in five different kinematic settings (see Table 4.3). Those kinematic conditions were modelled in SIMC. The experimental and simulated missing energy distributions for one of the settings are shown in the left hand plot of Figure 5.9. The simulated radiative tail is in good agreement with the experimental data. Experimental data for negative values of E_m result mainly from resolution effects, but also from target wall events and from protons that scattered in the HMS collimator. The simulated distributions are in good agreement with the experimental data in all cases except for the kinematic setting in which the SOS is set at an angle of 56° . It was found that the model for the SOS in SIMC lacks acceptance for events coming from $y_{tar} > 1.5$ cm (see below). This region of the phase space was removed from further analysis.

After this the total simulated yields and the data were compared. The right hand plot in Fig. 5.9 shows the ratios of the experimental yields to the simulated

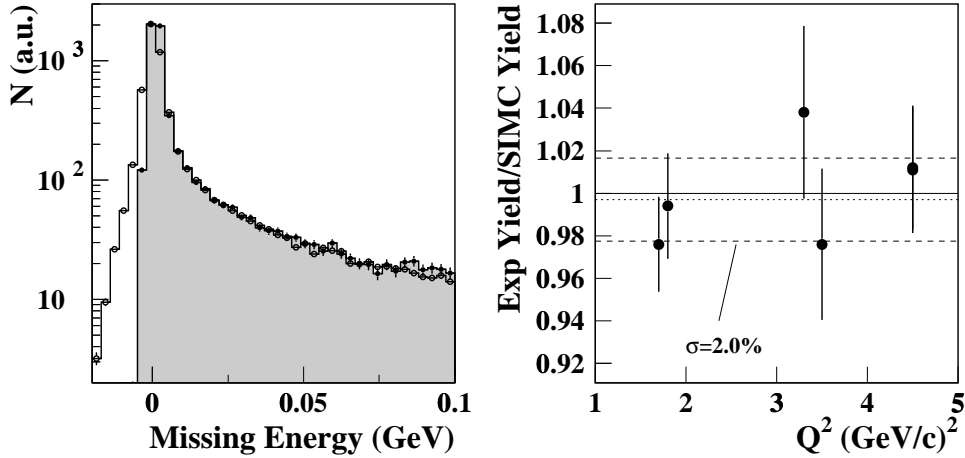


Figure 5.9: Left: logarithmic plot of the E_m distribution for one of the $^1\text{H}(e, e'p)$ kinematics. The SIMC distribution (shaded area, crosses) is overlaid by the experimental data (circles). Right: ratios of the yields from data and SIMC for the five different kinematics (two measurements were done at $Q^2 = 4.5$ (GeV/c) 2 before and after a week-long accelerator shutdown). The error bars include statistical uncertainties and systematic uncertainties of the order of 2%.

ones. Over the whole Q^2 range between 1.5 and 4.5 (GeV/c) 2 the ratios scatter around unity with $\sigma=2.0\%$, which can be explained by the uncertainty of the individual points. In addition there is the uncertainty of the world's data, which is of comparable magnitude. The result verifies that the efficiencies and dead times used to calculate the experimental yields are well understood and that the Monte Carlo program simulates the experimental conditions and acceptances very well.

5.5.3 Detector acceptances in SIMC

In the elastic $^1\text{H}(e, e'p)$ reaction the outgoing electron and proton are strongly correlated, so that only a subset of the phase space is populated. The full SOS acceptance was studied by measuring deep inelastic electron scattering on deuterium. A detailed comparison of the boundaries of the acceptance of the experimental and the simulated data was done in the four target variables δ , y_{tar} , x'_{tar} , and y'_{tar} (see Subsect. 4.1.1). Small parts of the phase space, where the boundaries of simulation

and experimental data disagree were excluded from the analysis. The following shortcomings of the acceptance model for the SOS were discovered:

- the SOS model has too little acceptance for events coming at SOS $y_{\text{tar}} > 1.5$ cm (see Subsect. 5.5.2). With the 4.5 cm target cells this effect can be seen when the SOS is placed at angles of 42° or larger.
- the boundaries of the $(\delta, y_{\text{tar}}, y'_{\text{tar}})$ phase space from the SOS model disagree with the experimental acceptance in some points. The cuts that exclude this discrepancy are defined as follows (y'_{tar} in mrad, y_{tar} in cm, δ in %):
 $y'_{\text{tar}} > -125.0 + 4.25 \delta + 64.0 y_{\text{tar}} - 1.7 \delta y_{\text{tar}}$, and
 $y'_{\text{tar}} < 125.0 - 4.25 \delta + 64.0 y_{\text{tar}} - 1.7 \delta y_{\text{tar}}$.

These parts of the acceptance were omitted from the analysis.

The HMS model acceptance does not present a comparable challenge. As the HMS is placed at very forward angles in all kinematics, the y_{tar} acceptance is flat in the (limited) region of interest. The x'_{tar} acceptance is limited to ± 60 mrad (*cf.* Subsect. 4.4.1). The acceptances in y'_{tar} and δ are also within previously determined safe limits (Ref. [Ent99pc]). The limits used in the analysis are listed in Subsects. 4.4.1 and 4.4.2. The phase space for coincident HMS and SOS events is checked with data from the pion electroproduction reaction by comparing distributions for reconstructed quantities such as HMS and SOS target variables, W , Q^2 , t , and missing energy and momenta. For the extraction of separated cross sections for the high ϵ kinematics, the analysis was restricted to the range in W and Q^2 that is covered by the acceptance of the low ϵ kinematics (see Fig. 5.1). Because of the distortions in the reconstruction of angles in the SOS of up to 1.5 mrad and to a lesser extent in the HMS (see Subsects. 4.4.1 and 4.4.2), the uncertainty in the extraction of cross sections related to the detection volume is estimated to be 2%.

5.5.4 The model cross section for pion electroproduction

Definitions

The simulation code contains a model for the cross section for the pion electroproduction in the five-fold differential form of Eq. (2.7):

$$\frac{d^5\sigma}{dE' d\Omega_{e'} d\Omega_\pi^*} = \Gamma_V \frac{d^2\sigma}{d\Omega_\pi^*}, \quad (5.4)$$

where the asterisks denote quantities in the center-of-mass frame of the pion-nucleon system, Γ_V is the virtual photon flux factor of Eq. (2.8) and ϵ is the virtual photon

polarization introduced in Eq. (2.9). The two-fold differential cross section can be written in terms of an invariant cross section $d^2\sigma/(dtd\phi)$ as (with $\phi^* = \phi$)

$$\frac{d^2\sigma}{d\Omega_\pi^*} = \frac{d^2\sigma}{dtd\phi} \cdot \frac{dt}{d\cos\theta^*}, \quad (5.5)$$

where $dt/d\cos\theta^* = |\mathbf{p}_\pi^*||\mathbf{q}^*|/\pi$ is the Jacobian factor, and \mathbf{p}_π^* and \mathbf{q}^* are the three-momenta in the center-of-mass frame of the pion and the photon, respectively. The form $d^2\sigma/(dtd\phi)$ is the form used in Ref. [Bra77] and in various theoretical publications. As shown in Eq. (2.10), this cross section can be written as a sum of four cross sections that depend on W , Q^2 and t ,

$$2\pi \frac{d^2\sigma}{dtd\phi} = \epsilon \frac{d\sigma_L}{dt} + \frac{d\sigma_T}{dt} + \sqrt{2\epsilon(\epsilon+1)} \frac{d\sigma_{LT}}{dt} \cos\phi + \epsilon \frac{d\sigma_{TT}}{dt} \cos 2\phi. \quad (5.6)$$

Determination of the model cross section

For the purpose of extracting cross sections, the data are binned in t , but integrated over W , Q^2 and θ^* . This integration is complicated because of the range covered in these quantities (see for instance Fig. 5.1) and the correlations between them. To make matters more complicated, only three of the four quantities W , Q^2 , t and θ^* are independent. If the dependence of the cross section on these variables is poorly understood, problems will arise in determining the (average) cross section and also in the L/T separation. The problems are that the cross section has to be averaged over the phase space of the t bin, and that in order to do the L/T separation, the same values for W , Q^2 and t have to be used in the high and low ϵ data. If the average values of these quantities in a given t bin differ for both data sets, the cross sections must be scaled towards common values of W and Q^2 . When using an imperfect model, the scaling error will influence the high and low ϵ data differently and thus influence the extraction of σ_L and σ_T . Also, the interference terms have to be modelled well, because the ϕ acceptance is not homogeneous (see right hand plot in Fig. 5.1 and leftmost plot in Fig. 5.7).

Both problems are alleviated by creating a model such that the ratio of experimental to simulated yields does not depend (or hardly depends) on W , Q^2 , t , θ^* and ϕ . If the model meets this criterium, it is safe to use

$$\left(\frac{d\sigma}{dt}\right)_{\text{exp}} = \frac{Y_{\text{exp}}}{Y_{\text{sim}}} \left(\frac{d\sigma}{dt}\right)_{\text{MC}} \quad (5.7)$$

for the extraction of unseparated experimental cross sections at any value of W , Q^2 and t . In this way, common values of W and Q^2 can be chosen freely for the high and low ϵ bins in order to make an L/T separation possible. The iterative fitting procedure used to create the model for the cross section is described below.

Fitting of the interference terms

First the interference terms σ_{LT} and σ_{TT} are determined. The experimental and simulated yields are binned in t , θ^* and ϕ . For each bin in t the ratio $R(\theta^*, \phi) = Y_{\text{exp}}/Y_{\text{MC}}$ is calculated for each (θ^*, ϕ) bin. The two-dimensional distributions are fitted with the fit function $f(\theta^*, \phi) = a + b \sin^2 \theta^* + c \sin \theta^* \cos \phi + d \sin^2 \theta^* \cos 2\phi$. The latter two terms in the fit function correspond to the two interference terms σ_{LT} and σ_{TT} , taking into account their leading order behaviour in θ^* (Ref. [Mul90]). The first term corresponds to the part of the longitudinal and transverse cross sections independent of θ^* . The data indicate that the (transverse) cross section has a $\sin^2 \theta^*$ dependent component (see also Ref. [Mul90]), the b term of the fit function. High ϵ data are used for the fit because of their larger coverage in ϕ . Data from the central portion of the coverage in W and Q^2 are used in order to minimize correlations in these variables. The fitting process starts with a reasonable estimate for the four cross sections, and the result from the fit to the ratios is used to correct the interference terms and the $\sin^2 \theta^*$ dependent σ_T term in the model cross section. The resulting new cross section model is used for another iteration. When the fit converges, the terms b , c and d are consistent with zero, while a is close to unity.

In the beginning the fit for the interference terms is done for each Q^2 point separately. By doing the fit for all t bins the t dependence of the interference terms per Q^2 point is determined. When this converges for the four Q^2 points, the Q^2 dependence of the interference terms is parametrized.

Determination of the longitudinal and transverse terms

The determination of the longitudinal and transverse cross sections is done in parallel with the fitting of the interference terms. After each iteration for the θ^* dependent terms, σ_L and σ_T are extracted and parametrized as functions of t . After this procedure has converged for each Q^2 point, the Q^2 dependence of the model for σ_L and σ_T is parametrized.

Cross section model

The procedure results in the following model for the cross sections, which is valid in the range of Q^2 between 0.4 and 1.8 (GeV/c)²:

$$\frac{d\sigma_L}{dt} = 34.0 e^{(-23.5+6.0Q^2)(-t-0.02)} \quad (5.8)$$

$$\frac{d\sigma_T}{dt} = \frac{10.0}{Q^2 + Q^4} (1.0 - 4.0t) - 4.0 \frac{d\sigma_L}{dt} \sin^2 \theta^* \quad (5.9)$$

$$\frac{d\sigma_{LT}}{dt} = \left(0.94 - 34.4 e^{-2.76Q^2} + 171.0 e^{113.9t} e^{-0.75Q^2} \right) \sin \theta^* \quad (5.10)$$

$$\frac{d\sigma_{TT}}{dt} = \frac{2.22}{Q^4} \frac{t}{(t - 0.02)^2} \sin^2 \theta^*. \quad (5.11)$$

These cross sections have the units $\mu\text{b}/\text{GeV}^2$. The model is a mixture of purely phenomenological fits and fits with a theoretical basis (such as the pion pole term in σ_{TT}).

Of the dependences on W , Q^2 , t and θ^* , only that on W has not been fitted, because the data spanned a limited range in W . Instead, a W dependence of the cross section of the form $(W^2 - M_p^2)^{-2}$ is included in the model. This dependence, which is the one for the t -pole term[‡], was also used in the analyses of the experimental data from Refs. [Bra77, Beb78]. The left hand plot in Figure 5.7 shows that this W dependence may not be entirely correct. However, since the discrepancy is linear in W and relatively small (over the most part of the phase space the discrepancy is smaller than 10%), it is still safe to average over W .

5.6 L/T separation

After the cross section model is tuned to the data, the data are binned in t (*i.e.*, integrated over W , Q^2 and ϕ). Unseparated cross sections $\sigma_u = \epsilon\sigma_L + \sigma_T$ are extracted according to Eq. (5.7) by multiplying the model cross section $\left. \frac{d\sigma}{dt} \right|_{\text{MC}}$ with the ratio $R = Y_{\text{exp}}/Y_{\text{sim}}$. Since the model for the interference terms is good, as demonstrated by the fact that the ratio does not depend on ϕ (see Fig. 5.7), the procedure is justified.

The model cross section for each t bin is calculated at the central value of t of the bin and at the average values of W and Q^2 of the high and low ϵ data for each bin. This choice is motivated in two ways: the problem of unphysical combinations of

[‡]The VGL Regge model predicts different W dependences for the contributions from π and ρ trajectory exchanges, hence also for σ_L and σ_T . The range of the data in W does not allow a verification of this prediction.

W , Q^2 and t when using central values of W and Q^2 (that is if $-t < -t_{\min}(W_c, Q_c^2)$) is avoided in a natural way, and possible errors introduced by using wrong scaling functions in W and Q^2 are minimized.

Having extracted the unseparated cross sections $\sigma_u = \epsilon\sigma_L + \sigma_T$, the L/T separation is straightforward. The high and low values of ϵ are fixed by the choice of W and Q^2 combined with the high and low electron energies. From the low and high ϵ measurements the longitudinal and transverse components are derived as

$$\frac{d\sigma_L}{dt} = \frac{\left(\frac{d\sigma}{dt}\right)_{\text{high}} - \left(\frac{d\sigma}{dt}\right)_{\text{low}}}{\epsilon_{\text{high}} - \epsilon_{\text{low}}}, \quad (5.12)$$

$$\frac{d\sigma_T}{dt} = \frac{\epsilon_{\text{high}} \left(\frac{d\sigma}{dt}\right)_{\text{low}} - \epsilon_{\text{low}} \left(\frac{d\sigma}{dt}\right)_{\text{high}}}{\epsilon_{\text{high}} - \epsilon_{\text{low}}}. \quad (5.13)$$

It follows from Eqs. (5.12) and (5.13) that uncorrelated uncertainties on the unseparated cross sections will be magnified for the separated ones.

5.7 Estimate of uncertainties

The uncertainty in the extraction of separated cross section has statistical and systematic sources. The statistical uncertainty on the unseparated cross sections is determined by the uncertainties in Y_{exp} and Y_{sim} in Eq. (5.7). The uncertainty in the experimental yield is given by the uncertainty in the number of measured real events and the contributions from accidental coincidence events and events from the cell walls. The statistical uncertainty in the simulated yield is given simply by the uncertainty in the number of accepted simulated events. As the Monte-Carlo simulation was done for high statistics (160,000 events per kinematic setting, four times the number of experimental counts in the high energy settings), the relative statistical error on $R = Y_{\text{exp}}/Y_{\text{sim}}$ is dominated by the uncertainty in the number of measured real events.

The systematic uncertainties can be subdivided into correlated and uncorrelated contributions. Uncertainties that are the same for the high and the low ϵ data, *e.g.*, as a result of the fact that the pion arm settings are the same for both measurements (correlated uncertainties) are attributed directly to the separated cross sections. Uncorrelated uncertainties are attributed to the unseparated cross sections. Significant correlated and uncorrelated contributions to the systematic uncertainties in the cross sections are listed in Table 5.2. They are added quadratically. Dominating uncorrelated contributions are the uncertainty in the detection volume (Subsect. 5.5.3) and the correction for the reduction of the target density

source	σ_u	$\sigma_{L,T}$
detection volume	2.0%	-
target density	1.0%	-
charge measurement	0.5%	-
beta tracking efficiency	-	0.25%
pion absorption	-	1.0%
pion decay	-	1.0%
radiative processes	0.5%	1.0%
cut dependences	0.5%	0.5%
sum	2.4%	1.8%

Table 5.2: *Significant contributions to the systematic uncertainty associated with the measured $^1H(e, e'\pi^+)$ cross section. Errors that are uncorrelated between low and high ϵ data are attributed to the unseparated cross section, correlated errors to the separated ones.*

(Subsect. 5.4.5). The correlated contributions to the systematic uncertainty are dominated by pion absorption and decay (Subsects. 5.4.4 and 5.5.1) and the treatment of radiative processes (Subsect. 5.5.1).

The dependence of the extraction of separated cross sections on the cross section model in the simulation constitutes another source of systematic uncertainties. Because of the variation in the magnitude of this uncertainty from bin to bin, this contribution was studied by extracting σ_L and σ_T with different cross section models. Since the longitudinal and transverse cross sections in the model are believed to reproduce the experimental data to within 10%, these two terms were independently increased and decreased by 10% in the model. With these changes, the extracted σ_L and σ_T varied by less than 0.5%.

The interference terms σ_{LT} and σ_{TT} are not equally well known. Their contributions to the systematic uncertainties of σ_L and σ_T were studied as follows: from the fitting procedure on the ratios (see Subsect. 5.5.4) the uncertainties on the interference terms in the model were calculated. The interference terms in the cross section model were then independently increased or decreased by their respective uncertainties, and L/T separations were done with the modified models. The contribution to the uncertainty of σ_L and σ_T of these two terms is between 1% and 8% and depends strongly on t . The latter value (at the largest values of $-t$) is comparable to the contribution of uncorrelated uncertainties to σ_L and σ_T . In presenting the data, the contributions of the model uncertainty are calculated for

variable	value	Reference
Coincidence timing (ns)	$-1.07 < t < 1.25$ (exp.)	Fig. 5.2
# photo electrons SOS	≥ 0.5 (exp.)	Subsec. 5.3.1
# photo electrons HMS	≤ 0.2 (exp.)	Subsec. 5.3.1
Calorimeter sum SOS	≥ 0.6 (exp.)	Subsec. 5.3.1
HMS β	≥ 0.925 (exp.)	Subsec. 5.3.1
HMS and SOS collimators	-	Figs. 4.3 and 4.5
cut on SOS calorimeter position	-	-
HMS $ \delta $	$\leq 8.5\%$	Subsect. 4.4.1
HMS $ x'_{\text{tar}} $	≤ 60 mrad	Subsec. 4.4.1
HMS $ z_{\text{tar}} $	≤ 3.375 cm	-
SOS $ \delta $	$\leq 15\%$	Subsect. 4.4.2
SOS $ z_{\text{tar}} $	≤ 6.750 cm	-
SOS acceptance cut	-	Subsec. 5.5.3
SOS x_{fp}	$-20 \text{ cm} < x_{\text{fp}} < 22 \text{ cm}$	-
missing mass (GeV)	$0.925 < M_m < 0.980$	Fig. 5.8
cut on W and Q^2	-	Fig. 5.1

Table 5.3: Overview of the cuts used to select the data for the extraction of cross sections.

each t bin and added in quadrature to the statistical and systematic uncertainties of Table 5.2.

5.8 Analysis cuts

An overview of the analysis cuts is shown in Table 5.3. The first panel contains cuts on coincidence timing and particle identification. The second and third panels contain cuts on reconstructed target variables. Of these the first panel contains cuts on physical apertures (the collimators and the SOS calorimeter), whereas the second panel contains cuts outside of which the quality of the reconstruction decreases below acceptable limits.

The fourth panel of Table 5.3 contains cuts on the physics quantities W , Q^2 and the missing mass. The diamond shaped cuts on W and Q^2 are designed to entail the low ϵ range for both the low and high ϵ data. The missing mass range is chosen in a region where resolution effects, which affect the region of up to 20 MeV above the missing mass peak have averaged out, while errors from insufficient simulation of

radiative processes at higher missing mass have not yet set in. Therefore the result does not depend on the cut on the missing mass. The dependence on the other cuts has been checked by varying them. The change in the cross section amounted to a total of less than 1%.

Chapter 6

Results and discussion

The results of the analysis are presented in this chapter. In Section 6.1 the global behaviour of the separated experimental cross sections is discussed and compared to the Monte Carlo cross sections. Also, the measured cross sections are compared to the Regge model by Vanderhaeghen, Guidal and Laget (VGL, Ref. [Van97]). In Section 6.2 four methods of extracting F_π from our data are discussed, and in Section 6.3 the best values for F_π are obtained from that analysis. In Section 6.4, older data from DESY and CEA/Cornell are re-analyzed consistently with the present data. The chapter concludes in Section 6.5 with the presentation of our results for F_π and a discussion, followed by an outlook to future experiments.

6.1 Experimental cross sections

6.1.1 Discussion of the cross sections

The cross sections presented here have been extracted with the help of the Monte Carlo simulation SIMC using the relation Eq. (5.7) with the cross section model of Eqs. (5.8) to (5.11) and the analysis cuts of Table 5.3. The cross sections for the low and high ϵ measurements as well as the separated cross sections σ_L and σ_T are presented as differential cross sections $d\sigma/dt$, binned in the Mandelstam variable t . The cross sections are presented for average values of W and Q^2 per bin and bin centered values of t . The theoretical and Monte Carlo model predictions are calculated at the same values of W , Q^2 and t per bin. With this choice, unphysical combinations of W , Q^2 and t are avoided, and extrapolation errors in the L/T separation from low and high ϵ data are minimized (see Sect. 5.6).

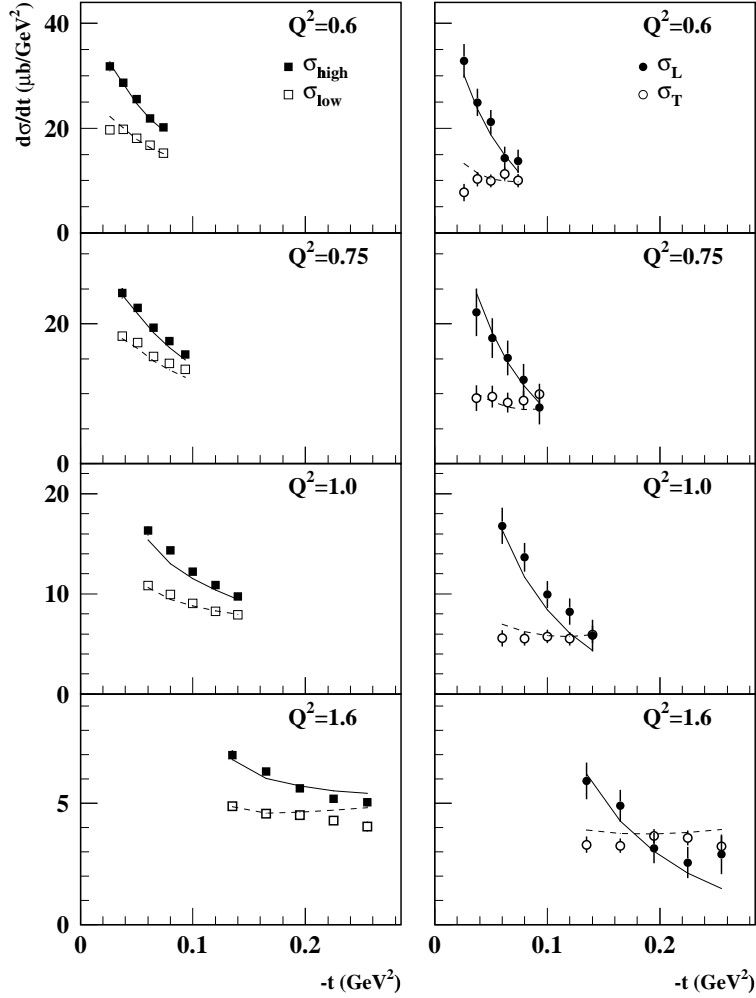


Figure 6.1: Left column: unseparated cross sections $\epsilon\sigma_L + \sigma_T$. Empty and full symbols: low and high ϵ settings. Right column: separated cross sections (open circles: σ_T , closed circles: σ_L). The solid and dashed curves are the corresponding Monte Carlo model values. The error bars on the unseparated cross sections include statistical and uncorrelated systematic uncertainties and are smaller than the symbols. Those on the separated cross sections include in addition correlated systematic uncertainties and those due to the Monte Carlo model.

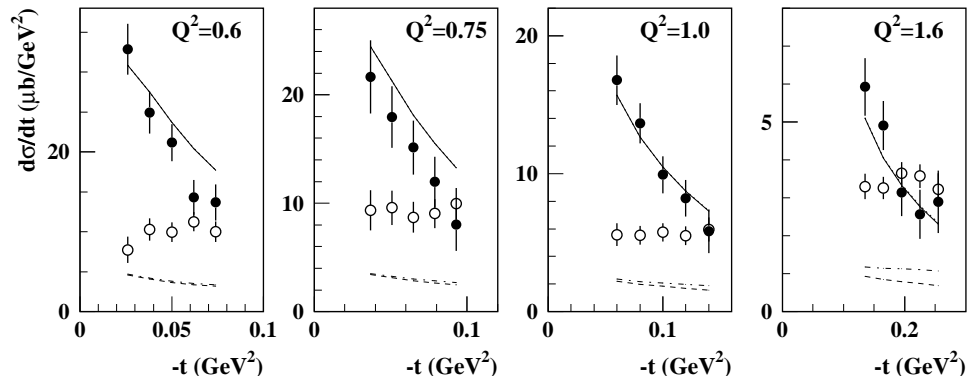


Figure 6.2: Separated cross sections for the four Q^2 points (symbols as in Fig. 6.1). The solid and dashed (dash-dotted) curves denote the results from VGL model (Ref. [Van97]) for σ_L and σ_T , respectively. The cutoff parameters in the monopole parametrizations for the π and ρ trajectories are $\Lambda_\pi^2=0.4$ (GeV/c) 2 , and $\Lambda_\rho^2=0.6$ (GeV/c) 2 (dash-dotted curve) and 2.1 (GeV/c) 2 (dashed curve), respectively.

The unseparated cross sections $\sigma_u = \epsilon \sigma_L + \sigma_T$ and the separated cross sections σ_L and σ_T are shown in Fig. 6.1 (and in Tables A.1 and A.2) together with the model cross section used in the Monte Carlo simulation (see Subsect. 5.5.4). The model cross sections are displayed as solid and dashed curves on top of the data. Note that the scale on the y-axis changes per Q^2 point, while the range on the x-axis stays the same. As mentioned in Chapter 5, the separated cross sections are reproduced by the Monte Carlo model to better than 10% on average. The longitudinal cross section exhibits the expected t-pole behaviour. The transverse cross section is mostly flat.

6.1.2 Comparison with the VGL model

Longitudinal and transverse cross sections

The Regge model of Vanderhaeghen, Guidal and Laget (VGL, Ref. [Van97], see Subsect. 2.2.3) provides a fair description of the separated cross sections of older L/T separated data (for instance the DESY data of Refs. [Ack78, Bra77] and the Cornell data of Ref. [Beb78]). Those data are in a range of Q^2 that is comparable to that of the present data, though at a higher value of W . The VGL model calculations for the longitudinal and transverse cross sections of the present data set are shown

in Fig. 6.2. Both the π and the ρ trajectories are included in the calculation. They are parametrized as monopole functions in Q^2 , with cutoff parameters Λ_π^2 and Λ_ρ^2 . The values of the cutoff parameters for the curves shown in Fig. 6.2 are $\Lambda_\pi^2=0.45$ GeV² and $\Lambda_\rho^2=0.6$ or 2.1 GeV². The longitudinal cross section is insensitive to the ρ trajectory (at these values of $-t$ the two curves for σ_L for the two values of Λ_ρ^2 lie on top of each other), whereas the transverse cross section differs noticeably for the two different values of Λ_ρ^2 at large values of $-t$.

The VGL model calculation for σ_L gives the right magnitude. By adjusting Λ_π^2 , σ_L^{VGL} can be increased or decreased. The t dependence of the longitudinal cross section data is somewhat steeper than that of the model. This may indicate that the model lacks a negative background term. The model underestimates the experimental data for σ_T by more than a factor of two. Since the Jefferson Lab data have been taken at relatively small values of W around 1.95 GeV, contributions from the resonance region may enhance the strength in σ_T . No such terms are included in this Regge model. However, these contributions are expected to be small in the longitudinal cross section at small values of $-t$, where σ_L is dominated by the pion exchange t-pole diagram.

Interference terms

The interference terms σ_{LT} and σ_{TT} have not been extracted explicitly from the data. However, these terms were globally fitted as function of Q^2 and $-t$ using the fitting procedure described in Subsec. 5.5.4. The thus obtained values of σ_{LT} and σ_{TT} as calculated from the Monte Carlo model are compared to those of the VGL model in Fig. 6.3. The sign convention is the one from Equations (5.10) and (5.11), which is opposite to the one of Ref. [Van97]. The sign of VGL curves was inverted in Fig. 6.3 to account for this. Because of their intrinsic $\sin\theta^*$ ($\sin^2\theta^*$) dependences, the terms go to zero when θ^* goes to zero. The slope of the σ_{LT} interference term is reproduced correctly by the VGL model at all values of Q^2 , but the model cross section has an offset with respect to the data. The offset decreases with increasing Q^2 . The absolute value of the σ_{TT} term from the VGL model is generally smaller than that of the data. The findings are probably in keeping with the failure of the VGL model to describe the magnitude of the transverse cross section, since the same currents that enter into the calculation of the transverse cross section play a role in the interference terms. If σ_T is larger than calculated, σ_{TT} may be larger, and σ_{LT} may be influenced as well.

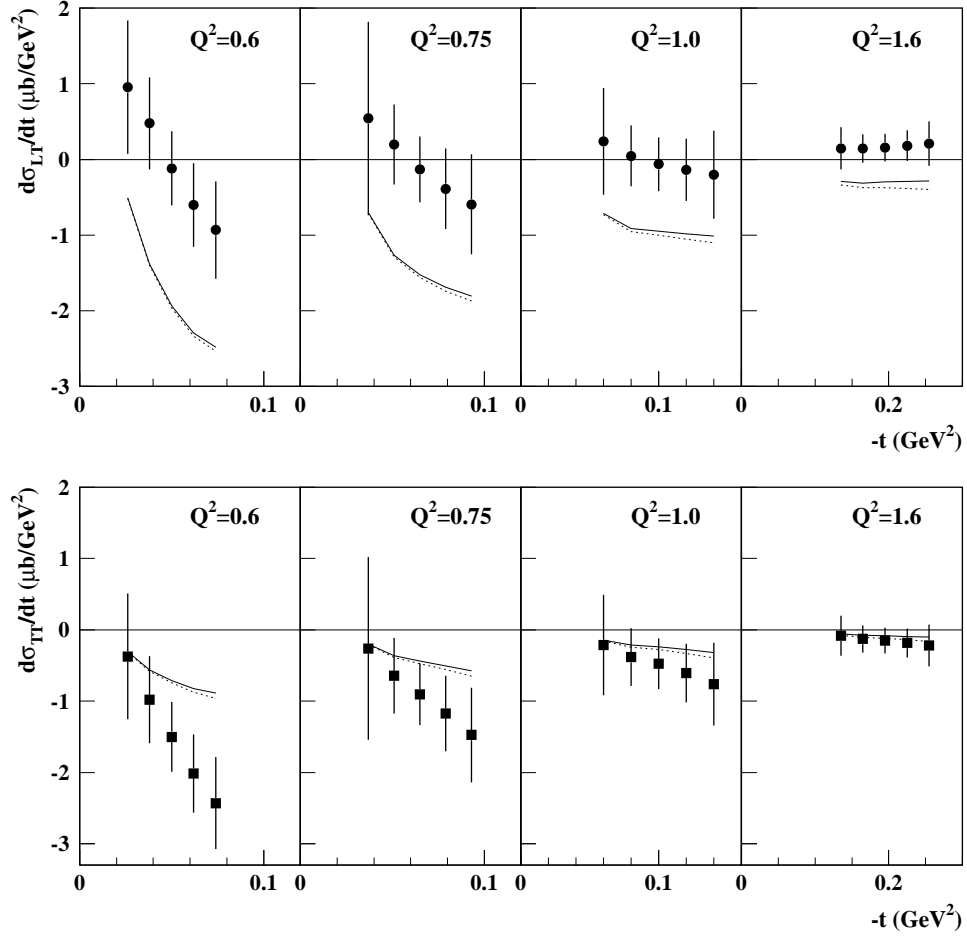


Figure 6.3: Cross sections σ_{LT} (top) and σ_{TT} (bottom), calculated from the Monte Carlo model that was fitted to the experimental data. The errors bars are calculated from the fitting uncertainty. The solid and dashed lines represent the VGL model results for σ_{LT} and σ_{TT} with values of $\Lambda_\pi^2=0.45$ $(\text{GeV}/c)^2$, $\Lambda_p^2=0.6$ and 2.1 $(\text{GeV}/c)^2$, respectively.

6.2 Extraction of the pion form factor

For the extraction of F_π from the present data, the Regge model of Vanderhaeghen, Guidal and Laget is used because it has been shown to be able to qualitatively and quantitatively describe a range of processes (see Subsec. 2.2.3). The VGL model is in fair agreement with the present data for σ_L , but does not agree well with the data for σ_T , σ_{LT} and σ_{TT} . However, since σ_L is dominated at small values of $-t$ by the pure t-channel process, other process are supposed to have only limited influence on the extraction of F_π from σ_L .

The dependence of the extraction of F_π on the ρ Regge trajectory was checked by varying the Λ_ρ^2 cutoff parameter. This has a large influence on the transverse cross section (see Figure 6.2). The model for σ_L did not change significantly, even if the ρ trajectory exchange was omitted entirely. However, as mentioned above, the VGL model for σ_L does not match the experimental data perfectly. In the following, four different approaches to extract F_π using the VGL model are explored. In Section 6.5 it is discussed how to arrive at the best value for F_π .

6.2.1 Pure VGL model

The simplest way to extract values for F_π from the experimental data is by means of a least squares fit of the VGL model prediction for σ_L to the experimental data (method 1). The model σ_L includes F_π in a monopole parametrization with Λ_π^2 as cutoff factor. Since F_π does not have to follow a monopole parametrization, Λ_π^2 can be chosen freely and dependent on Q^2 . It is used as the fit parameter in a one-parameter fit. The value of F_π is then calculated as $F_\pi(Q^2) = (1 + Q^2/\Lambda_\pi^2)^{-1}$ with Λ_π^2 taken at the minimum of the $\chi^2/d.f.$ distribution.

Fig. 6.4 shows that the values of F_π derived in this way are largest if only the first bin is used in the fit, and decrease if more t bins are included. This is a direct consequence of the fact that the σ_L data have a steeper t dependence than the VGL model predictions. Since the dominance of the pure t-channel process over background processes is expected to be stronger at small values of $-t$, the value of F_π extracted at the lowest value of $-t$ is considered to be most trustworthy. In order not to rely on only one bin, the dependence of F_π on the number of bins used in the χ^2 fit is interpolated with a linear function, and the value of the interpolation is taken at the position of the first bin*. The values for F_π are shown in the left hand plot of Figure 6.5 and are listed in Table B.1.

*It should be noted that it is not meaningful to use this method for an extrapolation to the pion pole, because the bins do not correspond to values of $-t$ but to numbers of bins used in a fit.

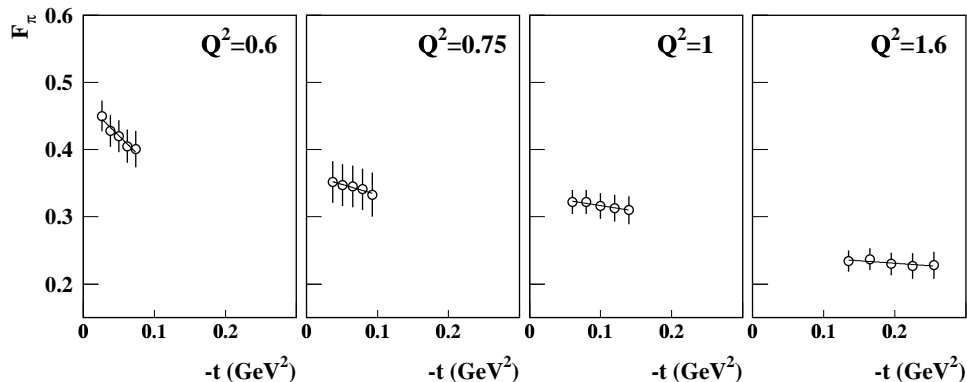


Figure 6.4: *Dependence of the extracted value for F_π on the number of t bins used in the fit (method 1). Each subsequent bin corresponds to the usage of one more data point from Fig. 6.2.*

6.2.2 VGL model with constant background term

The difference in the t dependence of σ_L between the experimental data and the VGL model may be explained by the presence of a negative background term. Such an effect was effectively produced in the Born term model of Gutbrod and Kramer (Ref. [Gut72]), which was used in the analysis of the data from Ref. [Bra77]. In order to better describe the t dependence of existing data, the authors fitted the nucleon form factors in their model and introduced a $g_{\pi NN}$ form factor. According to these authors, the use of modified nucleon form factors is equivalent to adding terms into the dispersion integrals with a Q^2 behaviour different from that of the nucleon pole. As a result the model prediction for σ_L decreased over the whole (large) range of $-t$ covered in that experiment.

Such an effect is used in analysis method 2. Assuming that there are background terms to σ_L that are not included in the VGL model, a constant background term c is subtracted from the VGL model prediction for σ_L . In order to compensate for this decrease, larger values for the input parameter Λ_π^2 to the VGL model are used. This results in a steeper t dependence of the thus obtained model for σ_L and a better fit to the experimental data. The best values for Λ_π^2 and c for each value of Q^2 are obtained in a two-parameter least squares fit. In this way, the t dependence of the result for F_π from method 1 is avoided. The resulting values for F_π and c are shown in the second plot of Figure 6.5 and are listed in Table B.2.

6.2.3 t -dependent F_π

If one assumes that the background terms in σ_L are adequately included in the VGL calculations, the discrepancy of the VGL model prediction for the t dependence of σ_L may be attributed to a t -dependence of F_π (the initial pion is off-shell). A very simple way of parametrizing such a t -dependence is to change the monopole function in Q^2 into a monopole function in Q^2 and t . In this way, the VGL model prediction is re-calculated with the “off-shell” F_π (method 3)

$$F_\pi(Q^2, t) = [1 + Q^2/\Lambda_\pi^2 - a/\Lambda_\pi^2 (t - M_\pi^2)]^{-1}. \quad (6.1)$$

The parametrization takes into account that at $t = M_\pi^2$ the pion is on-shell, and F_π resumes its on-shell form. Together with Λ_π^2 , the parameter a is used as a free parameter, just as the parameter c was in the previous Subsection.

The results of method 3 are shown in Figure 6.5 and in Table B.3. The fit yields generally larger values of Λ_π^2 (and thus F_π) and much larger uncertainties than method 2. This can be explained with the fact that large values of a are needed to increase the slope of σ_L . Large values of Λ_π^2 are then needed to fit the data (see Eq. (6.1)).

6.2.4 $g_{\pi NN}$ -like t -dependence

Another approach to explicitly introduce a t dependence follows the example of Gutbrod and Kramer (Ref. [Gut72], see also Subsec. 6.2.2). Their model, which includes Born terms and resonance contributions, does not properly reproduce the t dependence of the photo- and electroproduction cross sections of Ref. [Dri71]. Hence, the authors multiplied the Born term amplitudes of their model with an exponential function $f(t) = e^{t/M^2}$ (with M being the nucleon mass), which improved the fit of their model to the data. They identified the exponential function with the pion-nucleon form factor, $g_{\pi NN}$.

In the VGL model there is in principle no need to use a pion-nucleon form factor, since the full Regge trajectories effectively take this into account (compare dashed and solid curves in Figure 2 of Ref. [Van97]). However, one could assume that there is an additional t dependence. In order to investigate such an option, the VGL model prediction for σ_L is modified with $e^{\alpha t}$, where α is used as a free parameter (method 4). The analysis proceeds as in the previous two cases. The results are shown in the right hand plot of Fig. 6.5 and listed in Table B.4.

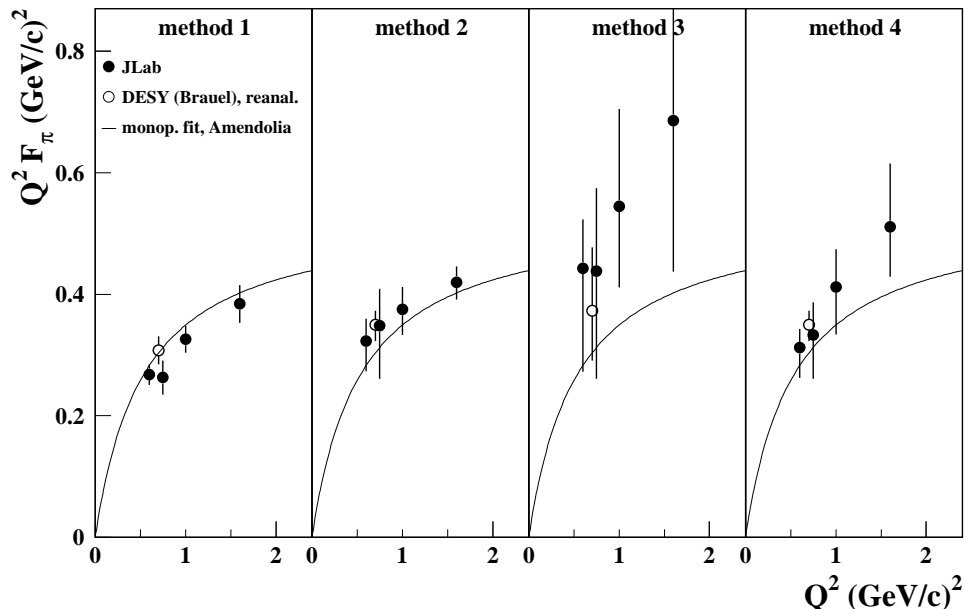


Figure 6.5: Results of the four methods for extracting F_π discussed in Subsections 6.2.1 through 6.2.4. The curve, which is meant as a reference for the data, and is the same in all panels, represents the monopole parametrization of F_π by Amendolia et al. (Ref. [Ame86]). The DESY data points are from the re-analysis (see Section 6.4).

6.3 Best values for F_π

In Section 6.2 the extraction of values for F_π from the present data using the VGL model is discussed. The four methods described in Subsections 6.2.1 to 6.2.4 (methods 1 to 4) yield different results for F_π . Therefore, while it is not possible to give a final answer to the question what the value of F_π in the region of Q^2 between 0.6 and 1.6 $(\text{GeV}/c)^2$ really is, the results can be used to determine the best values for F_π and to make an estimate for the model uncertainty.

The smallest values for F_π are obtained in method 1. Here, the VGL model for σ_L is not changed. However, we have argued that there may be negative background terms to σ_L missing in the VGL model, which gain influence at larger values of $-t$ and thus decrease the resulting value for F_π if more t bins are included in the analysis. Since there is no reason to assume that such background terms are absent

Q^2 (GeV/c) ²	F_π	$Q^2 F_\pi$ (GeV/c) ²
0.60	$0.493 \pm 0.022 \pm 0.046$	$0.296 \pm 0.013 \pm 0.028$
0.75	$0.407 \pm 0.031 \pm 0.057$	$0.306 \pm 0.023 \pm 0.043$
1.00	$0.351 \pm 0.018 \pm 0.025$	$0.351 \pm 0.018 \pm 0.025$
1.60	$0.251 \pm 0.016 \pm 0.010$	$0.402 \pm 0.026 \pm 0.016$
0.70^a	$0.471 \pm 0.032 \pm 0.030$	$0.330 \pm 0.022 \pm 0.021$

^afrom reanalysis of data from [Bra77]

Table 6.1: *Best values for F_π and $Q^2 F_\pi$. The combined statistical and systematic uncertainties are given as well as the model uncertainty. The re-analyzed DESY data point is included (see Subsection 6.4.1). In the case of the DESY data point the first uncertainty only includes contributions from the statistical uncertainty.*

at the lowest $-t$ bin, the value obtained there is considered to be a lower limit for F_π .

In the other three methods the VGL model for σ_L is changed in order to better fit the data. In method 2 this is done by subtracting a term c from σ_L , which is constant as a function of $-t$. This is based on the work by Gutbrod and Kramer (Ref. [Gut72]), who fitted experimental data by fitting nucleon form factors and found that as a result σ_L decreased over the whole range in $-t$. However, one may assume that the background to σ_L has a similar behaviour as the one in σ_T . The difference between the experimental data and the VGL model for σ_T (see Fig. 6.2) indicates that the background to σ_T increases with $-t$. With an increasing background the value of F_π would come out lower. Therefore the results obtained here are taken as an upper limit for F_π . In methods 3 and 4, F_π is made t dependent or multiplied by a form factor $e^{\alpha t}$. Since these adaptations are done ad hoc and may spoil gauge invariance, we think that these results are not very realistic, and we therefore discard them in the further discussion.

The results of methods 1 and 2 are phenomenological approximations to the problem of reconciling the VGL results with the experimental data. This yields realistic lower and upper estimates for F_π . Our best estimate for F_π is therefore taken to be the average of the values of methods 1 and 2. To these values we assign a model uncertainty of half of the spread between the lower and upper values, in addition to the uncertainty that is derived from the statistical and systematic uncertainties on the cross sections. The latter is between 5 and 7.5%, while the

model uncertainty is between 4 and 14%. The results thus obtained are shown in Figures 6.6 and 6.7 and in Table 6.1.

6.4 Reanalysis of existing data

6.4.1 DESY data

Brauel *et al.* (Ref. [Bra77]) have provided the only previous L/T separation with sets of high and low ϵ data from one experiment. The Q^2 value of 0.7 (GeV/c)² is within the range of the present data, but the central value of $W=2.19$ GeV is higher. The DESY cross section data are shown in Fig. 2.6. Like in the analysis of the Jefferson Lab data, the DESY data were analyzed using a Monte Carlo simulation to model the spectrometer acceptances. However, whereas the present analysis uses a detailed model cross section in the extraction of cross sections (see Subsection 5.5.4), the model cross section in the DESY simulation only included the virtual photon flux factor Γ_V of Equation (2.8) and the phase space factor $(W^2 - M_p^2)^{-2}$.

The DESY data are averaged over large ranges in W and Q^2 (W from 2.06 to 2.37 GeV, Q^2 from 0.5 to 0.9 (GeV/c)²) and the cross section data are presented at a common value of W and Q^2 for all t bins. As discussed in Subsection 5.5.4, this may lead to averaging and scaling errors. Because of the correlations between t , W and Q^2 (see Fig. 5.1), such averaging errors tend to work in opposite directions at small and large values of $-t$ and thus can cause a change in the slope of the t dependence of the cross sections. A similar argument holds for the fitting of the cross sections σ_{LT} and σ_{TT} . In the DESY analysis these terms were fitted for bins in t and ϕ_π , with implicit averaging over θ^* . Because of the intrinsic θ^* dependence of σ_{LT} and σ_{TT} , such a fit may yield incorrect results due to the bin-to-bin change in the average values of θ_π^* , Q^2 and W . If the interference terms have not been determined correctly, errors in the extraction of σ_L and σ_T will result.

However, since we cannot repeat the DESY cross section determination, we have taken their published cross section values (Table 7 of Ref. [Bra77] (b)) and used these to determine F_π in the same way and with the same model as for our own data, as described in Subsections 6.2.1 to 6.2.4. The authors originally used the modified Born term model of Gutbrod and Kramer (Ref. [Gut72]) to extract a value for F_π from their σ_L data. The pure VGL model for σ_L already agrees better with the DESY data than with the Jefferson Lab data. Consequently, when using the methods described in Subsections 6.2.1 through 6.2.4, the fits to the DESY data are better constrained, and the four results have smaller error bars and scatter less

than the present data. The results of this re-analysis are included in the plots (and tables) of the Jefferson Lab results (see Fig. 6.5). The values for F_π from the re-analysed DESY data generally agree with the Jefferson Lab results and lie between 5% and 17% above the originally quoted DESY results.

6.4.2 CEA/Cornell data

The data set for F_π most frequently quoted in theoretical papers is the one by Bebek *et al.* (Ref. [Beb78]). In the original analysis of these data, unseparated cross sections were extracted from data from four different experiments at Cambridge and Cornell. For each measurement, only data with $\theta_\pi^* \leq 3^\circ$ were considered. In this case of near parallel kinematics the interference terms can be neglected, provided the ϕ_π coverage was uniform. Because of the small numbers of counts the statistical uncertainty on the cross sections is large, between 8% and 24%. Separations of σ_L and σ_T were attempted for three values of Q^2 , where measurements at different electron energies existed that were taken in experiments over the course of several years. However, the uncertainty on the separated cross sections was very large. Therefore, the authors fitted the total photoproduction cross section σ_{tot} to the separated σ_T data and used the relation $\sigma_T = 0.025 \sigma_{\text{tot}}$ to subtract it from the unseparated cross section and thus to determine σ_L . The W -dependence of the relation for σ_T was assumed to be the same as for the s - and u -channel Born terms. Although this relation was obtained in a fit to the extracted σ_T data, the uncertainty on σ_T was set to zero. Then the authors used the extended Born term model of Berends (Ref. [Ber70]) to extract values for F_π .

Here we present a re-analysis of the CEA/Cornell data with values of Q^2 between 0.4 and 2.01 (GeV/c)². We make use of the fact that we have now a Monte Carlo cross section model for σ_T , fitted to experimental data in a range of Q^2 between 0.6 and 1.6 (GeV/c)², whereas the authors had little experimental information on σ_T . In the re-analysis of the CEA/Cornell data σ_L is determined from the original unseparated cross sections using the transverse cross section data from the Monte Carlo model, calculated at $\theta_\pi^*=0$. The resulting σ_L data are then compared to the predictions of the VGL model.

Our cross section model, which has been fitted to data with values of W below 2 GeV, is extrapolated up to W between 2.11 and 3.09 GeV for use with the CEA/Cornell data. Even if the extrapolation to high values of W introduces an uncertainty, this is much smaller than the systematic uncertainties of the Bebek data. This becomes clear when one looks at the results for the data points at values of Q^2 between 1.2 and 2.0 (GeV/c)², for which there are multiple measurements in

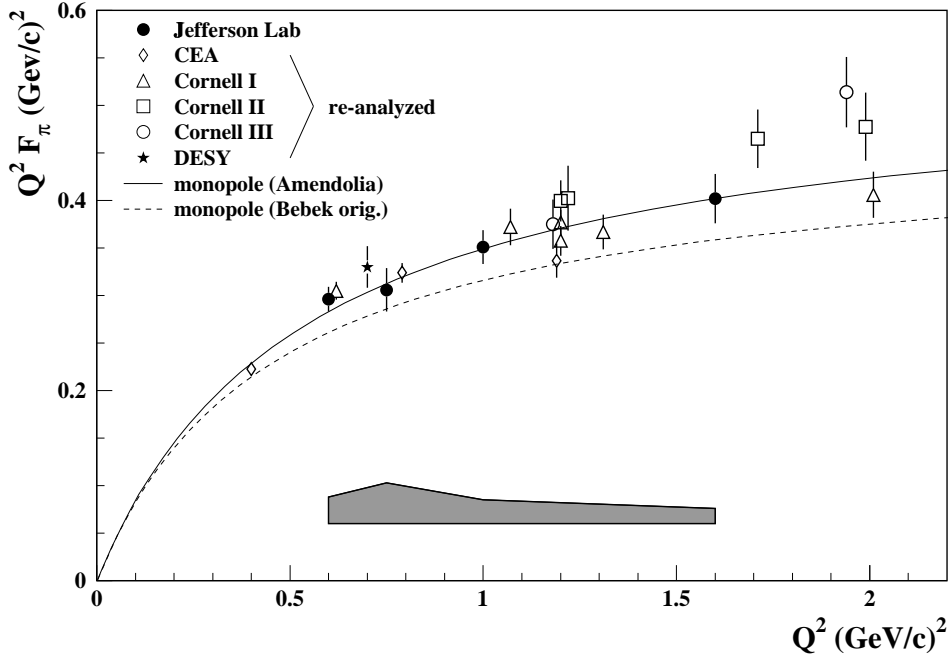


Figure 6.6: World data set for the pion form factor up to $Q^2=2.01$ $(\text{GeV}/c)^2$. Jefferson Lab and DESY data: best values based on our analysis. The error bars correspond to the combined statistical and systematic uncertainties for the Jefferson Lab data and the statistical uncertainty only in case of the DESY data, as given in Table 6.1. The grey band at the bottom of the plot gives the model uncertainty for the Jefferson Lab data. The CEA/Cornell data are re-analyzed with the Jefferson Lab model for σ_T and the VGL model. The error bars correspond to the statistical uncertainty on the total cross sections only (systematic or model uncertainties not included). The curves are a monopole parametrization of F_π of Amendolia (solid curve, Ref. [Ame86]) and the old monopole fit to Bebek's original result for comparison (dashed curve, Ref. [Beb78]).

the data set (see Table B.5). While the resulting values of F_π hardly depend on the W values of the data points, their scatter, which is about 17% at $Q^2=1.2$ (GeV/c)² and 27% at $Q^2=2.0$ (GeV/c)², gives an estimate of the systematic uncertainty of these measurements.

For almost all data points the newly estimated σ_T is smaller than the values quoted in Ref. [Beb78]. Hence, σ_L and F_π increase with respect to the older data. The results are shown in Fig. 6.6 and listed in Table B.5 together with the re-analyzed DESY data point and the present data.

6.5 Discussion

In Section 6.3 best values for F_π have been determined as the average of the results from fitting methods 1 and 2. The resulting values for F_π are shown in Figures 6.6 and 6.7 and in Table 6.1. Also displayed are the results of the re-analysis of the DESY and the CEA/Cornell data. Figure 6.6 shows that these data are in agreement with the Jefferson Lab results. The new DESY F_π point has been obtained in the same way as the Jefferson Lab points, as the average between the results of methods 1 and 2. It is included in Table 6.1. As mentioned before, the difference between the two methods is smaller in the DESY data, which may be explained by the fact that these data were taken at a higher value of W . The VGL model is better suited to this region, since the extra background to σ_L may be smaller. Indeed, the constant background term c in the fit in method 2 is smaller for the DESY data than for the Jefferson Lab data (see Table B.2).

The results for F_π from the re-analyzed CEA/Cornell in the range of Q^2 between 0.6 and 1.3 (GeV/c)² are in agreement with the Jefferson Lab results as well, despite the fact that the data scatter considerably. One should notice that only the statistical uncertainties on the total cross sections are reflected in the error bars on the CEA/Cornell data in Figure 6.6. The new values of σ_T from the Monte Carlo model cross section were subtracted with an uncertainty of zero. The model uncertainty for using the VGL model is put to zero as well.

These findings show that, although the data from Jefferson Lab, DESY and CEA/Cornell have been taken under very different kinematic and experimental conditions, the different measurements yield consistent results, if they are analyzed in the same way. This gives us confidence in the VGL model predictions for σ_L even at relatively small values of W . Otherwise, the results for F_π from different data sets would not agree as well as they do.

The picture that emerges from these findings is that up to values of Q^2 of 2 (GeV/c)² the value of F_π follows rather well a monopole form obeying the pion

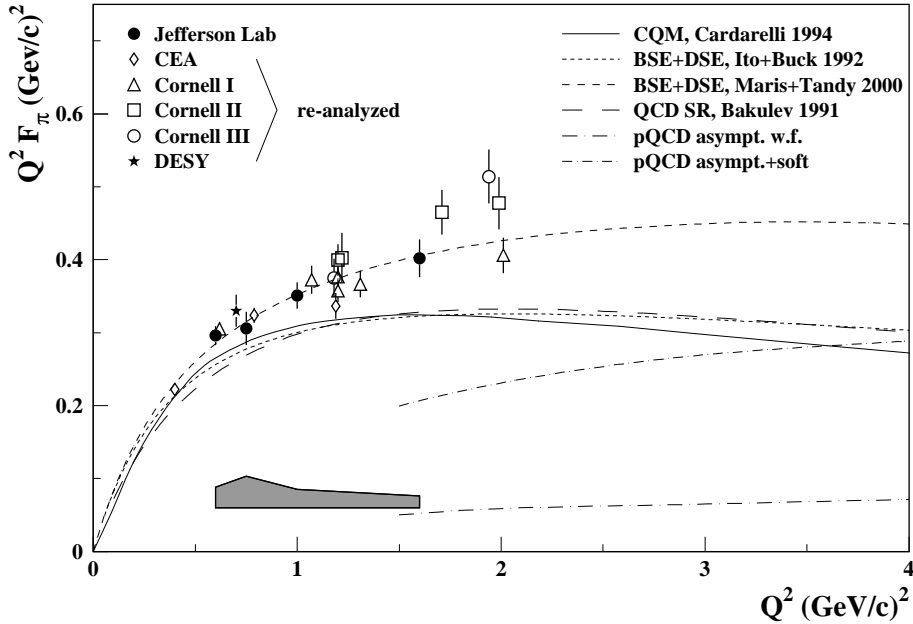


Figure 6.7: *Jefferson Lab and DESY best values for F_π and re-analyzed CEA/Cornell data compared with the theoretical curves from Fig. 2.11 (see Section 2.4). The systematic and model uncertainties are displayed as in Figure 6.6.*

charge radius (Ref. [Ame86], $\Lambda_\pi^2 = 0.54 \text{ (GeV/c)}^2$). In the region between $Q^2 = 0.6$ and 1.6 (GeV/c)^2 this is about 10% higher than the previously used values from the old CEA/Cornell data of Ref. [Beb78]. Those authors fitted their data with a monopole function in an attempt to determine the pion charge radius. The value of the cutoff factor Λ_π^2 they found was 0.462 (GeV/c)^2 . The corresponding pion charge radius was 0.711 fm, or about 7% larger than the value of 0.662 fm, which was measured later in the low- Q^2 measurements of Amendolia *et al.* (Ref. [Ame86]).

The result for $Q^2 F_\pi$ from the Jefferson Lab data is displayed in Figure 6.7 together with the theoretical predictions discussed in Section 2.4, which were also shown in Figure 2.11. Most of the models incorporate the asymptotic behaviour of F_π . Although not all of them reproduce the correct pion charge radius, they reach a maximum in $Q^2 F_\pi$ and decrease more or less rapidly after that. They differ in the value of Q^2 where the maximum is reached and in the height of the maximum. The present data indicate that up to $Q^2 = 1.6 \text{ (GeV/c)}^2$ F_π is still rising,

and that the maximum has to be expected beyond $2 \text{ (GeV}/c)^2$, with a value of $Q^2 F_\pi$ at the maximum around or above $0.4 \text{ (GeV}/c)^2$. Most of the theoretical curves lie below the F_π data. An exception is the calculation by Maris and Tandy (Ref. [Mar00]), following earlier work by Maris and Roberts (Ref. [Mar98]), which is based on the Bethe-Salpeter equation with quark propagators calculated using the Dyson-Schwinger equation. The parameters in this model were determined without using F_π data. In the Q^2 range presented here, the model curve closely follows the monopole fit to the Amendolia data (Ref. [Ame86]), and describes the F_π data remarkably well. In this model, the maximum of the $Q^2 F_\pi$ distribution is reached around $Q^2=3.5 \text{ (GeV}/c)^2$ with a value of $Q^2 F_\pi$ of about 0.45.

Outlook

Future experiments are needed to address the W dependence of the pion electroproduction cross section and the behaviour of F_π at higher values of Q^2 . The extension of the present experiment in Hall C, proposal E96-007 (Ref. [Mac96]), has been accepted and will be done in the year 2001 or 2002. In that experiment measurements will be done for values of Q^2 of 2.4 and $3.2 \text{ (GeV}/c)^2$. The maximum of the $Q^2 F_\pi$ distribution is probably within the range of these data points. With the proposed upgrade of the CEBAF accelerator to electron energies of up to 12 GeV, and with a new spectrometer in Hall C with smaller minimum angle, measurements at still higher values of Q^2 and especially W will be feasible at Jefferson Lab. By measuring at higher values of W one could enhance the applicability of models such as the VGL model for the interpretation of the data, and one would decrease the minimum value of $-t$ at which data can be taken, thus moving closer towards the pion pole. Furthermore, the addition of W values would allow one to measure the W dependence of the individual transverse and longitudinal cross sections, which would result in smaller model uncertainties for F_π . This study would also be interesting in the light of the prediction of the VGL model that σ_L and σ_T have different W dependences.

Another possible experiment where F_π could in principle be studied is the HERMES experiment at DESY (Ref. [Ack98, Ste99pc]). As the resolution of the spectrometer is not sufficient to separate the pion ground state from the resonances, one would need a model for π^+ production off the Δ resonance. Since an L/T separation is needed, the fixed electron energy of 27.5 GeV must also be lowered for a dedicated run. It might then be possible to use HERMES measurements of pion electroproduction for the extraction of F_π . At the higher values of W and Q^2 that can be reached at HERMES the count rate will be very low because of the

small cross sections and luminosity of HERMES. However, the larger acceptance of the HERMES spectrometer and longer running times or dedicated runs at higher luminosities may compensate for these drawbacks.

Apart from the new data for F_π that are presented here, the data for the four separated cross sections can serve as a test for any Born term or Regge model, such as the VGL model, that yields the W , Q^2 and t dependences of the separated cross sections. Measurements of all four structure functions at higher values of W and Q^2 would serve to improve models such as the VGL model and put them on a broader experimental basis. Such models then can be used to extract F_π with smaller model uncertainties. The present F_π data and the re-analysis of the older data already constitute a significant improvement in the knowledge of F_π for the range of Q^2 between 0.6 and 1.6 (GeV/c)² and will serve as input to theoretical models that calculate F_π non-perturbatively.

Chapter 7

Summary

The nature of the particles that form the atomic nucleus, such as the nucleons and the pion, is described in Quantum Chromodynamics (QCD) in terms of more fundamental constituents, the quarks and gluons. The existence of quarks and gluons is well established by experiment. However, the structure of nucleons and pions (and other hadrons) cannot be calculated *ab initio* in QCD from the interactions between the quarks and gluons. Instead, effective models have been developed, which describe the low-energy interactions of quarks and gluons and make predictions for the hadronic structure.

One way to study the structure of hadrons experimentally is by measuring their electromagnetic form factors. These contain information about the distribution of electromagnetic charge and current in the hadron. The experimental data on form factors can be used to constrain the theoretical models. In this dissertation the electromagnetic form factor of the charged pion, F_π , is studied. The pion form factor is particularly interesting because the π meson has a simpler structure than the nucleons, and, thanks to its small mass, it is more easily produced experimentally than other mesons. Another advantage of studying the pion form factor over the investigation of nucleon form factors is that its behaviour in the limit of infinite momentum transfer (asymptotic limit) is known from the decay of the pion, whereas the asymptotic limit of nucleonic form factors is not known. At the other end of the scale very precise measurements of F_π exist for values of the square of the four-momentum transfer Q^2 below $0.28 \text{ (GeV}/c)^2$. These measurements have been used to determine the pion charge radius. Although many theoretical models incorporate the same known behaviour of F_π at very small and very large values of Q^2 , they

predict rather different values of F_π in the intermediate Q^2 region. Therefore, measurements of F_π in this region will help to constrain these models.

New measurements are needed, since few sound experimental data from earlier experiments are available for values of Q^2 above 0.7 (GeV/c)^2 , where the theoretical models differ most. The measurements of pion electroproduction in experiment E93-021, which are discussed in this dissertation, were done in the end of 1997 in Hall C of Jefferson Laboratory, Newport News, Virginia. They cover the range in Q^2 from 0.6 to 1.6 (GeV/c)^2 and represent the first phase of measurements that will be used to determine F_π up to $Q^2=3.2 \text{ (GeV/c)}^2$. The measurements, in which pions were produced by scattering of electrons from protons, were done at two electron energies (between 2.4 and 4.0 GeV) for each value of Q^2 . The cross section due to longitudinally polarized photons (σ_L) was extracted from these data by means of a Rosenbluth separation. When the pion is emitted in the direction of the photon, this part of the cross section is dominated by the direct coupling of the photon to a virtual pion in the proton. The strength of the direct coupling of the photon to the pion is governed by the pion form factor. In addition to these measurements, positively and negatively charged pions were produced off deuterium for tests of background processes.

The calibration of the optical properties of the two magnetic spectrometers in Hall C is an important part of the analysis effort described in this thesis. The High Momentum Spectrometer (HMS) was for the first time used in a new setup (tune) that allowed it to be set at forward angles as small as 10.5 degrees. The development, implementation and calibration of the new HMS tune were paramount for providing data that could be used for the Rosenbluth separations. Furthermore, the optical properties, saturation effects and the acceptance of the other Hall C spectrometer, the Short Orbit Spectrometer (SOS), were studied in detail. The understanding of spectrometer acceptances was tested by measuring the elastic scattering of electrons from protons. The cross sections derived from these measurements agree with the world data for this process to better than 2% . The methods of the calibration of spectrometer optics and of the determination of experimental offsets that have been developed during the analysis of the calibration data for this experiment have been used in subsequent Hall C experiments.

The pion electroproduction data from this experiment have unprecedented small statistical uncertainties. Unseparated and separated cross sections were extracted with the help of a Monte Carlo simulation. The simulation takes into account acceptances, resolution effects and other physical effects, such as radiative processes, pion absorption and pion decay. For the simulation a detailed model for the cross sections was fitted to the experimental data. The use of such a cross section

model helps to minimize systematic errors when one averages over large regions of phase space. Based on these cross section data, the extraction of F_π was done using a recent Regge model developed by Vanderhaeghen, Guidal and Laget (VGL, Ref. [Van97]), which agrees with previous pion electro- and photoproduction data. However, the predictions of this model for σ_L show deviations from the measured data. With reasonable assumptions for a background term to σ_L we obtained an improved description of the data and determined best values for F_π as well as the model uncertainty thereof.

The older DESY and CEA/Cornell data (Ref. [Bra77, Beb78]) were re-analyzed in a way consistent with the present analysis using the VGL Regge model to extract values for F_π from the longitudinal cross section data from those experiments. In the case of the CEA/Cornell data, an additional improvement was made with respect to the original analysis. The authors did not have enough experimental data to determine σ_L and the transverse cross section σ_T satisfactorily from their measurements. They extracted σ_L by subtracting an assumed relation for σ_T from the measured total cross sections. In the present re-analysis of the CEA/Cornell data, σ_L was determined by subtracting σ_T from the Monte Carlo cross section model that was fitted to the Jefferson Lab cross section data. The F_π values from the older data have much larger uncertainties than the new measurements. However, all data from the re-analyzed DESY and CEA/Cornell measurements up to $Q^2=2$ (GeV/c)² are in agreement with the Jefferson Lab data for F_π . The data follow a monopole form which reproduces the pion charge radius.

The results of this study indicate that a maximum in the distribution of $Q^2 F_\pi$ can be expected at values of Q^2 greater than 2 (GeV/c)², with a maximum value of $Q^2 F_\pi$ of close to or above 0.4 (GeV/c)². Almost all theoretical predictions for the location and size of the maximum disagree in these quantities. Only the most recent calculation by Maris and Tandy (Ref. [Mar00]) gives a good description for the new data up to $Q^2=2.0$ (GeV/c)². The second phase of measurements for F_π at Jefferson Lab, where measurements will be done at values of Q^2 of 2.4 and 3.2 (GeV/c)², will have the potential to improve the knowledge of F_π further and to show at which value of Q^2 the maximum is located. These measurements may even start to give insight into how fast F_π approaches asymptotic behaviour. These characteristics could then be used to distinguish between models that produce otherwise similar predictions for F_π .

Finally, the separated pion electroproduction cross sections extracted from the Jefferson Lab data are precise enough that they can be used to improve Born term or Regge models. These models could then be used to determine F_π with greater precision from the measured data. Future pion electroproduction measurements

could provide improvements to the extraction of F_π , if in addition to measuring the Q^2 dependence of the cross section, the dependence on the invariant mass W would be studied by taking data at higher values of W . This would be useful because Regge models predict that σ_L and σ_T have different dependences on W . If these were known, the systematic errors made in extracting σ_L and σ_T , and hence F_π , from data that are averaged over W could be decreased further.

Appendix A

Tables of cross sections

All relevant information for the unseparated and separated cross sections are listed for each t bin in Tables A.1 and A.2. For each bin the value of t is the center value of the bin, whereas the values of W and Q^2 are the weighted average for each t bin, averaged over the high and low ϵ data. The values of ϵ and θ_π^* are calculated from W , Q^2 and t in each bin, and the high and low electron energies in the case of ϵ . These values of ϵ and θ_π^* may differ slightly from the weighted average values for each bin.

Q^2 (GeV/c) ²	W (GeV)	t (GeV ²)	θ_π^* (deg)	ϵ_{low}	σ_{low} ($\mu\text{b}/\text{GeV}^2$)	ϵ_{high}	σ_{high} ($\mu\text{b}/\text{GeV}^2$)
$Q^2=0.6$ (GeV/c) ²							
0.526	1.983	0.026	3.7	0.364	19.69 \pm 0.66	0.732	31.77 \pm 0.96
0.576	1.956	0.038	6.6	0.379	19.74 \pm 0.53	0.738	28.69 \pm 0.77
0.612	1.942	0.050	9.0	0.382	18.04 \pm 0.47	0.739	25.60 \pm 0.68
0.631	1.934	0.062	11.2	0.383	16.73 \pm 0.45	0.739	21.83 \pm 0.63
0.646	1.929	0.074	13.1	0.384	15.26 \pm 0.46	0.739	20.12 \pm 0.64
$Q^2=0.75$ (GeV/c) ²							
0.660	1.992	0.037	4.1	0.411	18.26 \pm 0.60	0.696	24.41 \pm 0.75
0.707	1.961	0.051	7.0	0.432	17.34 \pm 0.48	0.706	22.25 \pm 0.60
0.753	1.943	0.065	9.1	0.436	15.31 \pm 0.42	0.708	19.43 \pm 0.52
0.781	1.930	0.079	11.2	0.440	14.31 \pm 0.39	0.710	17.54 \pm 0.47
0.794	1.926	0.093	13.4	0.439	13.47 \pm 0.40	0.709	15.64 \pm 0.45
$Q^2=1.0$ (GeV/c) ²							
0.877	1.999	0.060	5.4	0.313	10.82 \pm 0.35	0.640	16.32 \pm 0.48
0.945	1.970	0.080	8.2	0.322	9.93 \pm 0.28	0.645	14.34 \pm 0.37
1.010	1.943	0.100	10.1	0.331	9.03 \pm 0.27	0.649	12.19 \pm 0.33
1.050	1.926	0.120	12.4	0.336	8.28 \pm 0.27	0.651	10.88 \pm 0.30
1.067	1.921	0.140	14.9	0.335	7.91 \pm 0.35	0.651	9.75 \pm 0.32
$Q^2=1.6$ (GeV/c) ²							
1.455	2.001	0.135	7.4	0.266	4.87 \pm 0.17	0.623	6.99 \pm 0.21
1.532	1.975	0.165	10.0	0.269	4.58 \pm 0.15	0.624	6.32 \pm 0.17
1.610	1.944	0.195	11.7	0.277	4.52 \pm 0.14	0.627	5.62 \pm 0.16
1.664	1.924	0.225	13.8	0.281	4.29 \pm 0.15	0.629	5.18 \pm 0.16
1.702	1.911	0.255	16.1	0.281	4.04 \pm 0.21	0.629	5.05 \pm 0.18

Table A.1: Unseparated cross sections $d\sigma/dt$ in $\mu\text{b}/\text{GeV}^2$

Q^2 (GeV/c) ²	W (GeV)	t (GeV ²)	θ_π^* (deg)	σ_L ($\mu\text{b}/\text{GeV}^2$)	σ_T ($\mu\text{b}/\text{GeV}^2$)
$Q^2=0.6$ (GeV/c) ²					
0.526	1.983	0.026	3.7	32.9 \pm 3.2	7.74 \pm 1.66
0.576	1.956	0.038	6.6	24.9 \pm 2.6	10.3 \pm 1.4
0.612	1.942	0.050	9.0	21.2 \pm 2.3	9.97 \pm 1.24
0.631	1.934	0.062	11.2	14.3 \pm 2.2	11.2 \pm 1.2
0.646	1.929	0.074	13.1	13.7 \pm 2.3	10.0 \pm 1.3
$Q^2=0.75$ (GeV/c) ²					
0.660	1.992	0.037	4.1	21.7 \pm 3.4	9.35 \pm 1.84
0.707	1.961	0.051	7.0	17.9 \pm 2.8	9.59 \pm 1.58
0.753	1.943	0.065	9.1	15.1 \pm 2.5	8.71 \pm 1.41
0.781	1.930	0.079	11.2	12.0 \pm 2.3	9.04 \pm 1.35
0.794	1.926	0.093	13.4	8.02 \pm 2.4	9.95 \pm 1.46
$Q^2=1.0$ (GeV/c) ²					
0.877	1.999	0.060	5.4	16.8 \pm 1.8	5.57 \pm 0.82
0.945	1.970	0.080	8.2	13.7 \pm 1.5	5.53 \pm 0.68
1.010	1.943	0.100	10.1	9.93 \pm 1.34	5.75 \pm 0.66
1.050	1.926	0.120	12.4	8.22 \pm 1.32	5.52 \pm 0.68
1.067	1.921	0.140	14.9	5.83 \pm 1.59	5.95 \pm 0.87
$Q^2=1.6$ (GeV/c) ²					
1.455	2.001	0.135	7.4	5.93 \pm 0.76	3.30 \pm 0.34
1.532	1.975	0.165	10.0	4.90 \pm 0.64	3.26 \pm 0.29
1.610	1.944	0.195	11.7	3.15 \pm 0.62	3.65 \pm 0.29
1.664	1.924	0.225	13.8	2.56 \pm 0.64	3.57 \pm 0.31
1.702	1.911	0.255	16.1	2.89 \pm 0.82	3.23 \pm 0.42

Table A.2: Separated cross sections $d\sigma/dt$ in $\mu\text{b}/\text{GeV}^2$

Appendix B

Tables for F_π data

In this appendix all values for F_π that were extracted in the analysis of the Jefferson Lab data and the re-analyses of the DESY and CEA/Cornell data are presented. Tables B.1 to B.4 contain the actual values of F_π that resulted from the analysis methods described in Subsections 6.2.1 to 6.2.4, including all fitting parameters. The uncertainties on these data are from the one- and two-dimensional least squares fits. Table B.5 contains all data relevant to the re-analysis of the CEA/Cornell, along with the old and new values for F_π from these data. The uncertainties reflect only the statistical uncertainties on the total measured cross sections.

Q^2 (GeV/c) ²	Λ_π^2 (GeV/c) ²	F_π	$Q^2 F_\pi$ (GeV/c) ²
0.60	0.483±0.055	0.446±0.029	0.267±0.017
0.75	0.406±0.065	0.351±0.037	0.263±0.028
1.00	0.484±0.048	0.326±0.022	0.326±0.022
1.60	0.505±0.052	0.240±0.019	0.384±0.031
0.70 ^a	0.552±0.072	0.441±0.032	0.308±0.023

^afrom the re-analysis of data from [Bra77].

Table B.1: The values of Λ_π^2 and F_π from analysis method 1 (Subsection 6.2.1).

Q^2 (GeV/c) ²	c ($\mu\text{b}/\text{GeV}^2$)	Λ_π^2 (GeV/c) ²	F_π	$Q^2 F_\pi$ (GeV/c) ²
0.60	16±10	0.7±0.2	0.538	+0.062
				−0.083
0.75	12±12	0.65±0.25	0.464	+0.081
				−0.116
1.0	5±5	0.6±0.1	0.375	+0.037
				−0.042
1.6	2±2	0.57±0.08	0.263	+0.026
				−0.029
0.7 ^a	3±2	0.7±0.1	0.500	+0.033
				−0.038

^afrom the re-analysis of data from [Bra77].

Table B.2: The values of the constant background term c , Λ_π^2 and F_π from analysis method 2 (Subsection 6.2.2)

Q^2 (GeV/c) ²	a	Λ_π^2 (GeV/c) ²	F_π	$Q^2 F_\pi$ (GeV/c) ²
0.60	30	1.7	0.738	0.443
0.75	17	1.05	0.584	0.438
1.0	15	1.2	0.545	0.545
1.6	10	1.2	0.429	0.686
0.7 ^a	4	0.8	0.500	0.373

^afrom the re-analysis of data from [Bra77].

Table B.3: The values of a , Λ_π^2 and F_π from analysis method 3 (Subsection 6.2.3).

Q^2 (GeV/c) ²	α (GeV ⁻²)	Λ_π^2 (GeV/c) ²	F_π	$Q^2 F_\pi$ (GeV/c) ²
0.60	5.1±2.7	0.65±0.15	0.520	0.312
0.75	7±7	0.6±0.2	0.444	0.333
1.0	2.5±2.0	0.6±0.1	0.412	0.412
1.6	1.5±1.5	0.75±0.25	0.319	0.511
0.7 ^a	1.8±1.2	0.7±0.1	0.500	0.350

^afrom the re-analysis of data from [Bra77].

Table B.4: The values of α , Λ_π^2 and F_π from analysis method 4 (Subsection 6.2.4).

Q^2 (GeV/c) ²	W (GeV)	ϵ	$d\sigma/d\Omega_\pi^*$ ($\mu b/sr$)	$d\sigma_T/d\Omega_\pi^*$ ($\mu b/sr$)		F_π	
				old	new	old	new
CEA							
0.40	2.15	0.87	8.90±0.34	2.921	3.116	0.570±0.016	0.556±0.016
0.79	2.15	0.83	6.99±0.37	2.080	1.503	0.384±0.014	0.410±0.013
1.19	2.15	0.79	3.54±0.28	1.570	1.005	0.238±0.017	0.283±0.015
Cornell I							
0.62	2.67	0.87	5.15±0.25	1.488	1.098	0.445±0.016	0.492±0.015
1.07	2.89	0.81	3.53±0.31	0.902	0.457	0.309±0.019	0.348±0.018
1.20	2.65	0.86	3.81±0.23	0.993	0.504	0.269±0.012	0.314±0.011
1.31	2.46	0.90	3.50±0.29	1.098	0.574	0.242±0.015	0.280±0.014
1.20	2.14	0.94	4.43±0.29	1.579	1.014	0.262±0.014	0.298±0.013
2.01	2.66	0.82	1.59±0.17	0.655	0.280	0.154±0.014	0.202±0.012
Cornell II							
1.22	2.14	0.95	5.08±0.74	1.558	0.999	0.290±0.030	0.330±0.028
1.20	3.08	0.82	3.09±0.31	0.732	0.335	0.294±0.019	0.333±0.018
1.71	3.09	0.79	2.52±0.32	0.551	0.210	0.238±0.020	0.272±0.018
1.99	2.14	0.94	2.28±0.29	1.071	0.673	0.179±0.021	0.240±0.018
Cornell III							
1.18	2.11	0.47	2.97±0.27	1.646	1.086	0.256±0.026	0.318±0.022
1.94	2.67	0.33	1.26±0.15	0.673	0.287	0.193±0.025	0.265±0.019

Table B.5: Re-analysis of the data from Ref. [Beb78] (old) with σ_T from the cross section model (Eq. 5.9). The new values for F_π are extracted using the VGL Regge model.

References

- [Abb95] D. J. Abbott *et al.*, *The CODA system and its performance in the First Online Experiments at CEBAF*, Proceedings of the 1995 IEEE Conference on Real-Time Computer Applications in Nuclear, Particle and Plasma Physics (May 1995), pp. 147-151
- [Ack78] H. Ackermann *et al.*, Nucl. Phys. **B137** (1978) 294
- [Ack98] K. Ackerstaff *et al.*, Nucl. Instr. Meth. **A417** (1998) 230
- [Ady77] G. T. Adylov *et al.*, Phys. Lett. **B51** (1974) 402 and G. T. Adylov *et al.*, Nucl. Phys. **B128** (1977) 461
- [Ame84] S. R. Amendolia *et al.*, Phys. Lett. **B138** (1984) 454
- [Ame86] S. R. Amendolia *et al.*, Nucl. Phys. **B277** (1986) 168
- [Arm98] C. S. Armstrong, *Electroproduction of the S_{11} Resonance at High Momentum Transfer*, Ph.D. thesis, The College of William & Mary (1998) unpublished
- [Arr98] J. R. Arrington, *Inclusive Electron Scattering From Nuclei at $x > 1$ and High Q^2* , Ph.D. thesis, California Institute of Technology (1998) unpublished
- [Ash99] D. Ashery, *Diffractional Dissociation of High Momentum Pions*, Invited talk, International Workshop on Electron Polarized Ion Collider, Bloomington, Indiana April 1999, and preprint hep-ex/9910024
- [Ass97] K. A. Assamagan, D. Dutta, P. Welch, *Hall C Matrix Element Optimization Package (CMOP)*, (1997) unpublished
- [Bak91] A. P. Bakulev and A. V. Radyushkin, Phys. Lett. **B271** (1991) 223
- [Bak95] O. K. Baker *et al.*, Nucl. Instr. Meth. **A367** (1995) 92
- [Bar85] L. M. Barkov *et al.*, Nucl. Phys. **B256** (1985) 365
- [Beb74] C. J. Bebek *et al.*, Phys. Rev. **D9** (1974) 1229
- [Beb76] C. J. Bebek *et al.*, Phys. Rev. **D13** (1976) 25
- [Beb78] C. J. Bebek *et al.*, Phys. Rev. **D17** (1978) 1693

- [Beh91] CELLO Collaboration, H.-J. Behrend *et al.*, Z. Phys. **C49** (1991) 401
- [Ber70] F. A. Berends, Phys. Rev. **D1** (1970) 2590
- [Ber95] M. Berz, Technical Report MSUCL-977, Michigan State University (1995) unpublished
- [Bis89] D. Bisello *et al.*, Phys. Lett. **B220** (1989) 321
- [Blo86] H. Blok, *Core polarisation and configuration mixing in ^{58}Ni studied by high resolution electron scattering*, Ph.D. thesis, Free University (1986) unpublished
- [Blo87] H. P. Blok *et al.*, Nucl. Instr. Meth. **A262** (1987) 291
- [Blo98] H. P. Blok, *Definition of kinematical Variables for Coincidence Studies*, Internal Report, F_π collaboration (1998) unpublished
- [Bos95] P. E. Bosted, Phys. Rev. **C51** (1995) 409
- [Bra76] P. Brauel *et al.*, Phys. Lett. **B65** (1976) 184
- [Bra77] P. Brauel *et al.*, Phys. Lett. **B69** (1977) 253; P. Brauel *et al.*, Z. Phys. **C3** (1979) 101
- [Bra00] V. M. Braun, A. Khodjamirian and M. Maul, Phys. Rev. **D61** (2000) 073004
- [Bro73] C. N. Brown *et al.*, Phys. Rev. **D8** (1973) 359
- [Bro80] K. L. Brown *et al.*, *TRANSPORT, a computer program for designing charged particle beam transport systems*, Technical Report CERN 80-04, CERN, 1980
- [Car94] F. Cardarelli *et al.*, Phys. Lett. **B332** (1994) 1; Phys. Lett. **B357** (1995) 267
- [Cas98] C. Caso *et al.*, *Review of Particle Physics*, Eur. Phys. J. **C3**, (1998) 1-794
- [CEB90] *CEBAF Conceptual Design report, Basic Experimental Equipment*, SURA, april 1990
- [CEB92] Technical report CEBAF-TN-92-054, *Hall C beam momentum measurement system*, (1992) unpublished

- [Che82] V. L. Chernyak and A. R. Zhitnitsky, Nucl. Phys. **B201** (1982) 492; Nucl. Phys. **B214** (1983) 547(E); Phys. Rep. **112** (1984) 173
- [Chu88] P. L. Chung, F. Coester and W. N. Polyzou, Phys. Lett. **B205** (1988) 545
- [Dal82] E. B. Dally *et al.*, Phys. Rev. Lett. **48** (1982) 375; Phys. Rev. Lett. **39** (1977) 1176; Phys. Rev. **D24** (1981) 1718
- [Dev72] R. C. E. Devenish and D. H. Lyth, Phys. Rev. **D5** (1972) 47
- [Dri71] C. Driver *et al.*, Phys. Lett. **B35** (1971) 77 and 81; Nucl. Phys. **B30** (1971) 245
7073
- [Dun98] J. Dunne, *Cryo and Dummy Target Information*, TJNAF Hall C document (1998) unpublished
- [Dut99] D. Dutta, *The $(e, e'p)$ Reaction Mechanism in the Quasi-Elastic Region*, Ph.D. thesis, Northwestern University, Evanston, Illinois (1999) unpublished
- [Ent99pc] R. Ent, private communication, 1999
- [Far79] G. R. Farrar and D. R. Jackson, Phys. Rev. Lett. **43** (1979) 246
- [Fra59] W. R. Frazer, Phys. Rev. **115** (1959) 1763
- [Gas99pc] D. J. Gaskell, private communication, 1999
- [Gro98] CLEO Collaboration, J. Gronberg *et al.*, Phys. Rev. **D57** (1998) 33
- [Gue98pc] P. Gueye and K. Gustafsson, private communication, 1998
- [Gut72] F. Gutbrod and G. Kramer, Nucl. Phys. **B49** (1972) 461
- [Hal84] F. Halzen and A. D. Martin, *Quarks and Leptons*, John Wiley & Sons, New York, 1984
- [Har89] L. H. Harwood *et al.*, Internal report CEBAF-PR-89-006, 1989
- [Isg84] N. Isgur and C. H. Llewellyn-Smith, Phys. Rev. Lett. **52** (1984) 1080; Nucl. Phys. **B317** (1989) 526
- [Ito92] H. Ito, W. W. Buck and F. Gross, Phys. Rev. **C45** (1992) 1918

- [Jac90] O. C. Jacob and L. S. Kisslinger, Phys. Lett. **B243** (1990) 323
- [Jac91] H. E. Jackson, *A Study of Longitudinal Charged Pion Electroproduction in ^2H , ^3He and ^4He* , CEBAF proposal E91-003, 1991
- [Jak93] R. Jakob and P. Kroll, Phys. Lett. **B315** (1993) 463
- [Jak96] R. Jakob *et al.*, J. Phys. **G22** (1996) 45
- [Jla99] Technical report Jlab-TN-99-006, *Orbit shift: Analysis and modeling of BSY-ARC transport line optics in absolute beam energy measurement at Hall C*, 1999
- [Kra93] G. Krafft and A. Hofler, Technical Report CEBAF-TN-93-004 *How the Linac Beam Position Monitors Work*, (1993)
- [Lep79] G. P. Lepage and S. J. Brodsky, Phys. Lett. **B87** (1979) 359
- [Leo87] W. R. Leo, *Techniques for Nuclear and Particle Physics Experiments*, second edition, Springer Verlag Berlin, Heidelberg 1987, 1994
- [Liu95] K. F. Liu *et al.*, Phys. Rev. Lett. **74** (1995) 2121
- [Mac87] R. Machleidt *et al.*, Phys. Rep. **149** (1987) 1
- [Mac96] D. J. Mack, H. P. Blok, G. M. Huber, E96-007, extension proposal to experiment E93-021
- [Mac99pc] D. J. Mack, private communication
- [Mak94] N. Makins, Ph.D. thesis, Massachusetts Institute of Technology (1994) unpublished
- [Mak98] N. Makins, R. Ent, *et al.* to be published
- [Man99] L. Mankiewicz, G. Piller and A. Radyushkin, Eur. Phys. J. **C10** (1999) 307
- [Mar98] P. Maris and C. D. Roberts, Phys. Rev. **C58** (1998) 3659
- [Mar00] P. Maris and P. C. Tandy, electronic preprint nucl-th/0005015
- [Mee98] D. G. Meekins, *Coherent π^0 Photoproduction on the Deuteron*, Ph.D. thesis, College of William & Mary (1998) unpublished
- [Mei95] T. Meissner, Phys. Rev. **C52** (1995) 3386

- [Mkr00pc] H. Mkrtchyan, V. Tadevosian, private communication, 2000
- [Moh99] R. M. Mohring, *A comparison of longitudinal and transverse cross sections in the $p(e, e' K^+) \Lambda$ and $p(e, e' K^+) \Sigma^0$ reactions*, Ph.D. thesis, University of Maryland (1999) unpublished
- [Mul90] P. J. Mulders, Phys. Rep. **185** (1990) 83
- [Nic98] G. Niculescu, *First Measurement of the Longitudinal and Transverse Cross Sections in $^1H(e, e' K^+) \Lambda$* , Ph.D. thesis, Hampton University (1998) unpublished
- [Pot99pc] D. H. Potterveld, private communication, 1999
- [Rad91] A. V. Radyushkin, Nucl. Phys. **A532** (1991) 532; Proceedings of the Second European Workshop “Hadronic Physics with Electrons beyond 10 GeV”, Dourdan, France, 1990
- [Sal51] E. E. Salpeter and H. A. Bethe, Phys. Rev. **84** (1951) 1232
- [Ste89] J. Botts and G. Sterman, Nucl. Phys. **B325** (1989) 62; H. N. Li and G. Sterman, Nucl. Phys. **B381** (1992) 129
- [Ste99pc] G. van der Steenhoven, private communication, 1999
- [Tan98] P. C. Tandy, electronic preprint nucl-th/9808029, proceedings to the Workshop on Future Directions in Quark Physics, 1998, Adelaide
- [Ter98] B. Terburg, Ph.D. thesis, University of Illinois (1998) unpublished
- [Van97] M. Vanderhaeghen, M. Guidal and J.-M. Laget, Phys. Rev. **C57** (1997) 1454; Nucl. Phys. **A627** (1997) 645
- [Vol96] J. Volmer, *Report on the acceptances, optical properties and resolution in the lean tune for HMS*, Report, Amsterdam (1996) unpublished
- [Vol98] J. Volmer, *Calculation of Energy Losses in Hall C’s Replay engine*, Internal Report, F_π collaboration (1998) unpublished
- [Vol99a] J. Volmer *et al.*, Proceedings of the 8th International Conference on the Structure of Baryons, Editors D. W. Menze and B. Ch. Metsch, World Scientific, Singapore, 1999, p. 605
- [Vol99b] J. Volmer and H.P. Blok, *Usage of Heepcheck*, TJNAF Internal Report (1999) unpublished

- [Wel94] P. Welsh, *CMOP, Hall C Matrix Element Optimization Package*, FORTRAN program, 1994
- [Wes99] D. van Westrum, *Quasielastic ($e, e'p$) Reactions and Proton Propagation through Nuclei*, Ph.D. thesis, University of Colorado, Boulder (1999) unpublished
- [Yan93] C. Yan *et al.*, CEBAF-PR-93-004, *Beam Energy Measurement Using the Arc Beam Line as a Spectrometer*, 1993

Samenvatting

De ladingsvormfactor van het pion via pi-onelectroproductie op het proton

De deeltjes die de atoomkern vormen, onder meer de nucleonen en π mesonen (ook wel hadronen genoemd), zijn volgens de Quantum Chromodynamica (QCD) opgebouwd uit fundamentele bouwstenen, de quarks en gluonen. Het bestaan van deze bouwstenen is experimenteel aangetoond. De structuur van hadronen kan echter nog niet *ab initio* met QCD berekend worden uit de interacties die tussen de quarks en gluonen plaatsvinden. In plaats daarvan zijn effectieve modellen ontwikkeld, die de laagenergetische interacties van quarks en gluonen beschrijven en voorspellingen doen voor de hadronische structuur.

Een manier om de structuur van hadronen experimenteel te bestuderen is door hun electromagnetische vormfactoren te meten. Deze grootheden bevatten informatie over de electromagnetische ladings- en stroomverdeling van de hadronen. De meetgegevens over vormfactoren kunnen gebruikt worden om de theoretische modellen te verbeteren. In deze dissertatie is de ladingsvormfactor van het pion, F_π , bestudeerd. Er zijn een aantal redenen om het pion te bestuderen. Ten eerste heeft het pion een interne structuur die eenvoudiger is dan die van een nucleon. Bovendien heeft het pion een zeer kleine massa, zodat het pion experimenteel gemakkelijker toegankelijk is dan andere mesonen. Tenslotte is het gedrag van de pionvormfactor bij zeer grote waarden van de impulsoverdracht (asymptotische limiet) bekend uit het verval van het pion. De relatie tussen deze twee kan worden berekend met behulp van storingstheoretische QCD. Daarentegen is de normering van de nucleonvormfactoren onbekend in deze limiet. Zeer nauwkeurige metingen van F_π zijn uitgevoerd voor waarden van de vierimpulsoverdracht in het kwadraat, Q^2 , die kleiner zijn dan 0.28 (GeV/c)^2 . De resultaten van deze metingen zijn gebruikt om

de RMS-straal van de ladingsverdeling van het pion te bepalen. Ofschoon verschillende theoretische modellen bij zeer kleine en zeer grote waarden van Q^2 hetzelfde gedrag van F_π geven, verschillen hun voorspellingen toch bij gemiddelde waarden van Q^2 . Daarom zullen metingen van F_π in dit gebied helpen om deze modellen te verbeteren.

Aangezien in het verleden slechts weinig betrouwbare meetgegevens voorhanden waren voor waarden van Q^2 boven de 0.7 (GeV/c)^2 , zijn er nieuwe nauwkeurige meetgegevens nodig. De metingen van de electroproductie van pionen in experiment E93-021, die besproken worden in deze dissertatie, leveren deze gegevens. Zij zijn eind 1997 uitgevoerd in Hall C van Jefferson Laboratory, Newport News in Virginia (VS) en omvatten waarden van Q^2 in het meetbereik van 0.6 tot 1.6 (GeV/c)^2 bij een waarde van de invariante energie W van het pion-nucleon systeem van 1.95 GeV. In een tweede fase van dit experiment zullen metingen plaatsvinden bij hogere waarden van Q^2 tot 3.2 (GeV/c)^2 . Bij de hier besproken metingen zijn pionen onderzocht door hoogenergetische electronen aan pionen te verstrooien, die in het proton gevormd worden. Voor ieder meetpunt zijn deze metingen uitgevoerd bij twee verschillende energieën van de verstrooiende electronen. Daardoor is het mogelijk de totale werkzame doorsnede in een Rosenbluth procedure te scheiden in bijdragen, waarbij het virtuele foton gepolariseerd is langs zijn voortplantingsrichting (σ_L) en loodrecht daarop (σ_T). Wanneer het gevormde pion zich voortplant in de richting van het virtuele foton, is σ_L gedomineerd door het proces, waarin het foton direct aan het pion koppelt. De sterkte van deze koppeling wordt bepaald door de vormfactor van het pion. Voor de correcte interpretatie van de bepaalde σ_L zijn ook de bijdragen van achtergrondprocessen onderzocht. Daarvoor zijn positief en negatief geladen pionen geproduceerd in een deuterium trefplaatje.

De optische eigenschappen van de twee magnetische spectrometers in Hall C vormen een belangrijk onderdeel van de in deze dissertatie beschreven analyse. Voor de “High Momentum Spectrometer” (HMS) is een andere opstelling van de quadrupool-magneten ingevoerd, waardoor het mogelijk is om de spectrometer op kleine strooihoeken (vanaf 10.5 graden) te plaatsen. Bij deze instelling zijn de optische eigenschappen opnieuw gecalibreerd. De nieuwe HMS instelling is zeer belangrijk geweest voor de metingen van data die gebruikt kunnen worden voor de Rosenbluth scheiding van de werkzame doorsnede. Ook zijn de optische eigenschappen, verzadigingseffecten en meetbereiken van de andere spectrometer, de “Short Orbit Spectrometer” (SOS), in detail onderzocht. De meetbereiken in hoeken en impuls van de spectrometers werden bepaald door electronen elastisch aan protonen te verstrooien. De gemeten opbrengst van dit proces komt binnen 2% overeen met een parametrisatie van gegevens uit eerdere metingen. De in deze dissertatie ont-

wikkelde calibratiemethoden voor de optische eigenschappen van de spectrometers en de bepaling van experimentele offsets zijn gebruikt in vervollexperimenten in Hall C.

De meetgegevens voor electroproductie van het pion bij dit experiment hebben veel kleinere statistische onzekerheden dan die van vorige experimenten. De werkzame doorsneden zijn bepaald met behulp van een Monte Carlo simulatie. Voor deze simulatie is een gedetailleerd model van de werkzame doorsnede aangepast aan de meetgegevens. In de simulatie is rekening gehouden met de meetbreiken van de spectrometers, resolutie effecten en andere fysische effecten. Het gebruik van een gedetailleerd model voor de werkzame doorsnede heeft tot doel om systematische fouten te minimaliseren. Deze fouten ontstaan bij het middelen van de opbrengst over grote gebieden van de faseruimte. Gebaseerd op de zo verkregen werkzame doorsneden is F_π bepaald. Hierbij is gebruik gemaakt van een recent Regge model van Vanderhaeghen, Guidal en Laget (VGL, Ref. [Van97]). Dit model beschrijft eerdere pion electro- en fotoproductie data. De voorspellingen van het VGL voor σ_L hebben een van de experimentele gegevens verschillend gedrag. Vanwege deze discrepantie was het niet mogelijk om direkt waarden voor F_π te verkrijgen. In plaats daarvan zijn realistische boven- en onderlimieten berekend, waaruit beste waarden voor F_π verkregen zijn. Deze methode is verder gebruikt om de modelonzekerheden op de verkregen waarden van F_π af te schatten.

Bovendien zijn eerdere meetgegevens uit experimenten bij DESY en CEA/Cornell (Ref. [Bra77, Beb78]) opnieuw geanalyseerd met dezelfde analysemethode die gebruikt is in dit experiment, dat wil zeggen de data voor σ_L uit deze experimenten zijn vergeleken met de voorspellingen van het VGL model. In het geval van de CEA/Cornell data was σ_L op een modelafhankelijke manier bepaald. Voor de bepaling van σ_L is in onze heranalyse gebruik gemaakt van de gemeten transversale werkzame doorsnede in plaats van het door de auteurs gebruikte fenomenologisch model voor σ_T . De nieuwe waarden van F_π komen voor waarden van Q^2 tussen 0.4 en 2.0 (GeV/c)² overeen met onze meetgegevens, hoewel zij grote systematische en statistische fouten hebben. Al deze data kunnen worden beschreven door een monopool parametrisatie van de pionformfactor die consistent is met de straal van het pion.

De bepaalde waarden van F_π laten zien dat $Q^2 F_\pi$ een maximum heeft ter grootte van meer dan 0.4 (GeV/c)² bij een Q^2 van boven de 2 (GeV/c)². Vrijwel alle theoretische berekeningen leveren maxima op, die te laag zijn, of bij $Q^2 < 2$ (GeV/c)² liggen. Slechts de meest recente berekeningen van Maris en Tandy (Ref. [Mar00]) beschrijven de data tot op $Q^2=2.0$ (GeV/c)². In de tweede fase van het F_π experiment op Jefferson Lab zullen metingen worden uitgevoerd bij waarden van Q^2 van

2.4 en $3.2 \text{ (GeV}/c)^2$. Dergelijke metingen kunnen vermoedelijk uitsluitsel bieden over de positie van het maximum voor de $Q^2 F_\pi$ verdeling.

Ten slotte is de precisie van de hier bepaalde werkzame doorsneden voldoende, modellen zoals het Born term en Regge modellen te verbeteren, zodat F_π met grotere nauwkeurigheid kan worden bepaald met die modellen. Toekomstige experimenten zouden profiteren van pionelectroproductie metingen bij hogere waarden van de invariante energie W . Regge modellen voorspellen namelijk dat σ_L en σ_T zich verschillend gedragen met W . Indien deze afhankelijkheden beide bekend zijn, dan is het mogelijk om de systematische fouten van σ_L en σ_T (en F_π) kleiner te maken.

Zusammenfassung

Der Ladungsformfaktor des Pions via Pionelektroproduktion am Proton

Die Erforschung der Struktur der Teilchen, aus denen der Atomkern aufgebaut ist, ist Gegenstand dieser Abhandlung. Diese Teilchen, u.a. die Nukleonen und Pionen (die sogenannten Hadronen), werden in der Quanten Chromodynamik (QCD) beschrieben als gebundene Systeme von noch elementarerer Teilchen, den Quarks und Gluonen. Die Existenz von Quarks als Bausteine der Nukleonen ist aus hochenergetischen Streuexperimenten bekannt. Aufgrund der Natur der starken Kernkraft ist es jedoch bislang nicht gelungen, innerhalb der QCD die Struktur der gebundenen hadronischen Zustände in einer konsistenten Art und Weise zu berechnen. Als Behelf wurden stattdessen Modelle entwickelt, die die niederenergetischen Wechselwirkungen zwischen Quarks und Gluonen näherungsweise, und daher einfacher berechenbar, beschreiben.

Elektromagnetische Formfaktoren geben Aufschluss über die Verteilung der elektrischen Ladung und Ströme in Hadronen. Deshalb ist es möglich, durch die Messung von Formfaktoren die Struktur von Hadronen zu studieren. Die Messdaten können dann benutzt werden, um die oben genannten theoretischen Modelle zu verbessern.

In der vorliegenden Arbeit wird die experimentelle Bestimmung des Ladungsformfaktors des Pions, F_π , behandelt. Die Untersuchung des Pion Formfaktors bietet mehrere Vorteile gegenüber nukleonischen und anderen mesonischen Formfaktoren. Zum einen hat das Pion als Meson (zwei Valenzquarks) eine einfachere Struktur als die Nukleonen und andere Baryonen (drei Valenzquarks). Wegen seiner geringen Masse ist es außerdem experimentell einfacher zugänglich als andere Mesonen. Zum anderen ist, im Unterschied zu den Nukleonformfaktoren, der Pionform-

faktor bekannt sowohl bei sehr kleinen als auch bei sehr großen Impulsüberträgen. Im asymptotischen Grenzbereich läßt F_π sich störungstheoretisch berechnen, wobei die Normierung aus dem schwachen Pionenzfall bekannt ist. Bei kleinen Viererimpulsüberträgen ($Q^2 < 0.28 \text{ (GeV/c)}^2$) liegen präzise Messungen vor, aus denen der mittlere Radius der Ladungsverteilung des Pions berechnet werden kann. Verschiedene Modellberechnungen beinhalten das Verhalten von F_π in beiden Extremen, unterscheiden sich aber im Bereich dazwischen. Die Messungen von F_π können also dazu genutzt werden, zwischen verschiedenen Modellen zu unterscheiden und diese gegebenenfalls zu verbessern.

Da in dem Übergangsbereich oberhalb von $Q^2=0.7 \text{ (GeV/c)}^2$ nur wenige fundierte experimentelle Daten für F_π vorhanden sind, sind neue Messungen notwendig. Die Messungen von Experiment E93-021, die Gegenstand dieser Arbeit sind, wurden Ende 1997 in der Experimentierhalle C am Jefferson Laboratory in Newport News, Virginia, durchgeführt. In diesem Experiment wurden Daten zwischen $Q^2=0.6$ und 1.6 (GeV/c)^2 genommen. In einer zweiten Phase werden voraussichtlich im Jahre 2001 oder 2002 weitere Messungen bei $Q^2=2.4$ und 3.2 (GeV/c)^2 vorgenommen. Um den Teil des Wirkungsquerschnittes, der den Austausch von longitudinal polarisierten Photonen beschreibt (σ_L), von dem transversalen Teil trennen zu können (L/T Separation), wurden die Messungen für jeden Datenpunkt bei zwei verschiedenen Elektron-Energien ausgeführt. Wenn das Photon direkt an das Pion koppelt, wird dieses in die Richtung des Photons ausgesendet. Bei diesem Prozess beschreibt der Formfaktor des Pions die Stärke der Kopplung des Photons an das Pion. Darum wird diese Reaktion zur Bestimmung von F_π benutzt.

Ein wichtiger Beitrag zu diesem Experiment war die Neueinstellung und Kalibration der magneto-optischen Eigenschaften der beiden Magnetspektrometer von Hall C. Da das "High Momentum Spectrometer" (HMS) zum ersten Mal bei einem Winkel von 10.5° benutzt wurde, mussten die Quadrupol-Magneten nach hinten verschoben werden. Das bedeutete, dass eine komplett neue Einstellung der Fokussiereigenschaften notwendig wurde. Die Entwicklung und Kalibration dieser Einstellung waren ebenso ein Teil der vorliegenden Arbeit wie die Kalibration des anderen Hall C Spektrometers, des "Short Orbit Spectrometer" (SOS). Die Kalibrationen und Normierungsfaktoren wurden anhand der Messung der elastischen Streuung von Elektronen an Protonen getestet. Die Übereinstimmung der daraus berechneten Wirkungsquerschnitte mit den sehr genau bekannten Wirkungsquerschnitten aus anderen Messungen war besser als 2%. Die in der vorliegenden Arbeit entwickelten Kalibrationsmethoden wurden in nachfolgenden Experimenten in Hall C erneut angewandt.

Für die Berechnung von unseparierten und separierten Wirkungsquerschnitten aus den experimentellen Daten wurde eine Monte Carlo Simulationssoftware benutzt, für die ein detailliertes Wirkungsquerschnittsmodell an die experimentellen Daten gefittet wurde. In der Simulationssoftware wurden Detektorakzeptanzen, Detektorauflösungen und physikalische Effekte wie Pionenzerfall und Strahlungskorrekturen simuliert. Mit dem Gebrauch des Wirkungsquerschnittsmodells wurden systematische Fehler aus der Mittelung über große Bereiche des Phasenraums minimiert. Zur Bestimmung von F_π aus den so gewonnenen Wirkungsquerschnittsdaten wurde ein Regge Model von Vanderhaeghen, Guidal und Laget (VGL, Ref. [Van97]) benutzt. Dieses ist an früheren experimentellen Daten für die Elektro- und Photoproduktion von Pionen getestet worden. Es enthält jedoch nicht einige Hintergrundprozesse, die die experimentellen Daten beeinflussen. Darum wurde in der Analyse eine Abschätzung für die Größe dieser Hintergrundprozesse gemacht und so neue beste Werte für F_π bestimmt.

Um zu einem konsistenten Bild aller vorhandenen experimentellen Daten zu gelangen, wurden die vorhandenen Wirkungsquerschnitte aus Experimenten am DESY und CEA/Cornell (Ref. [Bra77, Beb78]) mit Hilfe des VGL Modells re-analysiert. Im Falle der CEA/Cornell Daten wurde außerdem Gebrauch gemacht von den am Jefferson Lab gemessenen transversalen Wirkungsquerschnitten, um σ_L aus den vorhandenen unseparierten Wirkungsquerschnitten zu bestimmen. Der in dieser Weise konsistent analysierte Datensatz umfaßt Daten im Bereich von Q^2 zwischen 0.4 und 2.01 (GeV/c)². Trotz der großen systematischen Unsicherheiten in den CEA/Cornell Daten ergibt sich ein Bild, das von dem bisher angenommenen abweicht. Die neu berechneten F_π Werte liegen im Durchschnitt 10% oberhalb der alten Daten. Sie können mit einer Monopol-Funktion beschrieben werden, deren Parameter konsistent mit dem mittleren Radius der Ladungsverteilung des Pions ist.

Aus störungstheoretischen Berechnungen geht hervor, dass die Verteilung $Q^2 F_\pi$ bei kleinen Q^2 zunächst steigt, ein Maximum erreicht, und dann wieder abfällt, wobei sie sich der asymptotischen Berechnung annähert. Aus den vorliegenden Daten geht hervor, dass das Maximum wohl nicht bei einem Wert von Q^2 unterhalb von 2 (GeV/c)² erwartet werden kann. Es ist möglich, dass dieses in den zukünftigen Messungen erreicht wird. Die verschiedenen theoretischen Modelle unterscheiden sich unter anderem in dem Wert von Q^2 , wo das Maximum sich befindet. Die meisten hier besprochenen Modelle, von denen einige an die älteren Daten für F_π gefittet worden waren, liegen unterhalb der neuen Daten. Eine der neuesten Berechnungen (Maris and Tandy, Ref. [Mar00]) befindet sich jedoch in guter Übereinstimmung mit

den Daten, obwohl das Modell nicht an die experimentellen Daten für F_π optimiert ist.

Auch die Wirkungsquerschnittsdaten vom Jefferson Lab Experiment lassen sich weiter gebrauchen. Sie sind präzise genug, um dafür benutzt zu werden, Born Term oder Regge Modelle zu verbessern. Solche verbesserten Modelle könnten in der Zukunft dazu dienen, F_π mit größerer Genauigkeit und geringerer Modellabhängigkeit zu bestimmen. Zukünftige Messungen würden davon profitieren, Daten zu sammeln bei höheren Werten der invarianten Masse W . Dies wäre von Nutzen, da Regge Modelle vorhersagen, dass die Wirkungsquerschnitte σ_L und σ_T verschiedene W -Abhängigkeiten besitzen. Mit einem genaueren Verständnis dieser Abhängigkeiten ließe sich die Bestimmung von F_π weiter verbessern.

Nawoord

Mijn werk en leven in Amsterdam en Newport News heeft mij een schat aan dierbare en waardevolle ervaringen gebracht. Vele mensen hebben deze tijd voor mij verrijkt en het tot stand komen van dit proefschrift pas mede mogelijk gemaakt. Ik heb me altijd bij jullie thuis gevoelt. Daarvoor mijn dank aan iedereen. Ik zou de afgelopen vierenhalf jaren en de mensen daarin om geen prijs willen missen.

My working and living in Amsterdam and Newport News have given me a treasure of wonderful experiences. Many people have enriched this period of time for me and made this work possible. I always felt at home with y'all. I wish to thank you all for this. I would not wish to have missed a minute of the time and the people of the last four and a half years.

Uiteraard is het een onmogelijke opgave een ieder aan deze plaats op te noemen, laat staan in voldoende mate te danken. Desalniettemin wil ik graag de mensen noemen aan die ik me in bijzondere mate verbonden voel.

Beste Henk, ik heb helaas maar een alinea voor jou. Zal ik jouw altijd inspirerende begeleiding noemen, onze talloze gesprekken binnen en buiten de kernfysica, je rijke schat aan kennis en ervaring die je altijd bereid was met je promovendi te delen? Het is vanzelfsprekend dat jouw invloed op mijn werk en mijn schrijven vooruitzetting waren voor het slagen van deze onderneming. Maar mijn dank zou incompleet zijn zonder onze musikale avonturen te noemen, met z'n tweeën, drieën of vijven*. En, last but not least, mijn dank aan Marian en jou voor de gastvrijheid die ik in Ouderkerk a/d Amstel vele malen mocht genieten!

Dear Dave, my almost two years at Jefferson Lab would not have been so productive and enriching had it not been for your infatigable willingness to discuss matters big and small of work and life at any given moment. Your highly practical way of working as well as organizing will always be a shining example for me. My gratitude also extends to your family for having me over numerous times.

*Deze dank gaat ook uit naar de heren Schubert, Brahms en Dvořák

Beste Ger, je drukke agenda en verantwoordelijkheid voor het welvaren van het NIKHEF hebben je gelukkig niet gehinderd om met je levendig en persoonlijk interesse het ontstaan van deze proefschrift altijd kritisch te begeleiden. Je inzichten en commentaren waren altijd helder en hulprijk en hebben geholpen dit boekje op een goede pad te brengen.

Beste Rolf, ik heb de samenwerking met jouw altijd als gezellig en productief ervaren. Jouw bijdragen tot de HMS-100 tune en het ontravelen van de geheimen van de SOS zijn essentieel voor het slagen van dit werk geweest! Van harte bedankt voor alles!

Dear Kelley, I have enjoyed very much working with you on the experiment. Without your numerous contributions to the pre-experiment turnaround of Hall C, the conduct of the experiment and the data analysis this work would not have been possible. All the best to you and your family!

Dear Dave, you are a pal. Your NucPi analysis single-handedly added a sizeable contribution to our own. I have always known you as a kindred spirit and enjoyed your company. I wish you the best of luck for your future!

Dear Garth, I would like to thank you for all of our (mostly) late night discussions. Your scientific and moral support was very helpful!

I would like to thank Hamlet Mkrtchyan and Vardan Tadevosyan, Bryon Mueller, Rob van der Meer and Ilkyoung Shin, Chris Armstrong and Ketevi Assamagan for their valuable contributions to the data analysis. Of the Hall C staff I would most like to thank Paul Brindza, Roger Carlini, Allison Lung, Joe Mitchell, Bill Vulcan, Steve Wood and Chen Yan for their contributions to the successful completion of the experiment.

Dear Marc Vanderhaeghen and Michel Guidal, thank you for your always swift help in implementing your model in the analysis. I also extend my gratitude to Justus Koch for evaluating the theory chapter of this thesis.

My very special thanks go out to Kathy, Allie and Shadow and of course Sasha, who suffered me as a house-mate for two great years. Did we host Party-Central on the beach or what?

Party-central and the rest of the two years at JLab would of course not have been what they were without the presence of my dear colleagues and friends (beg your pardon if I forgot anyone): John Arrington, Steve Avery, Tony Day, Dipangkar Dutta, Furbee, Joe Grames, Paul Gueye, Kenneth Gustafsson, Marie Gustafsson, Doug Koltenuk, Laura Marcucci, Dave Meekins, Rick Mohring, Ioana and Gabriel Niculescu, Erika Reif, Derek van Westrum and the whole gang of frenchies.

Ondanks mijn lange amerikaanse danklijst heb ik het grotere deel van mijn tijd in Amsterdam toegebracht. Hier ben ik mijn collegas van de EMIN groep tot dank

verplicht. Aan de eerste plek komt daar Martijn Steenbakkers, mijn vriend en kamergenoot. Geschiedenis, voetbal, PAW, L^AT_EX, he is your man. Martijn, van harte bedankt voor drie uitermate gezellige jaren!

Voor mij is David Groep altijd de IT brain van de ploeg geweest. Hij is altijd bereid zijn kennis van alles (programmeren, fysica of autos (nog eens drievoudig bedankt!)) te delen. Wat ik maar over XBlast weet, heb ik van jou geleerd!

Marcel van Batenburg, je bent een prima huisgenoot. Ik snap niet al jouw verhalen, maar ik kom dichterbij. Dank je van harte voor je hulp bij de nederlandstalige samenvatting!

De groep van de N2.xx gang uit mijn tijdperk zou niet compleet zijn zonder David Boersma, Ronald Starink, Niels van Bakel, Igor Passchier, Laurens van Buren, Louk Lapikás, Willem Hesselink en Jos Steijger. Bedankt voor de vele uren gezellige babbel met en zonder koffie!

Met het grootste plezier heb ik deel uitgemaakt van het VU orkest en kamerorkest. En wie is de ziel van elk orkest? De altviolen uiteraard! Mijn dank dus aan onder meer Barbara, Christian, Mia-Petra, Roemer, Martine en Janneke, maar ook aan Daan Admiraal. Speciale dank aan Marjolein Vinkenoog voor de contributie tot de samenvatting!

An der WWU Münster habe ich einen Freund gewonnen, der mir bis auf den heutigen Tag gewogen ist. Ich möchte Dir, Ulf, danken für Deine langanhaltende moralische Stütze. Und mit niemandem würde ich ruhiger (und besser ausgerüstet!) in die Wildnis ziehen!

Schlußendlich gebührt mein tiefster Dank meinen Eltern, Felix und Renate, die mich immer ohne Vorbehalt in meinem Tun unterstützt haben, tatkräftig und moralisch. Durch sie habe ich die Freude an der Wissenschaft gefunden.